Transforming Ultra-High Molecular Weight Polyethylene Fibers: Sustainable Production Methods, Nanocomposites, and Carbon Fibers

---

A Dissertation

presented to

the faculty of the School of Engineering and Applied Science

University of Virginia

---

in partial fulfillment of the requirements for the degree

Doctor of Philosophy

by

Kenneth R. Brown

August 2024

APPROVAL SHEET

This

Dissertation

is submitted in partial fulfillment of the requirements for the degree of

Doctor of Philosophy

Author: Kenneth R. Brown

Advisor:	Xiaodong Li
Committee Chair:	Baoxing Xu
Committee Member:	Liheng Cai
Committee Member:	David L. Green
Committee Member:	Tao Sun

Accepted for the School of Engineering and Applied Science:

Jennifer L. West, School of Engineering and Applied Science

August 2024

Abstract

Reducing greenhouse gas emissions in the transportation sector is crucial to slowing the progress of global climate change. This may be accomplished in part by improving the energy efficiency of the vehicle through weight reduction. Polymer-matrix composite materials reinforced with high-performance fibers, such as carbon fibers and ultra-high molecular weight polyethylene (UHMWPE) fibers, or nanoparticles, such as graphene, can be used to replace dense metals thereby reducing mass. However, producing them is costly and environmentally damaging due to extensive use of non-renewable petrochemical solvents, and much remains to be learned about the effects of using more sustainable materials and methods to make these fibers and composites.

The aim of this dissertation is to advance our understanding of the relationship between the processing and resultant microstructure and properties of these materials. UHMWPE fibers were selected as the material of interest because its extremely long molecular chains present significant opportunities and challenges. It has been shown that these fibers can be converted into carbon fibers, and it is hypothesized that the long-range order in these fibers may make an ideal framework for highly graphitic carbon fiber production. However, the effect of tension applied during the stabilization of these fibers in preparation for carbonization is heretofore unexplored. Probing this processing parameter revealed the microstructural evolution of UHMWPE during conversion to carbon fibers and offered key insights for optimizing the conversion of all PE-grades.

UHMWPE fibers possess remarkable properties thanks to their long molecular chains, but the deep entanglement of these chains inhibits the use of low-cost melt processing methods. Instead, non-renewable petrochemical solvents are used at high concentration (as much as 98% by weight) to disentangle these chains through dissolution thereby enabling extrusion into fibers. A bio-derived solvent called orange terpenes has been previously demonstrated as a renewable

replacement for solution spinning of UHMWPE fibers, but scant information on the microstructure and properties of these fibers makes it difficult to assess its potential. Single-filament tensile testing coupled with thermal and X-ray microstructural characterizations revealed that these fibers develop the fundamental crystalline structures and mechanical properties indicative of high-performance potential given parametric optimization of processing conditions. This result inspired the search for a solvent suitable for dissolving UHMWPE and stably dispersing graphene nanoparticles simultaneously to form high-performance polymer nanocomposite fibers. Another terpene, 1,4-cineole, was selected and shown to be capable of highly stable graphene suspensions. UHMWPE-graphene fibers were produced and characterized to understand the effect of the nanoparticles on the microstructure and properties of the fibers. It was revealed that the nanoparticles were well-dispersed but suffer poor interfacial adhesion in the polymer matrix. At high concentration, they impede the formation and orientation of the load-bearing crystalline microstructure of the fibers, but a percolation threshold was found whereby the particles reinforce the matrix.

The findings presented in this dissertation expand the current understanding of the process-structure-property relationships underlying the production of UHMWPE fibers, polymer nanocomposites, and polyethylene-derived carbon fibers. These represent new steppingstones towards more environmentally friendly production of materials that are needed to improve the sustainability of human mobility. Recommendations for future work are included in the final chapter of this dissertation.

Acknowledgements

This work would not have been possible without the tireless love and devotion of my wife, the mother of our children, Laura Falconi. I would have never pursued this degree without her inspiration, and I could never have achieved it without her support. Laura, this dissertation is dedicated to you for all that you have given me in life. I am forever grateful to be at your side. Thank you for being there for me through the rollercoaster of emotion that this journey has been, for always listening to my ideas and presentations as well as my anxieties and fears, and for always being my steady foundation.

My extended family, on both sides, also supported me through their love and listening ears. Thank you to my parents, brother, grandmother, and all my in-laws for always being there for me. I want to specially acknowledge my late grandmother-in-law, Dottie, who was unquestionably the best person I have ever met and always cheering for me. I miss her very much.

Thank you to my advisor, Professor Xiaodong "Chris" Li, for encouraging me to pursue a PhD over a master's degree, then mentoring me through this process for the past five and a half years. He recognized the potential in me before I ever could and has been deeply dedicated to my mission to become a professor myself. I have grown so much through this process thanks to him carefully pushing me out of my comfort zone and encouraging me to aim higher than I thought possible. I would also like to thank my committee members, Prof. Baoxing Xu, Prof. David Green, Prof. Tao Sun, and Prof. Liheng Cai for supporting my journey with their time and expertise.

As singular as this academic pursuit can feel at times, it is truly a team effort to conduct good research and I was never alone in that regard. I am grateful to all my peers, past and present, for their willingness to assist me with their skills and knowledge. I would like to personally acknowledge Dr. Clifton Bumgardner, Cole Love-Baker, Prof. Timothy Harrell, Andriy

Sushchenko, ZhiJing Xue, Ryan Cordier, Alexander Scherschel, Dr. Zan Gao, and Luke Skrzypczak. Each of them offered their support unconditionally and have made an immeasurable impact on my graduate education and experience.

Finally, this work was funded by the U.S. Department of Energy Vehicle Technologies Office (DE-EE0008195) and Hydrogen and Fuel Cell Technologies Office (DE-EE0009239) and supported by various collaborators and research staff at the University of Virginia and beyond. The University of Virginia Nanoscale Materials Characterization Facility was instrumental to completing this research, and I greatly appreciate the help of staff members Richard White, Dr. Joseph Thompson, and Dr. Cathy Dukes for their patient training sessions and careful equipment maintenance. Dr. Diane Dickie assisted with wide-angle X-ray characterizations at UVA, which was conducted using single-crystal WAXS machines funded by the NSF-MRI program, grant award CHE-2018870. Erin Crater conducted small-angle X-ray scattering supervised by Prof. Robert Moore and furnished by Virginia Tech's Materials Technology Characterization Facility, which is supported by the Institute for Critical Technology and Applied Science, the Macromolecules Innovation Institute, and the Office of the Vice President for Research and Innovation at Virginia Tech. Prof. Elizabeth J. Opila graciously allowed me to extensively use her lab's simultaneous thermal analyzer and analytical balances, and her graduate students, Dr. Coleman Tolliver and Clark Luckhardt, offered their help whenever I asked. Last, but not least, thank you to Prof. Donald Griffin for access to his lab's viscometer and Jules Bates for her assistance using it.

Table of Contents

List of Figures

List of Tables

Common Abbreviations and Acronyms

AFM	atomic force microscopy
CAD	computer aided design
COV	coefficient of variance
DI	deionized
DSC	differential scanning calorimetry
FWHM	full width at half maximum
GnP	graphene nanoplatelet
HDPE	high density polyethylene
HOF	Herman's orientation factor
HRTEM	high resolution transmission electron microscopy
HSP	Hansen solubility parameters
HWHM	half width at half maximum
LDPE	low density polyethylene
LLDPE	linear low-density polyethylene
NMR	nuclear magnetic resonance spectroscopy
PAN	polyacrylonitrile
PE	polyethylene
RED	relative energy difference
SAXS	small-angle X-ray scattering
SEM	scanning electron microcopy
TEM	transmission electron microscopy
TGA	thermogravimetric analysis
UHMWPE	ultra-high molecular weight polyethylene
UTM	universal testing machine
WAXS	wide-angle X-ray scattering
XRD	X-ray diffraction

Chapter 1: Introduction

1. Lightweight, High-Performance Materials Crucial for Sustainability

The rising effects of global climate change are increasing the urgency of finding and applying measures to reduce greenhouse gas emissions. The transportation sector is a prime candidate for decarbonization. It accounts for 25% of global greenhouse gas emissions [1] and is the biggest contributor to U.S. greenhouse gas emissions by sector as of 2022 [2]. Greenhouse gas emissions can be reduced by improving the energy efficiency of all modes of transportation through vehicle weight reduction, which can be accomplished in large part by replacing high density metals conventionally used in their construction, such as steel, with low-density materials of commensurate properties. This has driven great interest in composite materials that possess low density and high mechanical performance. A composite is composed of a matrix material, oftentimes a thermoset or thermoplastic polymer, that is reinforced by another material that offers desirable properties such as high strength and stiffness or high thermal or electrical conductivity. This combination is oftentimes synergistic: the low-density matrix material may be highly formable but possesses insufficient strength and stiffness for the desired application whereas the reinforcement material may have high mechanical properties but lacks formability to create a net shape. Reinforcement materials are employed in many shapes and sizes, such as woven textiles, unidirectional fibers, chopped fibers, and particles of various sizes, which gives engineers a broad set of tools for meeting both performance and weight reduction criteria in their designs. Fibers are one of the most common reinforcements for composites throughout history, and recently nano-scale particles, referred to as nanofillers, have received intense attention due to their exceptional properties.

High-performance fibers, such as fiberglass, basalt fibers, carbon fibers, and highly oriented polymer fibers like Kevlar or ultra-high molecular weight polyethylene (UHMWPE), are desirable reinforcement materials because they have exceptional specific strength and stiffness, and their transversely isotropic properties enable composites designers to tune a final component's properties by orienting the fibers to achieve their design criteria while minimizing weight [3]. Such composites have become staples of high-performance industries, such as aerospace and motorsports, due to the exceptional strength-to-weight ratios that can be achieved.

While fiber-reinforced composites have been used and studied for hundreds of years, nanoparticle-reinforced composites have recently come to the fore as the exceptional properties of nanoparticles, particles with at least one dimension on the order of nanometers such as graphene and carbon nanotubes, were discovered in the past three decades. For example, single-layer graphene sheets possess a tensile modulus of up to 1 TPa and tensile strength of 130 GPa [4] in addition to superior electrical [5] and thermal conductivity [6]. Accordingly, great attention has been paid to incorporating these nanoparticles into polymers, including thermoplastics, thermosets, and elastomers, to enhance mechanical performance and imbue thermal and electrical conductivity for applications in wearable electronics, electromagnetic shielding, and structural health monitoring [7,8].

Both fiber-reinforced and nanoparticle-reinforced composites stand to greatly improve the energy efficiency of vehicles by supplanting denser materials, but the environmental cost of producing these materials must also be considered. In this dissertation, the current state of high-performance fibers, specifically carbon fibers and UHMWPE fibers, and nanoparticle composites is reviewed and pathways to more sustainable production of these materials are demonstrated. Through this work, new understandings of the relationships between the production of these

materials, their microstructure, and resultant properties are unveiled, which advances the state of lightweight, high-performance materials development.

2. High-Performance Fibers for Fiber-Reinforced Composites

Many fibers have been employed in fiber-reinforced composites throughout history with modern examples including glass, basalt, carbon, silicon carbide, aramids (Kevlar), UHMWPE, and many more. The present work will focus on UHMWPE fibers and carbon fibers derived from UHMWPE fibers, and the remainder of this section of Chapter 1 introduces the fundamentals of UHMWPE and carbon fibers.

2.1. About Ultra-High Molecular Weight Polyethylene Fibers

Polyethylene describes a class of polymers that are composed of ethylene monomers that are classified by their density and degree of branching into the several categories including the four most common types: linear low-density polyethylene (LLDPE), low-density polyethylene (LDPE), high-density polyethylene (HDPE), and UHMWPE [9]. The differences in molecular structure of these PEs is shown schematically in Figure 1 [10].

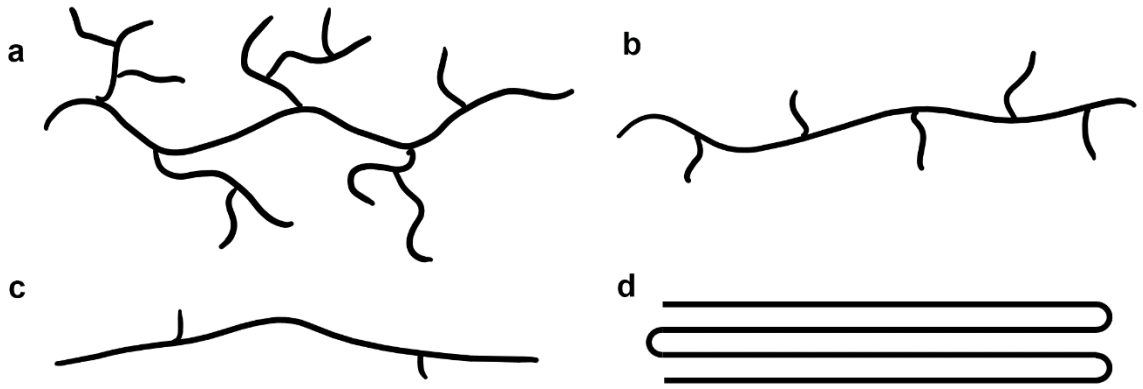

Figure 1. *Schematic representation of polymer chain crosslinking in a) LDPE, b) LLDPE, c) HDPE, and d) UHMWPE* [10]. *Each is a simplistic representation highlighting key features, such as the long branching of LDPE and short branching of LLDPE, the relatively linear structure of HDPE, and long folded chains characteristic of UHMWPE. In all cases, these structures vary throughout the polymer*

LDPE exhibits extensive long-chain branching and is consequently the lowest density of all PEs. The highly branched structure also yields the lowest melting temperature of all PEs of 80-110°C [10]. LLDPE, is a copolymer of ethylene with a few percent of an α-olefin comonomer that exhibits short-chain branching, which results in slightly higher tensile strength, impact resistance, melting temperature (115-125°C) and density compared to LDPE [10]. HDPE has a melting temperature of approximately 120-140°C and exhibits limited short-chain branching [9]. UHMWPE chains are linear much like HDPE but are significantly longer; UHMWPE has a molecular weight of at least 3M g/mol. These ultra long molecular chains oftentimes form into crystalline structures, which is represented as a folded chain crystal in Figure 1d.

UHMWPE ranks amongst the highest performance technical-grade polymers boasting high mechanical properties, low density, low coefficient of friction, and exceptional chemical resistance, moisture resistance, and biocompatibility [11]. Accordingly, UHMWPE has found myriad applications in film, fiber, and bulk form including battery separators [12,13], lightweight ballistics protection [14], and biomedical implants [15]. UHMWPE fibers have 10x greater tenacity by weight than steel fibers [16], which has engendered its use in fiber-reinforced polymer composites [11,17], woven textiles for wearable devices [18], and lightweight anchor ropes for the largest ships and offshore installations in the world [19]. These exceptional properties are achieved through the fiber spinning and drawing processes, which extends and preferentially aligns the extremely long UHMWPE molecules along the fiber axis. However, conventional fiber melt spinning processes cannot be applied due to the extensive molecular entanglement of these long molecules without modifications. This is overcome by dissolving UHMWPE into a semi-dilute solution that can be extruded through small orifices wherein the polymer solution gels upon

cooling. This process, referred to as gel spinning, was invented in the late 1970's and has come to dominate commercial production of UHMWPE fibers [20].

Gel spinning can be further divided into two subsets based on the way the solvent is removed. In one, referred to as wet extraction, a non-volatile solvent dissolves the UHMWPE and a volatile extraction solvent is required to remove the non-volatile solvent from the gel fiber after spinning. Paraffin oil is most commonly used for industrial-scale wet extraction gel spinning of UHMWPE [21]. The extraction solvents are typically harmful petrochemical liquids such as hexane, toluene, dioxane, methylene chloride, and trichlorotrifluoroethane [22]. In the other subset, referred to as dry extraction, a volatile solvent is used to dissolve UHMWPE, and the solvent evaporates out of the gel fiber without any additional extraction solvent. Decalin is most commonly used for industrial-scale dry extraction gel spinning of UHMWPE, and some studies have used other petrochemical solvents such as naphthalene, 1,2,4-trichlorobenzene, dodecane, camphene, and p-xylene [22–24]. In both cases, the use and recovery of these solvents is costly due to the solvent volume and environmental controls required at industrial scale, they present a host of health risks to those exposed to them [25], and their production is energy intensive and detrimental to the environment [26–28].

2.2. About Carbon Fibers

Carbon fibers are thin filaments containing at least 92 wt% carbon atoms arranged in planar hexagonal networks [29]. Consequently, they possess high elastic modulus (up to 940 GPa for pitch-derived carbon fibers) and strength (up to 7 GPa for polyacrylonitrile (PAN)-derived carbon fibers) as well as low density due to their atomic composition [30]. The vast majority of carbon fibers are derived from PAN, which requires solution spinning PAN into fibers, thermo-oxidatively stabilizing the fibers in air in the temperature range of 200-400°C, then carbonizing

the fibers at high temperature in the range of 1000°C to 1700°C [30–33]. Ultra-high performance carbon fibers can be created by graphitizing the fibers at temperatures ranging from 2500°C to 3000°C after carbonization [34,35], but this is an expensive procedure often reserved for special applications. PAN achieved dominance as a precursor due to its relatively high carbon yield, highly tunable processing parameters, and the superior properties of the carbon fibers it yields [36,37]. Although this precursor is referred to simply as PAN, it is most commonly a copolymer of PAN and another acrylic comonomer, such as acrylic acid, methacrylic acid, or methacrylate, amongst others, to improve drawability [38]. The critical advantage of PAN is that the material can be stabilized at temperatures below its melting point, thereby retaining the fibers' morphology during subsequent thermo-oxidative stabilization. Strong interactions of highly polar nitrile groups allow for the cyclization of PAN molecules in the temperature range of 180-250°C whereas it melts at 317°C [39–41]. However, producing PAN fibers is expensive; the precursor fibers account for 53% of the total cost of a carbon fiber [42]. Because PAN cyclizes and degrades before it melts, it must be dissolved in a highly polar solvent, such as dimethylformamide or dimethyl sulfoxide, to be spun into fibers [43]. This process is called solution spinning, which is subdivided into three types: wet spinning, dry-jet wet spinning, and dry spinning. Wet spinning is the most common method of solution spinning employed to form PAN fibers and involves the injection of a PAN/solvent solution from small orifices into a solvent/non-solvent coagulation bath to induce the precipitation of fibers, Figure 2 [44]. Dry-jet wet spinning is a modification of wet spinning wherein an air gap of 10-200mm is established between the point of extrusion and the coagulation bath [41]. It can enable non-circular fiber cross sections and results in greater mechanical properties, faster spinning, and higher solid content [38]. However, it is limited to filament counts less than 12,000 whereas wet spinning can achieve filament counts greater than 50,000 [41]. Both

wet spinning processes involve a series of coagulation baths of different compositions and temperatures to achieve the desired fiber shape, dimensions, and properties by controlling the flux of solvent out of and water into the fiber [45,46]. The fibers are typically stretched after they are formed to improve molecular alignment, dried to remove water content, and relaxed to reduce internal stresses induced by the stretching process following their formation [41,47]. The wet spinning process is relatively slow because it is limited by the rate at which the fibers can form while achieving desired properties, and it is expensive because it requires constant maintenance, turnover, and disposal of the hazardous coagulation bath solution [42].

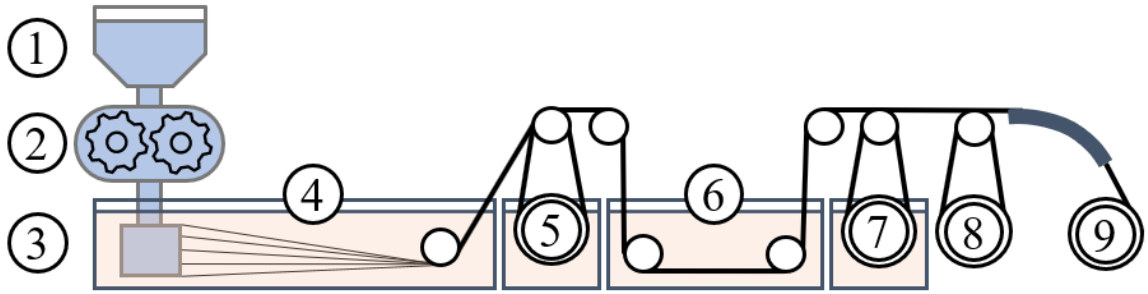

***Figure 2**. Abbreviated schematic of a wet spinning line composed of 1) polymer solution reservoir, 2) metering pump, 3) spinneret, 4) coagulation bath, 5) washing bath, 6) drawing bath, 7) secondary washing bath, 8) drying godet, and 9) dry-heated stretching and takeup* [44]. *Wet spinning lines can feature several washing baths in series to achieve proper solvent exchange* [46]

Dry spun fibers are formed by extruding a polymer solution into a heated gas atmosphere where the solvent evaporates leaving a solidified fiber. A suitable solvent for this process must not only readily solvate PAN but must also have a low vapor pressure and high stability with PAN at its boiling point. Accordingly, dimethylformamide or dimethylacetamide are commonly used [48]. The dry spinning process enables the production of fibers with non-circular cross sections but requires careful control of the drying process so that enough solvent is retained as a plasticizer whilst capturing as much solvent as possible to be reused and prevent pollution. The complicated equipment required to achieve the desired fiber morphology and safely contain the vaporized

volatile organic solvents makes this a costly process. The dry spinning of acrylic fibers was well-reviewed by Imura et al. in 2014 including a schematic of a typical acrylic fiber dry spinning system, shown in Figure 3 [49].

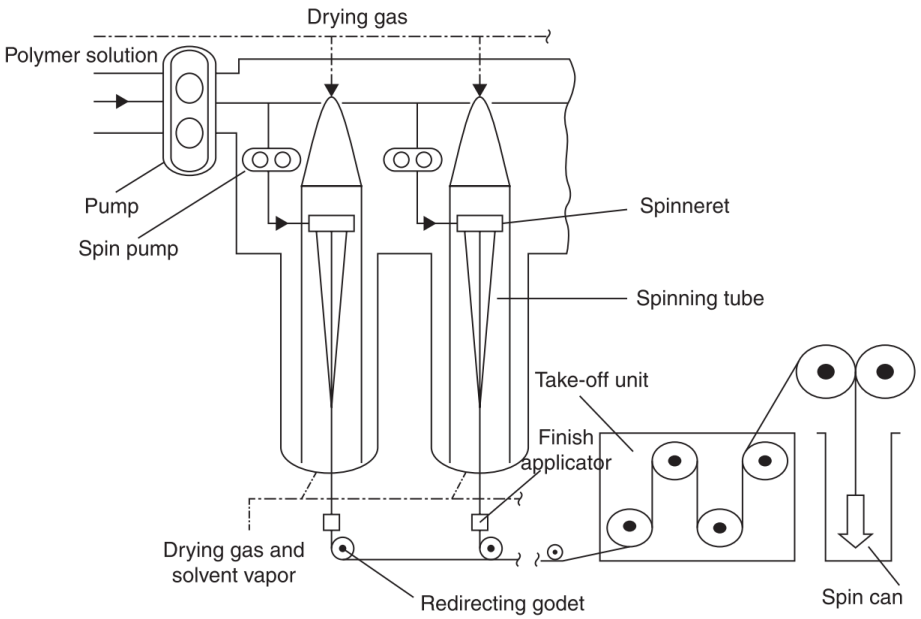

Figure 3*. Schematic of a typical dry-spinning system for acrylic fibers* [49]

Replacing the solution spinning process with a more economical fiber spinning method may greatly reduce the cost of producing precursor fibers and thus carbon fibers. An attractive alternative to wet spinning is melt spinning, which is one of the most popular fiber spinning methods due to its simplicity, high throughput, and low cost. This has inspired significant research effort towards the conversion of melt-spinnable polymers into carbon fibers in recent decades [50].

3. Nanoparticle-Reinforced Composites

The term nanoparticle is used to describe any particle with at least one nanoscale dimension. Some nanoparticles, such as carbon black, have been in use for millennia, well before the term nanoparticle was even coined [51]. In the past thirty years, carbon-based nanoparticles, such as graphene and carbon nanotubes, have attracted immense attention due to their exceptional

mechanical [4,52,53], electrical [5,54], thermal [6,54], and gas barrier properties [55]. Accordingly, great attention has been paid to incorporating these nanoparticles into myriad materials including polymers, such as thermoplastics, thermosets, and elastomers, to enhance mechanical performance and imbue thermal and electrical conductivity for applications in wearable electronics, electromagnetic shielding, and structural health monitoring [7,8]. High-performance polymers, such as UHMWPE, are particularly interesting for the deployment of any nanofiller because their performance envelope could be extended towards applications typically reserved for higher density materials such as carbon fibers or metals [56]. Graphene is especially well-suited for polymer nanocomposites due to its high surface area and 2D morphology, and it will be the focus of the nanocomposites formed and analyzed in this dissertation.

3.1. About Graphene

Graphene is characterized as a two-dimensional hexagonal lattice of carbon atoms that was first discovered in 2004 through the micromechanical exfoliation of graphite [57,58]. As a stable two-dimensional crystal, which had previously been theorized to be impossible, it immediately drew attention as a well of opportunity. Indeed, in the succeeding decade it was shown that single-layer graphene possesses remarkable mechanical [4], electrical [5], thermal [6], optical [59], and barrier [55] properties. Brimming with visions for wide-ranging applications, research and development efforts focused on methods of producing graphene at greater scale. This gave rise to new subclasses of graphene such as graphene oxide, reduced graphene oxide, and multi-layered graphene, called graphene nanoplatelets, and each of these graphene subvariants have found effective use cases, such as reinforcing polymers [60], cements [61], metals [62,63], and carbon fibers [64], amongst many others. The simplest and most economical method of graphene production to date involves liquid-phase exfoliation of graphite into graphene nanoplatelets. This

is most commonly accomplished via high-shear mixing [65] and/or ultrasonication [66], and the efficacy of these methods is highly influenced by the exfoliation media selected for these processes [67–69]. Liquid-phase dispersions of graphene are a convenient means of incorporating these particles into polymer composites, especially those that require liquid-phase processing in organic solvents, such as wet spinning of polyacrylonitrile fibers used in carbon fiber production, or gel spinning of UHMWPE fibers. The latter case is a core focus of the research in this dissertation.

3.2. Challenges in Polymer/Graphene Nanocomposites

Realizing the promise of polymer nanocomposites is challenging due to the self-attractive nature of graphene sheets and the importance of the graphene/polymer interface. Strong Van der Waals attraction between graphene layers encourages the agglomeration of graphene sheets into graphite-like particles. The desirable properties of the graphene decline significantly with increasing degree of agglomeration [70], and large agglomerated particles serve as stress concentrating defects in the polymer matrix rather than reinforcements. In liquid suspensions, this can be overcome by selecting a solvent with such an affinity for graphene that the particles remain separated [68], by including a surfactant in the solution such as sodium cholate [71,72], or functionalization with soluble polymers such as poly(vinyl alcohol) [73]. However, transferring these dispersions into a polymer matrix without inducing agglomeration is difficult, especially for thermoplastics that are conventionally processed in the melt phase. It has been found that inducing extensional (or elongational) flow can apply the shear forces necessary to disaggregate nanoparticles in polymer melts, but this requires complicated extruder screw designs and cost-intensive multi-screw extruders [7,74–76]. These challenges can be avoided in solution processing of polymers because the low viscosity of the solution enables the use of shear mixers and ultrasonication to disperse the graphene amongst the polymer molecules. Solution processing is

not possible or economically feasible for all polymers, so those that inherently require dissolution for processing, such as wet or gel spun fibers, present a natural opportunity. However, the solution must be designed to prevent graphene agglomeration in addition to dissolving the polymer, which requires a suitable solvent or surfactants that will not have adverse effects on the polymer-nanoparticle interface.

Even a well-dispersed polymer nanocomposite will underperform expectations if the polymer/nanoparticle interface is poor [77]. Molecular bonding between graphene sheets and the polymer matrix is highly dependent on the polymer molecular structure. Commonly used thermoplastics, such as polyolefins, form non-covalent bonds with graphene, and while polymers with aromatic rings can form π-π stacking bonds, linear chain polymers form weak CH-π bonds [78]. This has encouraged extensive research into the graphene functionalization and polymer grafting for improved interfacial bonding towards strong covalent bonds, but these efforts oftentimes require complex chemistries that must be specifically tailored to the polymer matrix of interest [79]. However, the polymer molecular structure is not the sole predictor of its interaction with graphene. Local alignment of polymer chains, crystallite nucleation, and confinement all play a role in the properties of the nanocomposite [80].

4. Reducing Environmental Impact and Cost in High-Performance Fiber and Nanocomposite Production

Carbon fiber reinforced composites are notoriously expensive largely due to the cost of producing the carbon fibers themselves [42]. Carbon fiber production is expensive and environmentally costly due to the vast amounts of volatile organic solvents required for the precursor fiber wet spinning process and the energy intensive oxidation and carbonization processes required to convert those fibers to carbon fibers [42]. UHMWPE fiber production lacks the latter thermal processes of carbon fiber production but requires significantly more harmful

petrochemical solvents due to the low concentration of UHMWPE that can be used during gel spinning of the fibers. Low-cost graphene nanoparticle production via liquid-phase exfoliation is similarly solvent intensive due to the low solution concentrations required for effective exfoliation and stable dispersion of the particles [65,68]. However, several avenues to reducing these fiscal and environmental costs have been identified in recent years.

4.1. Bio-derived Solvents for Ultra-High Molecular Weight Polyethylene Fiber Gel Spinning

Bio-derived solvents have received growing attention to supplant petrochemical solvents and improve the sustainability of solvent-intensive processes ranging from pharmaceuticals to polymer manufacturing [81,82]. This effort has extended to UHMWPE fiber spinning in recent years, but it remains a nascent area of research. In 2015, Schaller *et al.* [83] showed that natural oils, such as peanut or olive oil, and fatty acids, such as lauric or stearic acid, could act as "poor" solvents for UHMWPE. These poor solvents enabled fiber spinning with significantly higher polymer concentrations while maintaining mechanical properties equivalent to commercially produced UHMWPE fibers showing that high throughput could be achieved with lower environmental impact. Conversely, the authors also showed that fibers with far superior mechanical properties could be produced at the same polymer concentration as industrial UHMWPE methods. These natural solvents nonetheless required an extracting solvent. Isopropanol and diethyl ether were used in the study, and supercritical CO_2 was suggested as an option for lower environmental impact [83–86]. Pre-swelling of UHMWPE in a solvent, such as decalin, prior to spinning in paraffin oil has been shown to significantly improve the properties of the resulting fibers [87]. Recently, olive oil was blended with decalin and used to pre-swell UHMWPE particles for enhanced polymer chain disentanglement preceding fiber spinning with paraffin oil, which resulted in 24% and 32% increases in tenacity and tensile modulus respectively [88]. Greater mechanical properties may

reduce the total volume of UHMWPE fiber required for a given application, but the petrochemical solvent intensity in the production process remains the same.

Avoiding petrochemical solvents altogether can be accomplished by using orange terpenes, a food-grade bio-solvent derived from orange peel waste, which was first demonstrated by Abdul Waqar Rajput in a 2013 dissertation and two subsequent publications [89–91]. UHMWPE powder was dissolved in orange terpenes and extruded from a 1 mm diameter die into a water coagulation bath. The solvent was fully removed via immersion in water and evaporation in air without any extraction solvent, which makes this process very attractive for more sustainable UHMWPE fiber production [90]. The resulting fibers were cylindrical and exhibited relatively poor tenacity, 0.26 cN/dtex. The Taguchi design of experiments method was employed to assess the significance of feedstock particle size, solvating temperature, polymer concentration in the solution, and post-solvation heating time. It was found that post-solvation heating time and polymer concentration had the greatest positive effect on tensile strength although it was not a net improvement over the initial results [91]. The greatest improvement in fiber properties arose from ultrasonication of the UHMWPE-orange terpenes solution prior to extrusion. The fibers exhibited a flat profile and significantly improved tenacity, 1.69 cN/dtex [89]. Fiber drawing at rates ranging from 1:1 to 5:1 was applied to fibers spun from orange terpenes with and without ultrasonic treatment to assess the effect of the ultrasonication on molecular orientation. It was found via polarized light birefringence analysis that the samples spun from ultrasonicated polymer solutions exhibited increased molecular alignment after drawing, but no morphological assessment or mechanical properties were presented.

Such bio-derived solvents may simultaneously enable the formation of well-dispersed polymer nanocomposites. The gel spinning method for UHMWPE fiber production presents an interesting

advantage in this regard. Melt-phase incorporation of nanoparticles into thermoplastics results in deleterious agglomerations due to the high viscosity of the melt [92,93]. Overcoming this requires the use of complex and capital-intensive melt extruders, sometimes possessing as many as eight screws [75], or additional processing steps, such as cryomilling the matrix or coating the nanofiller [94]. Alternatively, even and stable liquid-phase dispersion of carbon nanoparticles can be achieved quickly and easily with simple shear mixing and ultrasonication equipment if a conducive solvent is selected [68,73]. This dispersion may be translated to the polymer matrix once the polymer is dissolved into the solvent/graphene solution. Consequently, the solvent selected for this purpose must be both a suitable solvent for dispersing the nanoparticles and solvating the polymer.

4.2. Commodity Polymers as Low-Cost Carbon Fiber Precursor Materials

Synthetic plastics have replaced natural and metallic materials in many applications since their invention in the 1930's due to their highly tunable and desirable mechanical and chemical properties. This flexibility led to the domination of PAN for carbon fiber production and offers opportunities to supplant PAN with a low-cost alternative. For instance, high-performance poly(p-phenylene-2,6-benzobisoxazole) (PBO, tradename Zylon) fibers can be converted into carbon fibers without the thermo-oxidative stabilization required for PAN-based carbon fibers [95–97]. However, the fibers are expensive to produce, because the polymerization of PBO is complex and the fibers must be dry-jet wet spun [98–100]. Additionally, the resulting carbon fibers have only attained modest mechanical properties to date [95]. Thus, research attention has turned to the conversion of melt-spinnable, commodity thermoplastics to replace PAN.

Commodity thermoplastics are those that are made in the greatest volume worldwide and are thus common and inexpensive. This classification typically includes polyolefins, poly(vinyl chloride), polystyrene, polyesters, and polyamides [101,102]. Unlike pitch and bio-precursors,

synthetic plastic fibers can be produced with high molecular and microstructural homogeneity, and unlike melt-spinnable PAN, the process can achieve fibers without voids at ambient environmental conditions with simple equipment. The major challenge to the use of commodity melt spinnable synthetic polymers as carbon fiber precursors is that their chemical structure is typically insufficiently stable for the thermal processes required for conversion to carbon fibers. Researchers have made great progress developing methods of overcoming this challenge in many polymers including polyolefins, polyamides, polystyrene, polyester, and poly(vinyl chloride) [50].

Polyolefins are the most produced thermoplastic in the world and this family includes polypropylene and polyethylene (PE). The combined production of all classifications of PE accounts for approximately 30% of global plastic production making it one of the most widely available commodity plastics on the market. Accordingly, PE has received great attention from the academic and commercial realms as a potential alternative carbon fiber precursor. In 1978, Shozo Horikiri [103] published the first patent to manufacture PE-derived carbon fibers using the sulfonation method most commonly used today. Since then, many grades of PE have been successfully converted into carbon fibers including LLDPE [104–106], LDPE [107], HDPE [108,109], and UHMWPE [110,111]. This attention is well warranted; in 2019, Choi et al. [42] estimated that PE-derived carbon fibers could cost 38% less than PAN-derived carbon fibers due to the low cost of PE and the melt spinning process. The methods of converting PE to carbon fibers have been reviewed as recently as 2022 by Roding et al. [112], which will be built on in this section. PEs do not inherently possess the thermal stability required for successful carbon fiber conversion, so a method of crosslinking the polymer chains of the precursor fibers is required. Many methods of crosslinking PEs have been developed for many purposes and a subset of those have been applied to carbon fiber synthesis. Sulfonation has emerged as the leading stabilization

method for PE-derived carbon fiber synthesis, which will be reviewed in the following section, and several promising alternatives that have arisen recently will be discussed afterwards.

4.3. Carbon Fibers Derived from Sulfonation Stabilized Polyethylenes

Sulfonation is the process of exposing PE fibers to high-concentration sulfuric acid at elevated temperatures. Sufficiently sulfonated PE fibers can proceed directly to carbonization without further thermo-oxidative stabilization. The 1978 patent by Horikiri et al. [103] is credited as the first demonstration of this process, and the mechanical properties they reported, up to 147 GPa elastic modulus and 2.53 GPa tensile strength, initiated decades of subsequent investigation. Pioneering academic studies conducted in the 1990s shed some light on the chemical, mechanical, and microstructural evolution of sulfonated PE into carbon fibers. Postema *et al.* [106] melt spun LLDPE fibers and stabilized the fibers via exposure to chlorosulfonic acid at room temperature. Infrared spectroscopy revealed the formation of sulfonic-group bridges, which indicated that treatment with sulfuric acid could achieve the same crosslinking effect. The fibers were then carbonized at 900℃ for 5 min under constant tension, and the final fibers exhibited a tensile strength of 1.15 GPa and Young's modulus of 60 GPa. The chlorosulfonation process induced axial and radial cracks on the surface of the stabilized fibers, and the carbonized fibers exhibited an amorphous microstructure with significant surface defects. In a series of publications from 1993 to 1996, Zhang [111] with Bhat [110] and later with Sun [113] demonstrated the production of carbon fibers from sulfonation stabilized PE and explored the effects of fiber molecular weight, molecular order, and sulfonation parameters on resulting carbon fiber properties. In 1993, Zhang [111] showed that UHMWPE could be converted to carbon fibers via sulfonation at 130-160℃ for at least 75 min. The resulting carbon fibers exhibited a tensile strength of 2.1 GPa and Young's modulus of 210 GPa with densified cross sections. Zhang and Sun [113] showed that high

temperature sulfonation is required for full stabilization, and that improper sulfonation would yield a hollow core where the polymer had been insufficiently stabilized and burned away during carbonization. In this study it was also shown that the molecular order of the precursor affects the required time for complete sulfonation; the less-ordered, highly drawn PE precursor fiber could be sulfonated in as little as 45 minutes compared with the 75 min minimum found for UHMWPE precursor fibers in Zhang's earlier study. The mechanical properties of carbon fibers were also shown to be directly related to sulfonation temperature; increasing the sulfonation temperature from 130℃ to 180℃ yielded greater mechanical properties [113]. The mechanism underlying sulfonation-induced crosslinking was proposed in 2013 by Younker et al. [114] and demonstrated in 2015 by Barton et al. [115]. Younker et al. [114] proposed a radical chain reaction wherein sulfonic groups on the polymer chain, introduced by the sulfuric acid, decompose into a hydroxyl radical and hydroxysulfonyl radical. The former abstracts hydrogen from the polymer while the latter further decomposes into another hydroxyl radical, which removes more hydrogen and sulfur dioxide to complete the cycle. The resulting aromatic structure is then sufficiently stable to conduct carbonization, which drives off the remaining noncarbon elements, Figure 4.

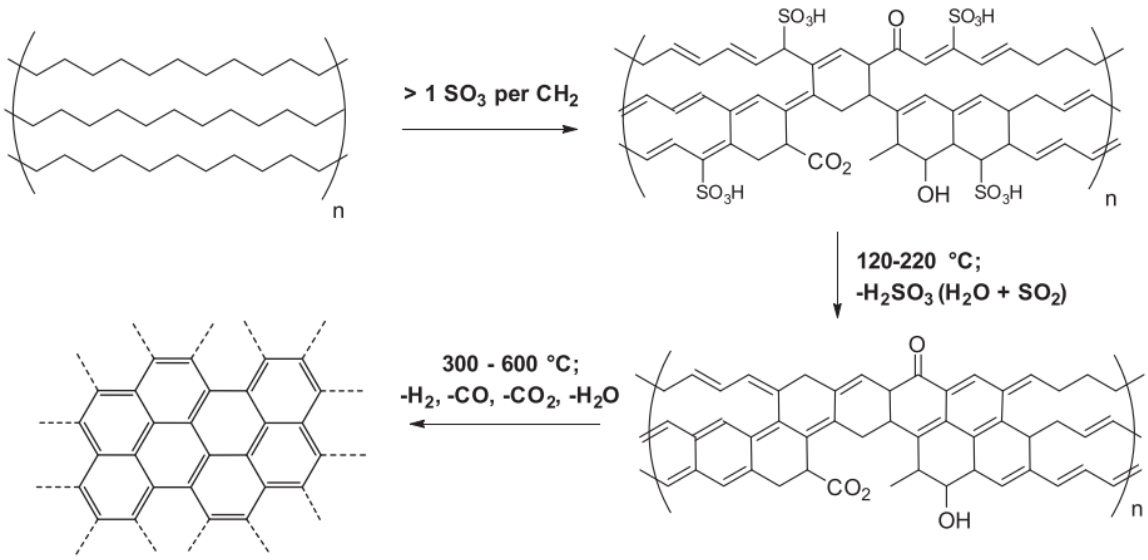

Figure 4. *Schematic of the transformation of PE into carbon* [115]

Barton et al. [115] confirmed this mechanism by identifying sulfonic groups on PE fibers sulfonated with sulfuric acid via Fourier transform infrared spectroscopy, the evolution of sulfur dioxide and water vapor during carbonization via evolved gas analysis-gas chromatography, and a decrease in S=O bonds via attenuated total reflectance infrared spectroscopy.

After settling the mechanism of sulfonation, Barton joined Behr *et al.* [116] in establishing a structure-property model for PE-derived carbon fibers in 2016. The authors conducted a series of experiments synthesizing carbon fibers from HDPE at carbonization temperatures ranging from 900℃ to 2400℃. Single-fiber tensile tests were used to determine the mechanical properties of the carbon fibers. Wide-angle X-ray diffraction was used to assess the orientation of graphitic layers. These results were used to apply Northolt et al.'s [117] uniform stress structure-property model for PAN-derived carbon fibers. The authors were able to show that the relationship between microstructure orientation and tensile modulus is different from each PAN- and pitch-derived carbon fibers and the shear modulus between graphitic layers of PE-derived carbon fibers was lower than both. This insight implies that the crosslink density in PE-derived carbon fibers is lower, which could indicate a greater propensity for orientation during graphitization and thus greater mechanical properties. This relationship can be used to estimate the level of orientation required to achieve high properties or predict properties based on an observed level of orientation. Critically, their experimental results can be extrapolated to show that highly oriented PE-derived carbon fibers could achieve tensile properties that meet or exceed PAN-derived carbon fibers, Figure 5 [116]. Expanding on their previous work, Barton and Behr [118] recently utilized a graphitization process with the addition of boron to yield LLDPE-derived carbon fibers with a tensile modulus greater than 400 GPa when graphitized at 2400 ℃. The boron additive was shown

to reduce the necessary temperature for graphitization and produces fibers with superior modulus at lower temperatures.

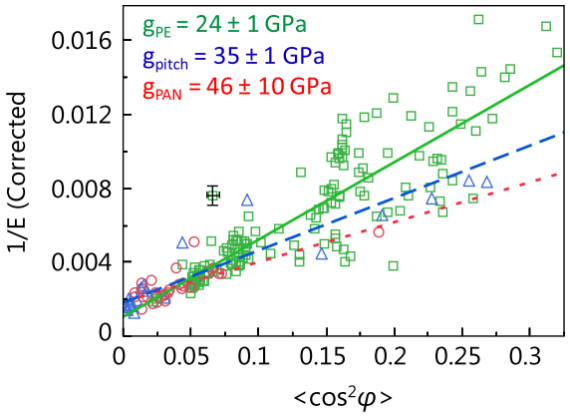
g_{PE} = 24 ± 1 GPa
g_{pitch} = 35 ± 1 GPa
g_{PAN} = 46 ± 10 GPa
1/E (Corrected
0.016
0.012
0.008
0.004
0
0
0.05
0.1
0.15
0.2
0.25
0.3
<cos²φ>
Figure 5. *Compliance (1/E) vs. orientation parameter for PE- (green squares), PAN- (red circles), and pitch- (blue triangles) derived carbon fiber. Shear moduli calculated from the data for each type are included. Note that the tensile moduli for the PE-derived carbon fiber are corrected for porosity, and the error bars were estimated from replicated measurements of the same fiber* [116]

Many aspects of the precursor fibers and the processing conditions affect the properties of the PE-derived carbon fibers. Sufficient sulfonation is the most important factor in synthesizing carbon fibers from precursors, and it has been shown that the diameter of the precursor fiber, fiber crystallinity, and the sulfonation temperature are inversely proportional to the required sulfonation time [105,108]. Recent advances in the sulfonation process, such as applying hydrostatic pressure, up to 5 bar, have been used to increase the rate of sulfuric acid penetration into the precursor fibers to accelerate the sulfonation process and overcome limitations induced by the crystallinity of the precursor fibers [119]. Reducing precursor fiber diameter also results in increased carbon fiber mechanical properties [104], as does careful control of tension applied to the fibers during sulfonation and carbonization [105]. Applying tension during conversion processing increases the degree of alignment in the carbon chains that make-up the backbone of carbon fiber, which has a direct correlation to increased mechanical properties and the anisotropic microstructure of the carbonized fiber.

Although sulfonation stabilized-PE derived carbon fibers show great promise, it must be acknowledged that the sulfonation process is costly and ecologically unfriendly because the best results require the use of high- or fuming-concentration sulfuric acid at high temperature. Accordingly, recent research has focused on the application of electron beam irradiation to lower the requirements for successful stabilization via sulfonation. In 2019, Choi et al. [120] were the first to demonstrate the production of carbon fibers from PE precursors that were pretreated with electron beam irradiation prior to sulfonation. In their work, the LLDPE precursor fibers were exposed to 500-1500 kGy prior to sulfonation in 98% sulfuric acid at 95°C followed by carbonization. The resultant carbon fibers exhibited functional mechanical properties of 1.3 GPa tensile strength, 89.9 GPa tensile modulus, and 1.5% elongation at break as well as a carbon yield of 44.6% for fibers pretreated with 1500 kGy irradiation. In addition to greatly reducing the sulfuric acid concentration and temperature (from 120% to 98% and 140°C to 95°C respectively), the authors were also able to achieve these results in one less hour of sulfonation duration [120]. In 2021, Kang et al. [121] performed a similar procedure with HDPE precursor fibers and achieved a carbonization yield of 40% with consistent, densified cross-section fibers, but did not publish mechanical properties for the carbon fibers.

4.4. Alternative PE Stabilization Methods

Despite the promising results of sulfonated-PE-derived carbon fibers, the challenges of the sulfonation process, well exemplified by the complex multiphase reactor developed by Hukkanen et al. in 2018 [122], Figure 6, have led researchers to explore alternative PE stabilization pathways. Some well documented methods, such as peroxide crosslinking, silane crosslinking, and irradiative methods without sulfonation, yield crosslinking densities too low for carbonization [123], whereas others, such as halogenation, ammoxidation, and sulfurization have shown potential.

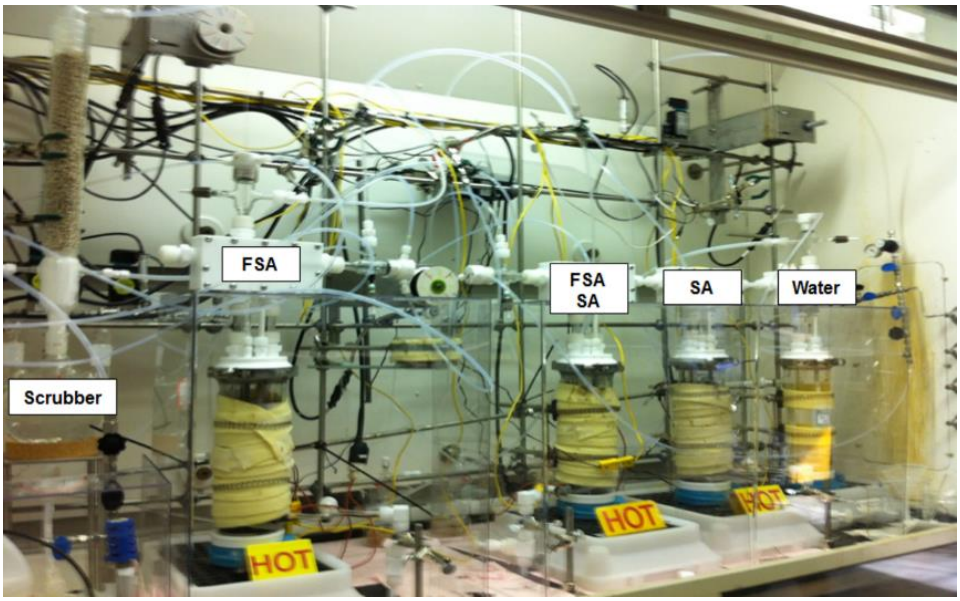

Figure 6. *Example of a continuous fiber sulfonation reactor system for sulfonating tows of polyethylene fibers for carbon fiber production. Reprinted with permission from* [122]*. Copyright 2018 American Chemical Society*

The highly reactive nature of halogen elements creates an attractive opportunity to strip the hydrogen from polymer chains to form carbon fibers. Generally, the halogen attaches to the hydrogen atoms of the polymer to form hydrohalogens, and a succeeding dehydrohalogenation process removes these molecules to reveal a carbon-only structure. A pathway to converting chlorine-saturated PE into carbon fiber was introduced as early as 1972. Saglio et al. [124] demonstrated that LDPE saturated to 73.7 wt% chlorine could be wet spun and converted into carbon fibers through a thermal dehydrochlorination process followed by carbonization. The resulting carbon fibers displayed turbostratic carbon regions after a carbonization stage conducted at 800°C and graphitization was possible at much higher temperatures. This conversion method leaves much to be desired due to the wet spinning fiber formation method, the substantial consumption of chlorine, and significant generation of HCl gas, and was thus abandoned in favor of sulfonation.

Halogenation was revisited recently by Laycock *et al.* in 2020, [125] who demonstrated the pyrolysis of brominated PE fibers and proposed a possible conversion mechanism, shown in Figure

7. The authors brominated melt spun PE fibers, and blends of PE with other materials such as kraft lignin, under ultraviolet irradiation and converted the brominated precursors into carbon fibers through a two-stage process involving a dehydrobromination at 180℃ followed by carbonization at ≥ 800℃. Dow ASPUN LLDPE, metallocene LLDPE, HDPE, and LDPE were all used in this study. Carbon yields greater than 90% were achieved, but the fiber morphology could not be retained due to its solubility with liquid bromine. Such a high carbon yield is attractive and the ability to recover and reuse bromine from the process makes this method promising, so the authors acknowledge that future work will involve the exploration of gas-phase bromination to maintain fiber morphology for carbon fiber production.

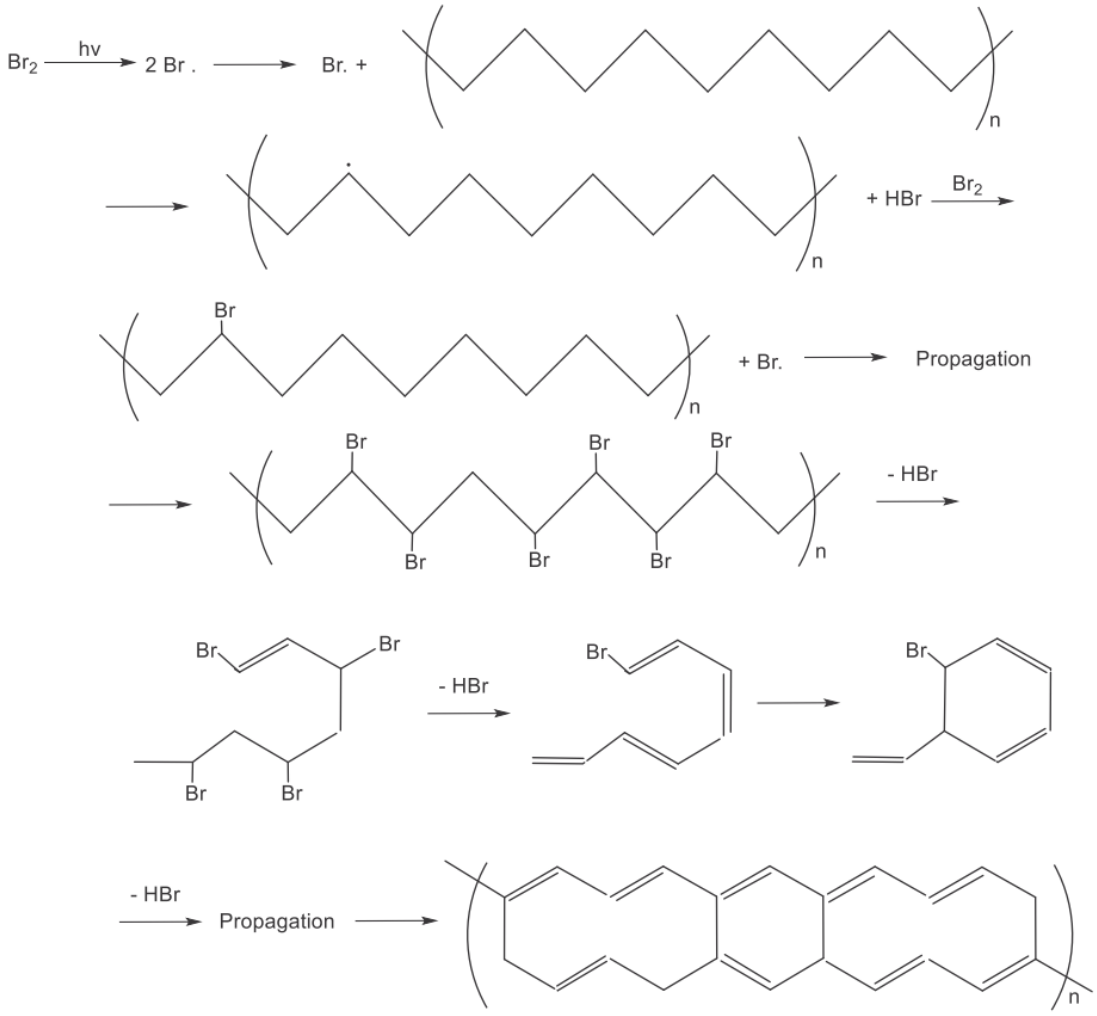

Figure 7. *Proposed mechanism for the conversion of PE into carbon fibers via bromination* [125]

In pursuit of an air-oxidation method, in 2018 Barton *et al.* [126] discovered that ammoxidized silane grafted-PE could be converted to carbon fibers with a carbon yield up to 70%. The authors formed crosslinked PE film and fibers by immersing LLDPE graft vinyl trimethoxysilane (PE-g-VTMS) in a sulfonic acid catalyst and then heating in air at 100% humidity. The initial intent was to demonstrate an air oxidation method of the crosslinked PE-g-VTMS, but lackluster results prompted the exploration of ammoxidation as an alternative. Samples that were immersed in air-sparged 5M anhydrous ammonia prior to oxidation demonstrated aromatic structures and high mass retention after oxidation and carbon yields up to 70% after carbonization. The resulting carbonaceous material was largely amorphous but graphitic regions were evident via high resolution transmission electron microscopy (HRTEM), Figure 8a. Although the precursor morphology was identifiable after pyrolysis, the fibers were fused together after oxidation, Figure 8b. Therefore, this method requires more development to realize its potential as an alternative to high temperature sulfonation.

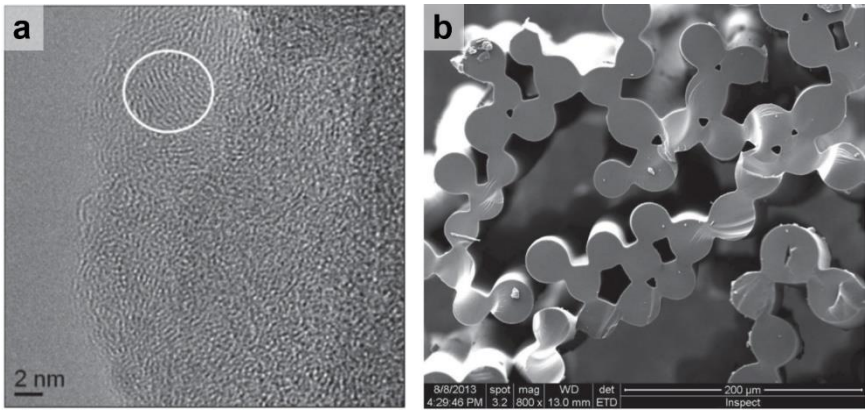

Figure 8. *a) HRTEM image of an ammoxidation-stabilized carbon fiber exhibiting graphitic regions including extended stacking of lattice fringes in the encircled region, and b) SEM image of the cross section of fused, carbonized PE fibers* [126]

The latest development in alternative stabilization methods for PE involves elemental sulfur rather than sulfuric or sulfonic acid. In 2021, Frank *et al.* [127] irradiated various grades of PE fiber with an electron beam and then sulfurized the fibers in molten elemental sulfur. The

irradiation step provides sufficient initial crosslinking for immersion in the molten sulfur at temperatures greater than 240°C. Sulfurization was first shown to convert PE into a semi-aromatized material containing poly(thienothiophene) and poly(naphthothienothiophene) blocks by Trofimov *et al.* in 2000 [128]. Frank *et al.* [127] applied this chemistry to their precursor PE fibers and then successfully carbonized the resulting fibers. Carbon yields up to 76% were achieved and the synthesized carbon fibers showed dense cross sections with few voids, Figure 9. The carbon content of the resulting fibers was measured to be 98.7%, thus the input sulfur could be considered entirely removed. The authors noted that sulfur-capture technology has long been matured due to extensive use of the vulcanization process at industrial scale, so input sulfur can readily be captured and re-used. The authors did not publish mechanical results and cited a need for production scale-up of the process to truly demonstrate the mechanical characteristics of carbon fibers produced in this method.

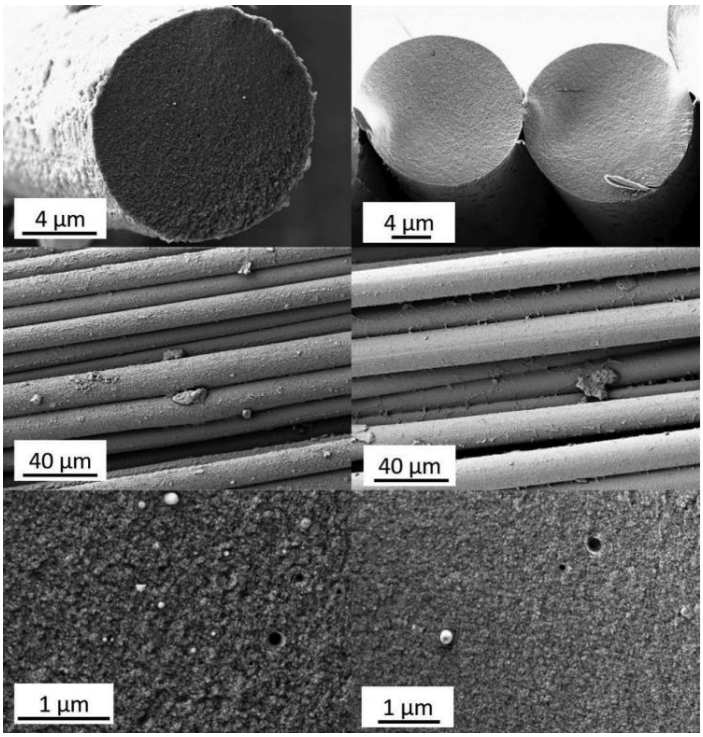

Figure 9. *SEM images of carbon fibers derived from sulfurized HDPE (left column) and sulfurized LDPE (right column) showing the resultant morphology including smooth exterior surfaces and minor voids and inclusions* [127]

5. Summary and Primary Research Questions

Fiber- and nanoparticle-reinforced composites offer the specific strength and stiffness needed to supplant denser metals in vehicle construction for significant energy efficiency gains. The high strength and stiffness of carbon and UHMWPE fibers are highly desirable for high-performance fiber-reinforced composites, but producing these fibers is costly and environmentally unsustainable. For carbon fibers, this may be addressed by using alternative precursor materials, such as polyethylene that can be spun into fibers at significantly greater throughput without the use of petrochemical solvents. For UHMWPE fibers, this may be resolved in part by replacing the solvents required for UHMWPE gel spinning with renewable alternatives. Polymer nanocomposites reinforced with graphene promise outstanding multifunctional properties, but the incorporation of the nanoparticles into the polymer matrix presents challenges in maintaining an even particle dispersion and tailoring the polymer/graphene interface for maximum load transfer. Solution processing of polymer nanocomposites can be used to overcome this issue if an appropriate solvent for both polymer dissolution and graphene dispersion is selected, and a bio-derived solvent is highly desired to reduce environmental impact. In all cases, there is much to be learned about how these alternative methods affect the microstructure and properties of the resultant materials, and the research efforts reported in this dissertation represent a step towards understanding these relationships. This gives rise to three primary research questions.

What is the effect of tension during sulfonation stabilization of PE-derived carbon fiber?

UHMWPE has been converted into carbon fibers in the past with promising results [110,111,113], and the authors of these publications acknowledged that optimizing the tension applied during the sulfonation stabilization of these fibers is crucial to maximizing mechanical properties. Yet, recent research has focused on the conversion of lower molecular weight variants

of PE, and the effect of tension applied during the sulfonation stabilization of PE remains unresolved. It is hypothesized that the long and highly ordered molecular chains of UHMWPE may enable superior graphitic structure development during carbon fiber conversion if the sulfonation tension can be tuned to maintain this alignment. Understanding the effect of this processing parameter on the evolution of the microstructure and properties of UHMWPE-derived carbon fibers will demonstrate pathways to maximize the performance of these fibers and will provide crucial insights to advance the development of carbon fiber synthesis from commodity-grade polyethylene precursor fibers as well [50].

What are the properties and potential of UHMWPE fibers spun using orange terpenes?

Current literature regarding UHMWPE fibers spun using bio-derived solvents that do not require solvent extraction, specifically an orange fruit byproduct called orange terpenes, lacks detailed information regarding the microstructure and properties of the fibers [90]. Gaining an understanding of the evolution of the microstructure during the spinning and drawing processes is critical to understanding the potential of this gel spinning method for making high-performance fibers that can rival those produced using petrochemical solvents. Probing the process-structure-property relationships underlying this material sets a baseline for optimizing this process and for exploring other bio-derived solvents that could be used for dry-extraction gel spinning of UHMWPE with additional benefits, such as higher polymer concentration, improved gelation/crystallization kinetics, or suitability for nanoparticle dispersion.

How does graphene affect the microstructure and properties of UHMWPE fibers spun using bio-derived solvents?

Carbon nanoparticles, such as graphene and carbon nanotubes, have been used to reinforce and augment polymers, thereby forming polymer nanocomposites, for over thirty years due to the exceptional properties of the nanoparticles [129]. However, little information is available on

UHMWPE nanocomposite *fibers*. It has been shown in other polymers that the fiber spinning process can preferentially align the nanofillers along the fiber axis [130], and that graphene can locally align polymer molecules along the graphene sheet [64] both improving mechanical properties. This begs the question: How does graphene affect the microstructure and properties of UHMWPE fibers spun using bio-derived solvents? It is hypothesized that graphene may aid in bridging the amorphous regions and reinforce the tie molecules that connect the crystalline phases in the UHMWPE thereby enhancing the strength and stiffness of the fibers [131]. However, the growth of lamellar crystals during gel spinning and extension of those lamellae into extended chain crystals during drawing is crucial to the development of the mechanical properties of the polymer fiber. The influence of graphene particles on these processes is not well understood.

Each of these questions will be answered through the next three chapters of this dissertation, and a summary and recommendations for future work based on these results will be covered in the final chapter. The results presented in Chapters 2 and 3 have been published in the Journal of Polymer Research [132] and Polymer Science & Engineering [133] respectively, and a version of Chapter 4 is under review for publication in Advanced Composites and Hybrid Materials, as of the time this dissertation was published.

Chapter 2. Effect of Tension Applied During Sulfonation Stabilization for UHMWPE-derived Carbon Fibers

1. Introduction

The process of synthesizing carbon fibers from sulfonation-stabilized polyethylene (PE) has received great attention since it was first patented in 1978 [103]. PE is much more abundant and less costly compared to the commercially dominant carbon fiber precursor, polyacrylonitrile (PAN), and has shown the greatest promise in terms of carbon fiber mechanical properties of the general population of commodity polymers that have been investigated as alternative carbon fiber precursors [50]. Although early work led by Dong Zhang [110,111,113] demonstrated carbon fibers with high mechanical properties derived from highly aligned PE (UHMWPE), research focus has shifted towards linear low density polyethylene (LLDPE) and high density polyethylene (HDPE) in recent decades [112]. This is attributed to the relatively long sulfonation stabilization duration required by the slow diffusion of sulfuric acid through the highly crystalline microstructure of UHMWPE [112]. However, increasing precursor molecular weight and molecular alignment has been shown to increase the mechanical properties of the resultant carbon fibers [116,134]. So, the high molecular weight and highly aligned molecular structure of UHMWPE fibers may present an opportunity for greater graphitic alignment and thus greater mechanical performance in the resulting carbon fibers. Maintaining this alignment throughout conversion requires the application of tension during stabilization and carbonization to reduce or prevent the occurrence of chain relaxation and shrinkage. This process is complicated for PE-derived carbon fiber production by the elevated temperature required to successfully stabilize the precursor fibers via sulfonation. At elevated temperatures the precursor fiber mechanical properties decline precipitously [135], which limits the amount of tension that can be applied. Kim and Lee [136] encountered this problem when studying the effect of processing parameters on the

conversion of LLDPE. The max stress the authors could apply to LLDPE fibers during sulfonation was 0.26 MPa. Herein lies another advantage for UHMWPE as a precursor: it has the greatest mechanical properties of all PE variants. Therefore, it presents an opportunity to apply greater tension during sulfonation and carbonization to maintain high molecular alignment that could translate to the final carbon fibers.

Zhang and Sun acknowledged that optimization of sulfonation tension could be the key to leveraging the high order of UHMWPE precursors [113], but prior to this work no study had been published probing this hypothesis. Herein, the effect of tension during the conversion of commercially available UHMWPE to carbon fibers is explored to test this hypothesis and explore the morphological, microstructural, and mechanical property evolution of PE-derived carbon fibers. A baseline conversion protocol was established for the selected UHMWPE precursor fiber, and then a logarithmic sweep of the sulfonation tension was performed, ranging from 0.1 MPa/filament tensile stress to 10 MPa. The fibers were then carbonized and characterized via thermal, microstructural, and mechanical characterization techniques to probe the chemical and structural evolution of the UHMWPE fibers to carbon fibers.

2. Experimental Methods

2.1. Materials

Dyneema SK60 UHMWPE fibers with a nominal diameter of 12 μm (880 dtex, 780 filaments/tow, 0.96 g/cm^3 density, manufactured by DSM) were selected for this study. Histological-grade acetone and deionized water were used for spin finish removal. 95-98% sulfuric acid was acquired from Millipore-Sigma and used without further purification for all sulfonation trials.

2.2. Sample Preparation

2.2.1. Precursor Preparation

As delivered, the precursor fibers are coated with a proprietary thin coating referred to as a spin finish. The composition of this coating is a closely kept trade secret but it may contain several compounds that offer anti-static, lubricating, antioxidant, and thermal stabilizing characteristics [137,138]. It was found that the presence of the spin finish during sulfonation stabilization has a deleterious effect on the fibers and can result in premature failure. Honeywell, a manufacturer of UHMWPE fiber, acknowledged that removal of the spin finish may be desirable in various applications and discussed methods of removal in a recent patent [139]. DSM described the spin finish on the Dyneema UHMWPE fibers used in this study as water-soluble. This is consistent with spin finish applied to other commercial fibers, so initial wash trials using only deionized water were conducted consistent with the procedures used in [140]. Additional trials using tribasic sodium phosphate, a common scouring agent for natural and synthetic fibers, were attempted based on [139,141]. Finally, routines including acetone washing and ultrasonication were explored, Table 1. Success was determined by completing a 7 h sulfonation without fiber failure. It was observed that fibers without the removal of the spin finish failed at approximately 4 h sulfonation and fibers with incomplete spin finish removal would fail in less than 5 h.

The following two-step washing method was used to remove the spin finish from the precursor fibers. First, the fibers were ultrasonicated in acetone for 30 minutes followed by a rinse with acetone and deionized (DI) water. Then, the fibers were ultrasonicated in deionized water at 60°C for 30 minutes. The fibers were then rinsed once more with deionized water, blown with air, and hung to dry in air for no less than 12 hours.

***Table 1**. Experimental spin finish removal procedures and their results*

Wash Procedure	Result
No rinse or soak	Failure at approximately 240 min
30 min stirred & ramp heated DI soak, post-rinse DI	Failure at 284 min
Rinse: acetone, methanol, ethanol, isopropanol, DI water, then 20 min ultrasonicate in DI water	Failure at 287 min
Stirred soak in 1% aq. tribasic sodium phosphate @ 60℃ for 1h. Acetone, isopropanol, then DI water rinse	Failure at 148 min
Ultrasonicated soak in 5% aq. tribasic sodium phosphate @ 60℃ for 1h. DI water rinse	Failure at 262 min
15 min stirred acetone soak, 15 min stirred DI water soak, DI water post-rinse	Successful, but fibers were brittle
Ultrasonication: 30 min acetone, 30 DI water, rinse after each step	Successful sulfonation

2.2.2. Sulfonation Stabilization

A custom Teflon and glass frame was designed and fabricated to apply deadweight tension to a continuous tow of fibers such that only straight sections without knots were immersed in the sulfuric acid bath, Figure 10. The sulfuric acid bath was composed entirely of 95-98% sulfuric acid without dilution. The amount of time it takes to completely stabilize a polyethylene fiber via sulfonation is dependent on the temperature of the sulfuric acid bath, diameter of the fiber, and several polymer characteristics such as crystallinity [112]. A series of trials of varying sulfonation time and temperature were conducted to determine the parameters necessary for completed sulfonation of the precursor fibers used in this study. Differential scanning calorimetry (DSC) was used to observe the reduction and elimination of the melting endotherm of the precursor, which indicates thermal stability. Thermogravimetric analysis (TGA) was used to identify the amount of carbonized material remaining after exposure to carbonization temperatures. Parameter sets with promising DSC and TGA results were used to make carbon fibers and scanning electron microscopy (SEM) was used to confirm that the resulting fibers had a completely densified cross section.

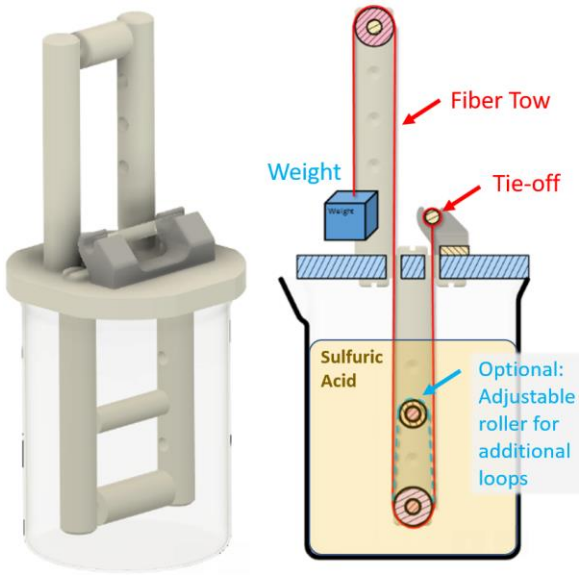

Figure 10. *Computer-aided design rendering and cutaway schematic of custom sulfonation tension application apparatus used to apply constant tension to UHMWPE tows during sulfonation stabilization*

An initial sulfonation temperature of 130℃ was selected, and the duration was increased in increments of 1h from 2 h to 5 h. The melting peak seemed to disappear at 5 h and carbonization resulted in a char yield of 46.3% (Figure S1), which is consistent with other PE-derived carbon fibers published in literature [113].

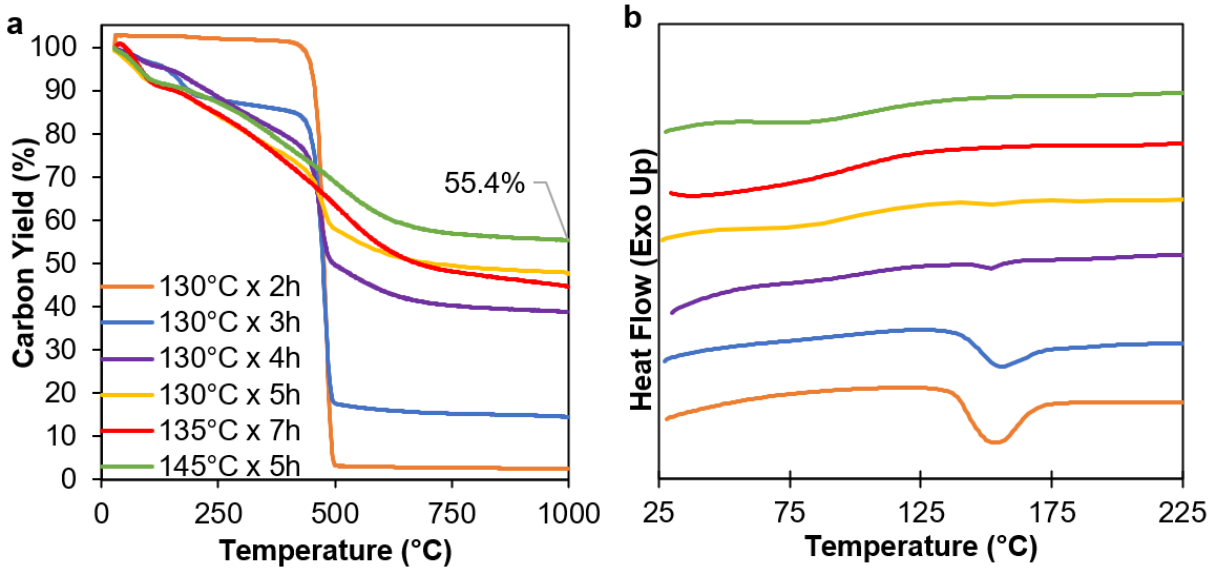

Figure 11*. a) Thermogravimetric analysis plot showing the mass reduction of the sample fibers during heating up to carbonization temperatures, and b) DSC heat flow plot showing the reduction in melting peak with increasing sulfonation time*

However, the resulting carbon fibers had a hollow core, Figure 12, which indicates that the interior of the fiber was not completely stabilized. The sulfonation temperature was then increased to accelerate the rate of diffusion of the sulfuric acid into the fibers thereby increasing the stabilization depth without increasing the stabilization time. Increasing the sulfonation temperature to 145℃ significantly increased the carbon yield to 55.4%, but the fiber tow broke in the process. Although DSC shows that the melting peak occurs at approximately 154℃, the melting endotherm begins at approximately 135℃. Therefore, 135℃ was selected as the sulfonation temperature for the remaining trials. It was then found that sulfonation at 135℃ for 7 h yielded fully densified carbon fibers that were pliable and capable of being handled for subsequent characterizations.

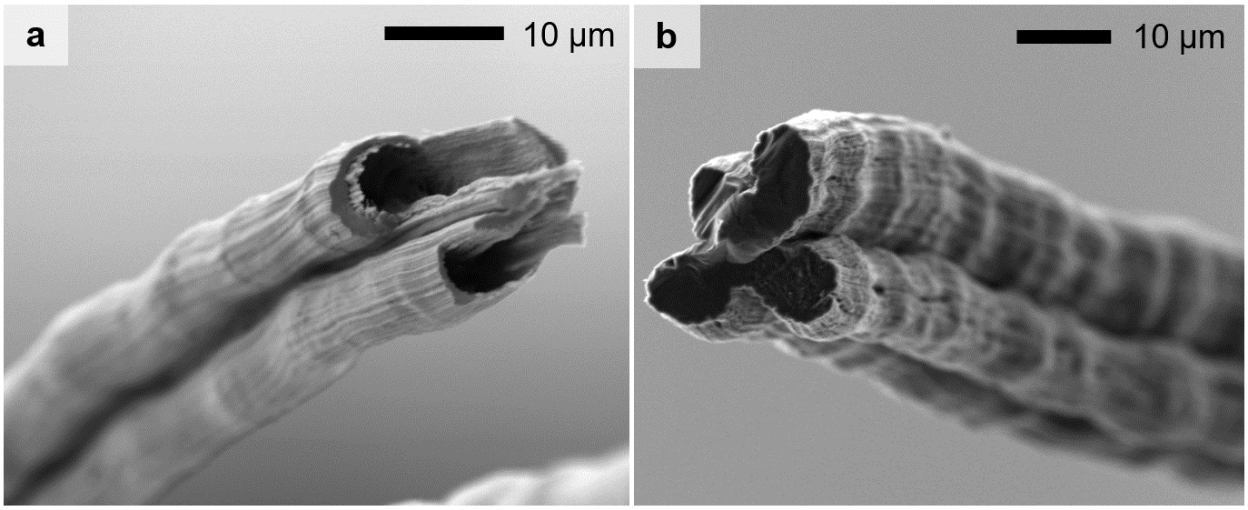

Figure 12. *a) SEM image of hollow carbon fibers resulting from insufficient sulfonation, and b) solid-cored carbon fibers indicating successful carbonization*

It was found that sulfonation at 135℃ for 7 h resulted in fibers sufficiently stabilized to yield carbon fibers with densified cross-sections, so these parameters were applied to all subsequent trials. Tension applied during sulfonation was then varied in a three-step logarithmic sweep from near-zero tension, 0.1 MPa tensile stress, to near-max tension, 10 MPa tensile stress. Trials with 20 MPa applied tensile stress resulted in fiber breakage, so the log-sweep was not extended beyond 10 MPa.

2.2.3. Carbonization

The sulfonation-stabilized fibers were converted into carbon fibers by heating to 1000°C from room temperature in an argon atmosphere at a heating rate of 3 °C/min (MTI OTF-1200X-S-VT). A graphite deadweight was attached to the fiber tow to apply 1 MPa tensile stress during carbonization for all trials.

2.3. Characterization Methods

2.3.1. Thermal Analysis

DSC and TGA were conducted using a Netzsch STA 449 F1 Jupiter Simultaneous Thermal Analyzer. Samples weighing 7 ± 1 mg were produced by cutting fibers into short pieces and pressing them into a platinum crucible for maximum contact area. The samples were then heated to 1000°C with a heating rate of 10 °C/min in an argon atmosphere.

2.3.2. Morphological Analysis

Fiber shrinkage during sulfonation was measured by analysis of digital images of a positional reference attached to the fiber tow collected every 60 seconds. A short length of precursor fiber was fully immersed in the sulfuric acid solution and attached to a chemically inert string that extended outside the bath to apply deadweight tension. A custom image analysis script was used to detect the position of a green indicator attached to that string, thus indicating the shrinkage of the tow in the bath [142]. Scanning electron microscopy (SEM, FEI Quanta 650) was used to image the fiber morphology at all stages of conversion. All non-carbonized samples were sputter coated in gold (Cressington 108 Auto/SE) to avoid charging.

2.3.3. Microstructural Analysis

Raman spectroscopy was conducted using a Renishaw InVia Confocal Raman microscope with a 50x objective lens. The laser wavelength was selected to minimize fluorescence according to

each sample. A 405 nm wavelength laser was used for the precursor UHMWPE fibers, and 514 nm wavelength laser was used on the sulfonated and carbonized fibers. The sample fibers were mounted in epoxy and sectioned to reveal radial cross sections and polished. Spectra were collected for three fibers per sample and averaged prior to baseline subtraction and normalization.

The precursor UHMWPE fibers, sulfonated fibers, and carbonized fibers were characterized via X-ray diffraction in the Debye-Scherrer configuration on a Bruker D8 Venture, equipped with Cu-Kα radiation, a Helios™ monochromator, and a Photon III 2-D detector [143]. This setup yielded a radiation wavelength of 0.154184 nm and a spot of size of 100 μm. Aligned fiber tows were inserted into low-absorbing glass capillaries of 1 mm diameter and approximately 10 mm in length. The capillaries were filled with as many fibers as possible in the interest of acquiring high signal-to-noise ratios. The carbonized fibers were sufficiently stiff and aligned well enough to allow for protrusion of the fibers out of the open end of the capillaries, allowing for a more accurate diffraction pattern with only air contributing to the background scattering. The capillaries containing the fibers, or supporting the fibers, were rotated 360° about the fiber axis for the duration of each scan.

2-D frames (0.02° 2θ resolution) were collected in equatorial and meridional configurations for all sample fibers. A blank scan of the 1 mm capillaries was collected under the same conditions as the fiber samples, and this 2-D frame was subtracted from all collected data prior to subsequent analysis [144]. In the case of the carbonized fibers, a blank scan of the air was collected and subtracted from the data. To acquire 1-D patterns, the collected scans were integrated ±20° around the azimuthal direction, horizontally along the 2-D frame (10° – 102° 2θ). Integration was performed using Bruker APEX4 software. For the equatorial scans, the fibers were rotated vertically relative to the detector and perpendicular to the 1-D integration direction, Figure. 13a.

For the meridional scans, the fibers were rotated horizontally relative to the detector and parallel to the integration direction, Figure. 13b. Using both configurations enables a broader perspective of the crystallographic texture inherent in fibers because physical limitations of the detector size required physical rotation of the diffracting crystallographic planes in the fibers. For systems with larger detectors, such as those found on synchrotrons, rotation of the fibers is unnecessary.

For all subsequent quantitative analyses of the carbonized fibers, a turbostratic layer stacking structure was assumed [145,146]. For the carbonized fibers, the azimuthal intensity distribution at the (002) peak, averaging across a 2θ width of 1°, was collected to assess crystallite orientation. The parameters extracted from the equatorial, meridional, and azimuthal scans for the carbonized fibers are explained in more detail in Section 3.3.

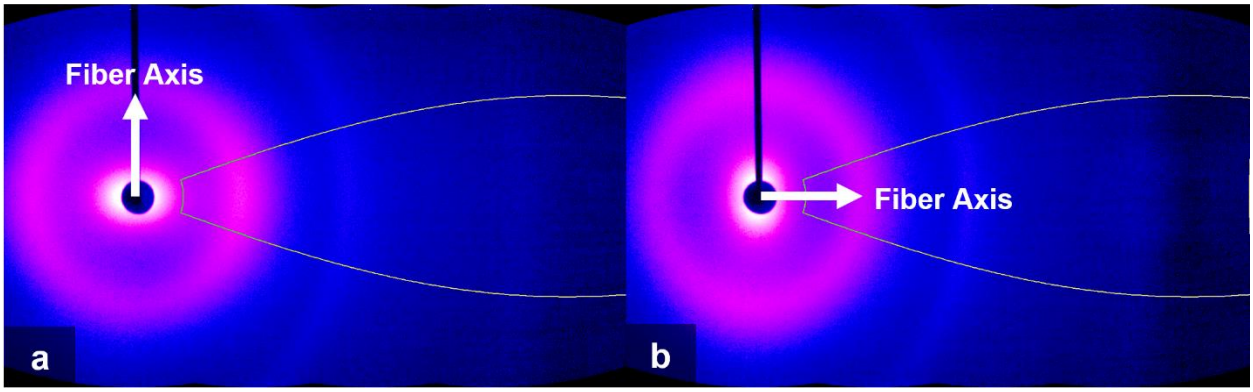

Figure. 13 *a) Equatorial 2D data frame, and b) meridional 2D data frame, with integration regions overlayed, for a carbon fiber derived from UHMWPE sulfonation stabilized under a tensile stress of 10 MPa. The fiber texture is evident through the varying intensity along the azimuthal direction*

2.3.4. Mechanical Analysis

Single-fiber tensile tests were performed according to ASTM standard C1557 with a gauge length of 10 mm using an MTS Nano Bionix UTM, which has a maximum load capacity of 500 mN and 150 mm of extension. Carbon fiber samples were tested with a strain rate of 1e-4 s^{-1} to complete the tests within the minimum time called for in the standard. The fracture surface from

each tensile test was imaged via SEM, and the cross-sectional area was measured using ImageJ to calculate the mechanical properties.

3. Results and Discussion

3.1. Thermal Analysis

DSC thermograms showed that the melting peak, at approximately 155°C in the precursor, had been eliminated in all samples regardless of applied tension, Figure 14, which indicates that the stabilization process was completed in all cases. TGA results showed that the tension applied during sulfonation can affect the ultimate carbon yield after carbonization. Fibers sulfonated under 1 MPa and 10 MPa tension exhibited similar rates of mass loss ending at a similar carbon yield, 55.3% and 56.1% respectively. However, the sample sulfonated at minimum tension, 0.1 MPa, exhibited a lower rate of mass loss and ultimately significantly higher char yield at carbonization temperatures, 68.6% Figure 14, which may be the result of virtually uninhibited chain relaxation allowing for greater penetration of the sulfuric acid and greater crosslinking.

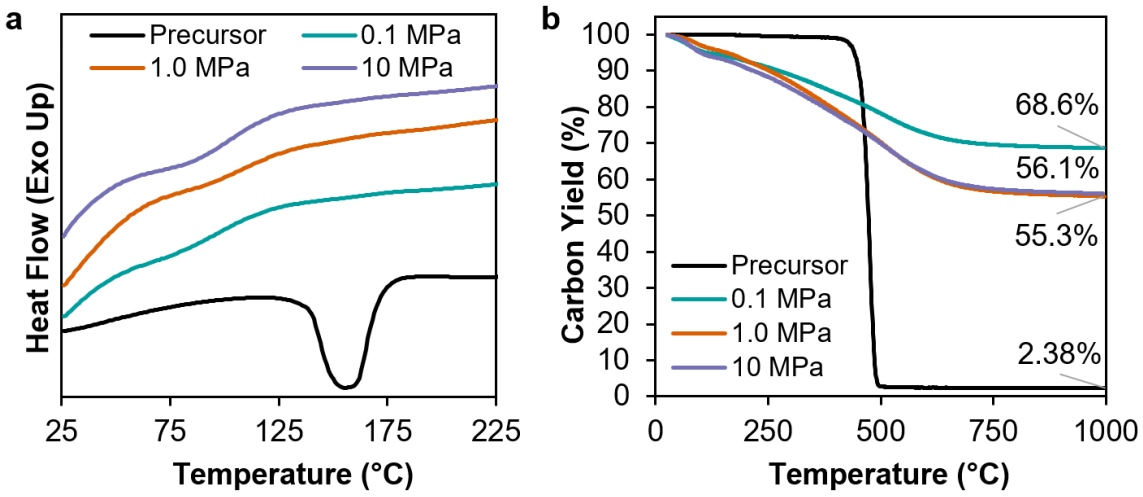

Figure 14. *a) DSC curves for the UHMWPE precursor fibers and fibers sulfonation stabilized with various amounts of applied tensile stress, and b) TGA curves showing the char yield of the same sulfonation stabilized fibers compared to the UHMWPE precursor*

3.2. Morphological Evolution

UHMWPE fibers shrink considerably along the fiber axis during the sulfonation process, so the change in length of a finite-length precursor tow was tracked during sulfonation, Figure 15. Time lapse recordings showing the physical change in the tow length over time with an adjoining plot of shrinkage are available where this work was published [132].

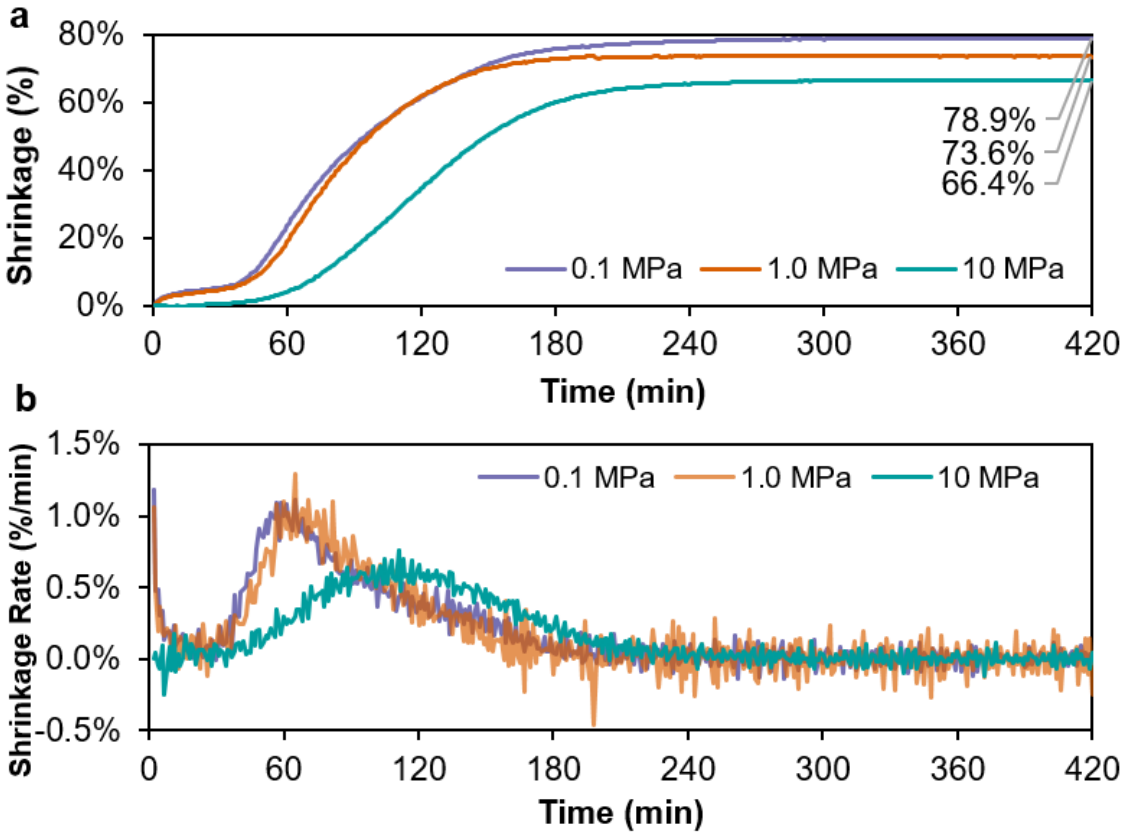

Figure 15. *a) UHMWPE precursor fiber shrinkage during sulfonation stabilization as a function of tensile stress applied during the stabilization process, and b) rate of shrinkage of the tow during the stabilization process*

Consistent with the findings of De Palmenaer's 2017 study of HDPE precursor conversion parameters, [112,147], two distinct shrinkage regimes occurred; A relatively low rate of shrinkage occurs in the first hour caused by the thermal relaxation of the polymer chains, called entropic shrinkage, then chemical shrinkage occurs at a relatively high rate until the fiber reaches equilibrium. The first regime is preceded by an instantaneous shrinkage upon contact with the bath

under 0.1 MPa and 1.0 MPa tensile stress, which was eliminated under 10 MPa tensile stress. The first regime shrinkage is approximately the same for the 0.1 MPa and 1.0 MPa stressed fibers but is eliminated when 10 MPa tensile stress is applied indicating that the applied tension has overcome the entropic shrinkage. Applying tension at 10 MPa also slowed the chemical shrinkage regime; the peak rate of shrinkage under 10 MPa tensile stress was 0.40 mm/min compared to 0.71 mm/min at 1.0 MPa and 0.59 mm/min at 0.1 MPa. Ultimately, the fibers sulfonated under 10 MPa tensile stress shrunk significantly less than the lower tension samples with a total reduction in length of 66.4% compared to 73.6% for the tow stressed at 1.0 MPa and 78.9% for the tow stressed at 0.1 MPa.

SEM was used to observe the effect of macro-scale shrinkage on the micro-scale morphology of the fibers, Figure 16. Following sulfonation, all the sample fibers exhibited a repeating pattern of swollen nodes along the length of the fiber, which has previously been acknowledged and referred to as kink bands [111]. As tension increased, the frequency and amplitude of the nodes decreased significantly. The microfibrillar structure of the UHMWPE is apparent in all the samples and accentuated by separations between the microfibrils occurring frequently along the length of the fiber [11]. The size and frequency of the separations is less for the 10 MPa stressed sulfonated fibers than the other samples. In all cases, evidence of crosslinking between microfibrils can be observed within these separations. It can also be seen in all cases that the microfibrils of the sulfonated fibers are swollen compared to the precursor fiber due to the uptake of sulfur. These microfibrils then remain swollen after carbonization.

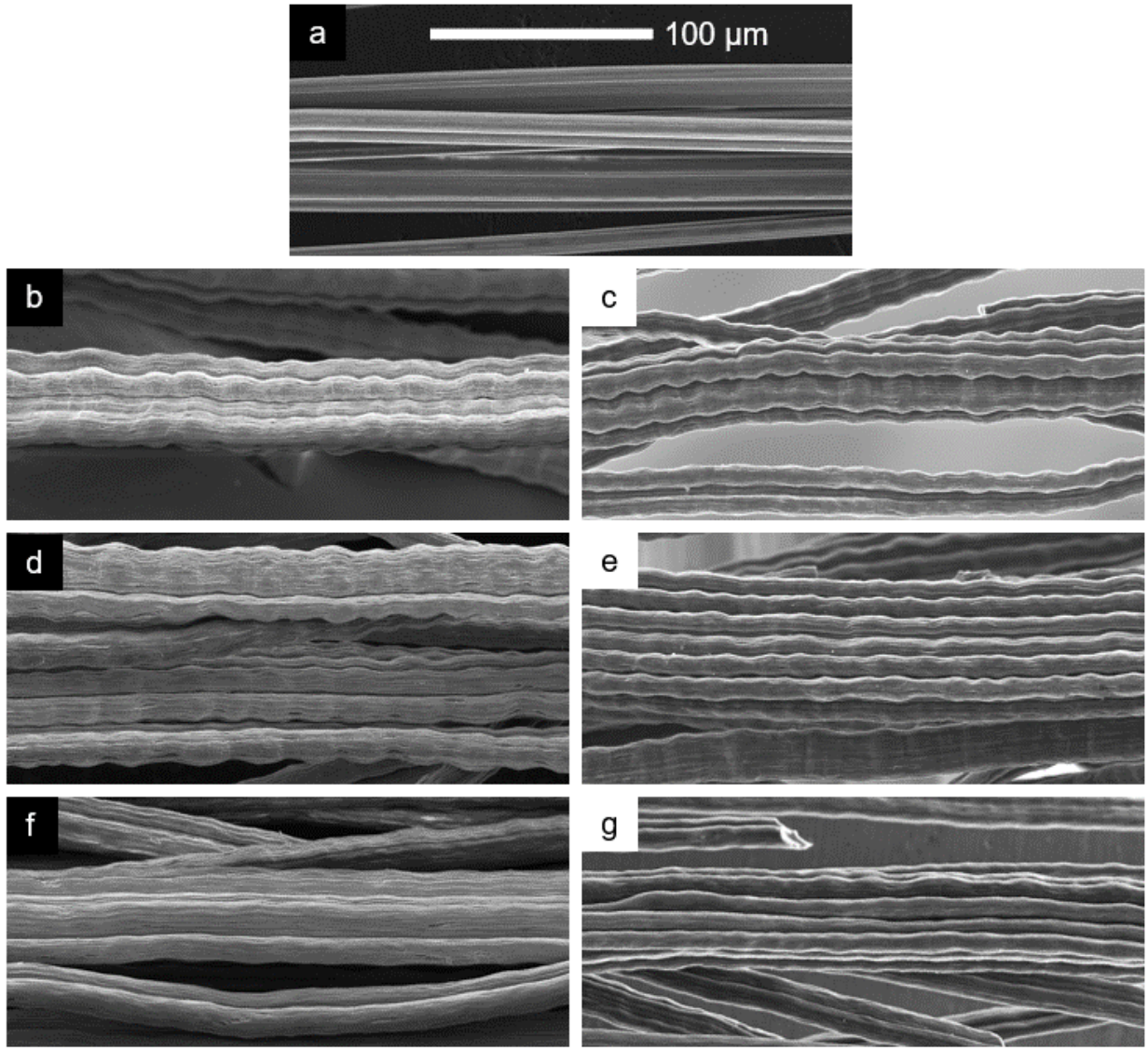

Figure 16. *a) SEM images of the UHMWPE precursor, SEM of stabilized fibers sulfonated with b) 0.1 MPa, d) 1 MPa, and f) 10 MPa tensile stress, and SEM of the carbonized fibers that had been sulfonated with (c) 0.1 MPa, (e) 1.0 MPa, and (g) 10 MPa tensile stress. The scalebar shown applies to subfigures.*

3.3. Microstructural Evolution

Raman spectroscopy and X-ray diffraction (XRD) were used to probe the microstructural evolution of the fibers after each step of the conversion process. The Raman spectra of each sulfonated and carbonized sample is shown in Figure 17. Despite the clear relationship between increasing tension and improving fiber morphology, no such relationship was evident in the Raman spectra; The spectra for all three sulfonated fiber samples were nearly identical, Figure 17a, as

were the Raman spectra of the three carbonized fiber samples, Figure 17b. Peak deconvolution was employed to understand the relevant microstructural features of the fibers at each stage of conversion. The Raman spectra for the sulfonated fibers feature the characteristic peaks of the aromatic ring breathing mode (near 1400 cm^{-1}) and carbon double bond stretching mode (near 1600 cm^{-1}) commonly reported in literature, which indicate the development of polyaromatic structures and crosslinking [148]. A third, minor peak may be present near 1150 cm^{-1}, which is hypothesized to be associated with stretching modes of remaining sulfonic acid functional groups in the resulting polyaromatic structure [149]. This may explain the long tail on the ring-breathing mode peak present in the Raman spectra shown in Figure 17 and many other Raman spectra of sulfonation-stabilized PE, see [115,148,150,151]. The presence of sulfonic acid groups is a result of the abstraction of hydrogen atoms from the polymer chain by the sulfuric acid and subsequent addition of sulfonic groups onto the polymer chain. This peak is relatively small because these sulfonic acid groups are cyclically eliminated above 120°C thereby crosslinking adjacent polymer chains [108,115].

A four-peak fit was applied to a representative spectrum for the carbon fibers derived from 10 MPa tension-sulfonated UHMWPE. The fit peaks are a mixture of Lorentzian and Gaussian curves consistent with the work of Vautard et al. [152], and the peaks are assigned according to the nomenclature set forth by Brubaker et al. [153] wherein the peaks at 1180 cm^{-1}, 1350 cm^{-1}, 1519 cm^{-1}, and 1603 cm^{-1} are assigned as the D4, D1, D3, and G peaks respectively. The D1 and G peaks are well established in the study of carbonaceous materials. The G peak arises from the presence of sp^2 carbon bonds and the D1 peak is associated with disorder or defects in the graphitic lattice [154,155]. The D3 peak indicates the presence of amorphous carbon content [156,157], and the D4 peak is associated with the presence of aliphatic moieties in the lattice [157,158], referred

to as the C-H peak by Vautard et al [152]. The conspicuous absence of a D2, or D', peak is explained by the high disorder present in the fibers as indicated by the D1 peak [153,159]. The magnitude of the D1, D3, and D4 peaks suggests that these carbon fibers are highly amorphous with a high rate of lattice disorder.

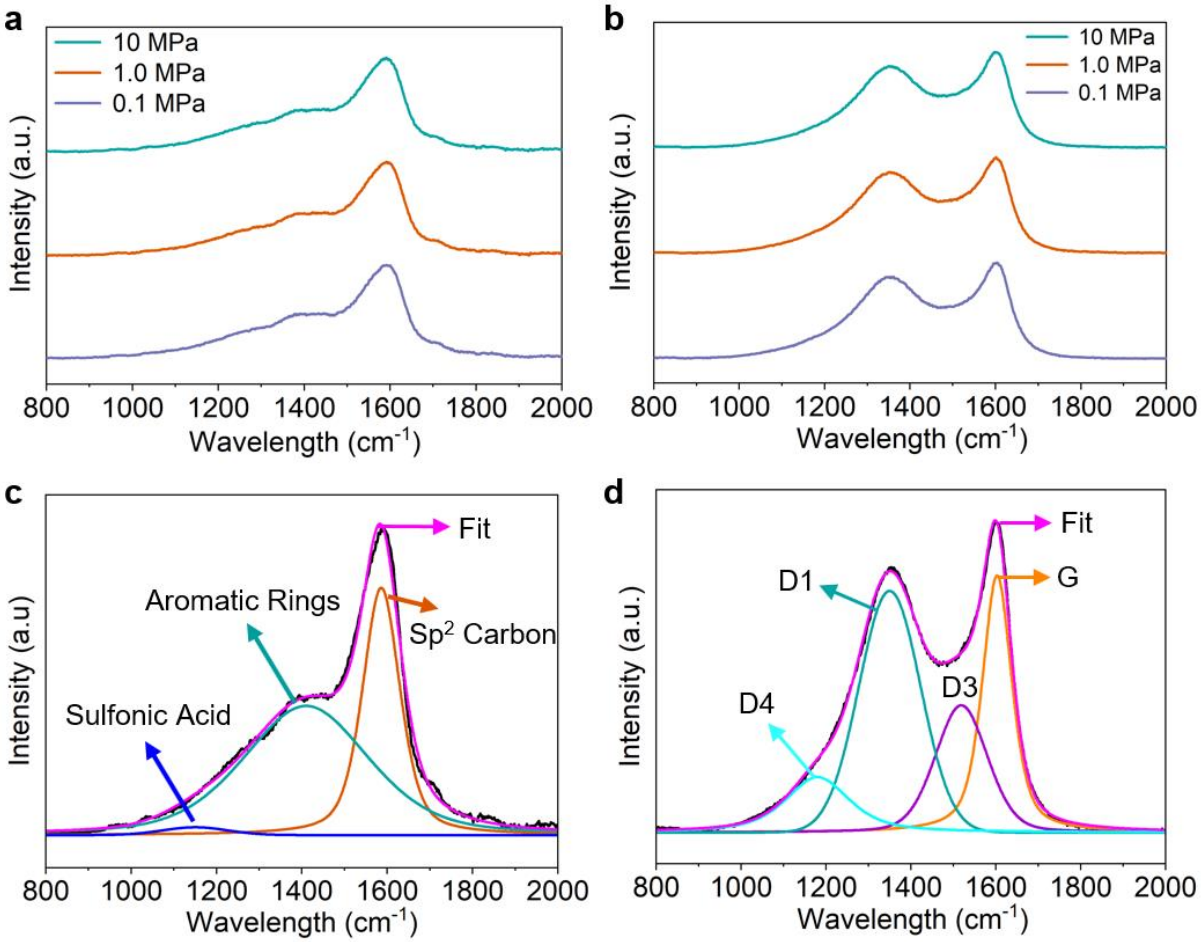

Figure 17. *Raman spectra of a) sulfonated fibers at each applied tension level, and b) carbon fibers made from sulfonated fibers at each applied tension level. Peak deconvolution was used to identify the relevant microstructural features of a representative c) Raman spectra of a sulfonated fiber with 10 MPa applied tension and d) carbon fiber derived from a fiber sulfonated with 10 MPa applied tension*

XRD was used to observe the microstructural evolution from precursor fibers to carbon fibers and to examine the properties of the turbostratic carbon crystallites present in the carbon fibers. These properties include interplanar spacing (d_{002}), crystallite dimensions (L_c and $L_{a\parallel}$), and the degree of orientation of the crystallites as shown by the half width at half maximum (HWHM) of

the (002) peak intensity across an azimuthal scan (Z_{002}) and corresponding Herman's orientation factor (f_{002}). These dimensions are schematically represented in Figure 18a,b, with a representative 1D XRD line integration shown in Figure 18c.

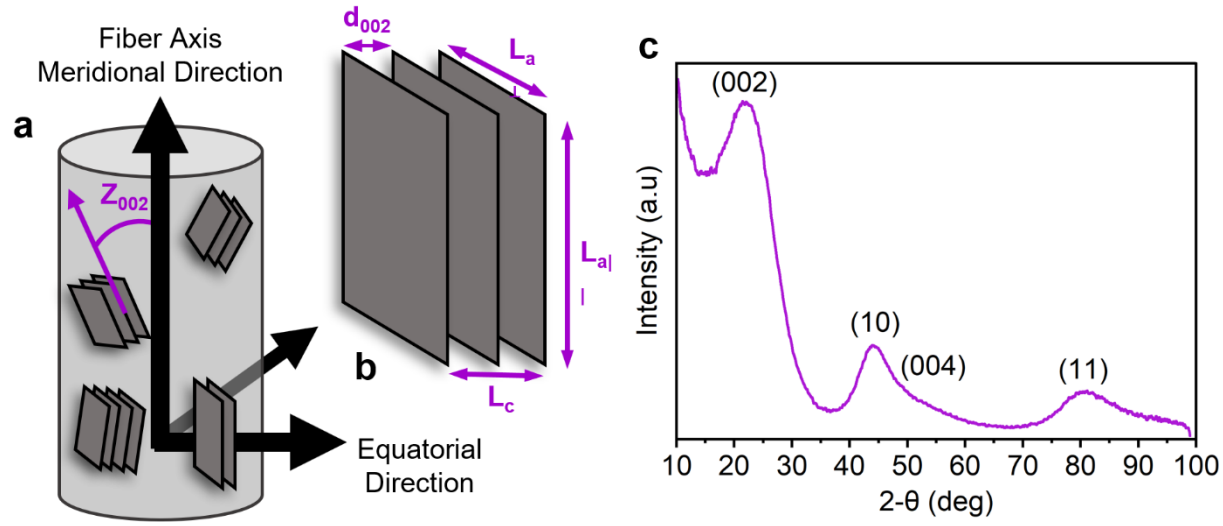

Figure 18. *a) Schematic of a carbon fiber featuring the coordinate system used to describe the X-ray diffraction directions and planar stacks exemplifying the diversity of crystallite dimensions and orientations that may be present in the fiber. b) A schematic definition of the crystallite dimensions measured via XRD in this work. c) XRD line integration in the fiber equatorial direction of carbon fibers derived from UHMWPE sulfonation-stabilized under 10 MPa tensile stress*

The carbon fiber samples exhibit significant scattering at low 2θ angles, Figure 19a,b, which is indicative of a significant presence of amorphous content and single-layer crystallites [146]. Nonetheless, no background subtraction was performed prior to quantitative analysis of the carbon fiber scattering patterns in the interest of a true comparison. Bragg's law was used to calculate the interplanar spacing, d_{002}, as shown in equation 2.1,

$$n\lambda = 2d_{002}\sin(\theta_{002}) \tag{2.1}$$

where λ is the wavelength of the incident X-rays, n is the diffraction order, and θ_{002} is the (002) peak position.

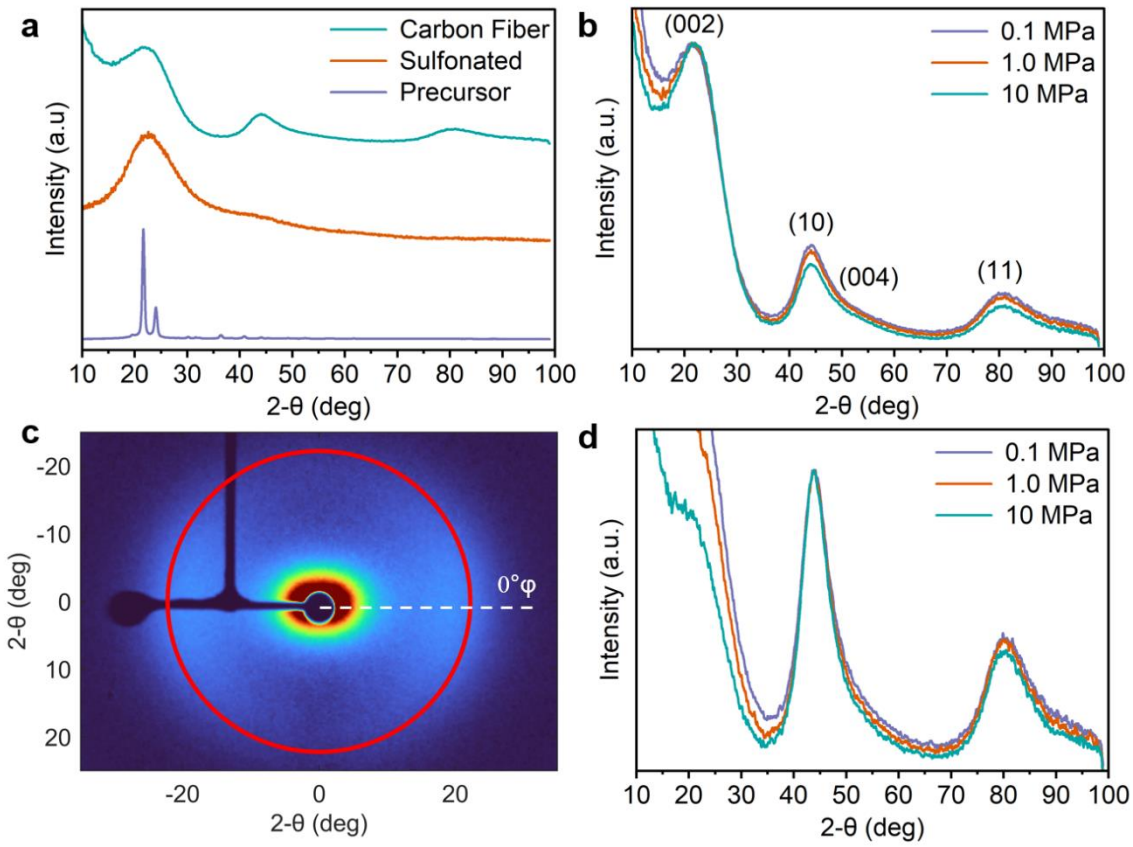

Figure 19. *XRD line integrations relative to the fiber equatorial direction for a) precursor, sulfonated, and carbon fibers, b) XRD line integrations relative to the fiber equatorial direction and normalized to the (002) peak for carbon fibers derived from UHMWPE sulfonated under 0.1 MPa, 1.0 MPa, and 10 MPa, c) 2D XRD scan of carbon fiber derived from UHMWPE sulfonation stabilized under 10 MPa tensile stress showing the azimuthal intensity distribution scan centerline in red and position of 0° φ. d) XRD line integrations relative to the fiber meridional direction and normalized to the (10) peak for carbon fibers derived from UHMWPE sulfonated under 0.1 MPa, 1.0 MPa, and 10 MPa*

The crystallite dimensions were calculated using the Scherrer equation, as shown in equation 2.2.

$$L_c = \frac{k\lambda}{FWHM_{002}\cos(\theta_{002})}, L_{a\parallel} = \frac{k\lambda}{FWHM_{10}\cos(\theta_{10})} \quad (2.2)$$

L_c is the dimension perpendicular to the graphite planes, often referred to as the stacking height, and $L_{a\parallel}$ is the dimension along the graphite plane parallel to the fiber axis, Figure 18. $FWHM_{002}$ is the full width at half maximum of the (002) peak from a line integration in the fiber equatorial direction, and $FWHM_{10}$ is the full width at half maximum of the (10) peak from a line integration in the fiber meridional direction. Peak-fitting methodologies were found to be very inaccurate for

analysis of the (002) and (10) peaks [145,146,160]. Therefore, a simple ruler technique was applied to find the FWHM of the (002) and (10) peaks [161]. For very small crystallites, strong deviations from quoted values of the shape factor, k = 0.89 (002) and k = 1.84 (10), have been seen. Given this information, k was assumed to be unity for the (002) and (10) peaks. The average orientation of the graphite crystallites relative to the fiber axis can be expressed as the HWHM of the azimuthal intensity distribution at the (002) position, Z_{002}, and is also commonly represented by the orientation parameter, $\langle \cos^2(\phi) \rangle$, equation 2.3, and Herman's orientation factor, f_{002}, equation 2.4, [48,162]. This azimuthal intensity distribution can be seen in Figure 19c.

$$\langle \cos^2(\phi) \rangle = \frac{\int_0^{\pi/2} I(\phi) \cos^2(\phi) \sin(\phi) d\phi}{\int_0^{\pi/2} I(\phi) \sin(\phi) d\phi} \tag{2.3}$$

$$f_{002} = \frac{1}{2}(3\langle \cos^2(\phi) \rangle - 1) \tag{2.4}$$

The crystallite dimensions, L_c and $L_{a\parallel}$, both increased with increasing sulfonation tension. The crystallite dimensions and orientation relative to the fiber axis increased significantly with increasing sulfonation tension while crystallite interplanar spacing remained constant, Figure 20. The crystallite orientation is low relative to commercial PAN and pitch-derived carbon fibers [163], but it has been noted that this orientation can be significantly improved with increasing carbonization temperatures [118,164]. Furthermore, the crystallite dimensions are consistent with the results achieved by Barton et al. [118] carbonizing LLDPE at the same temperature applied in this study (1000 ℃). In their work, these dimensions increased significantly at higher temperatures with boron catalyzation. Mechanical force is commonly applied during processing of PAN-based carbon fibers and is well-known to help align the polymer chains during thermal treatments. This effect is evident here with the increasing of crystallite dimensions and increased orientation with increasing applied tension [165].

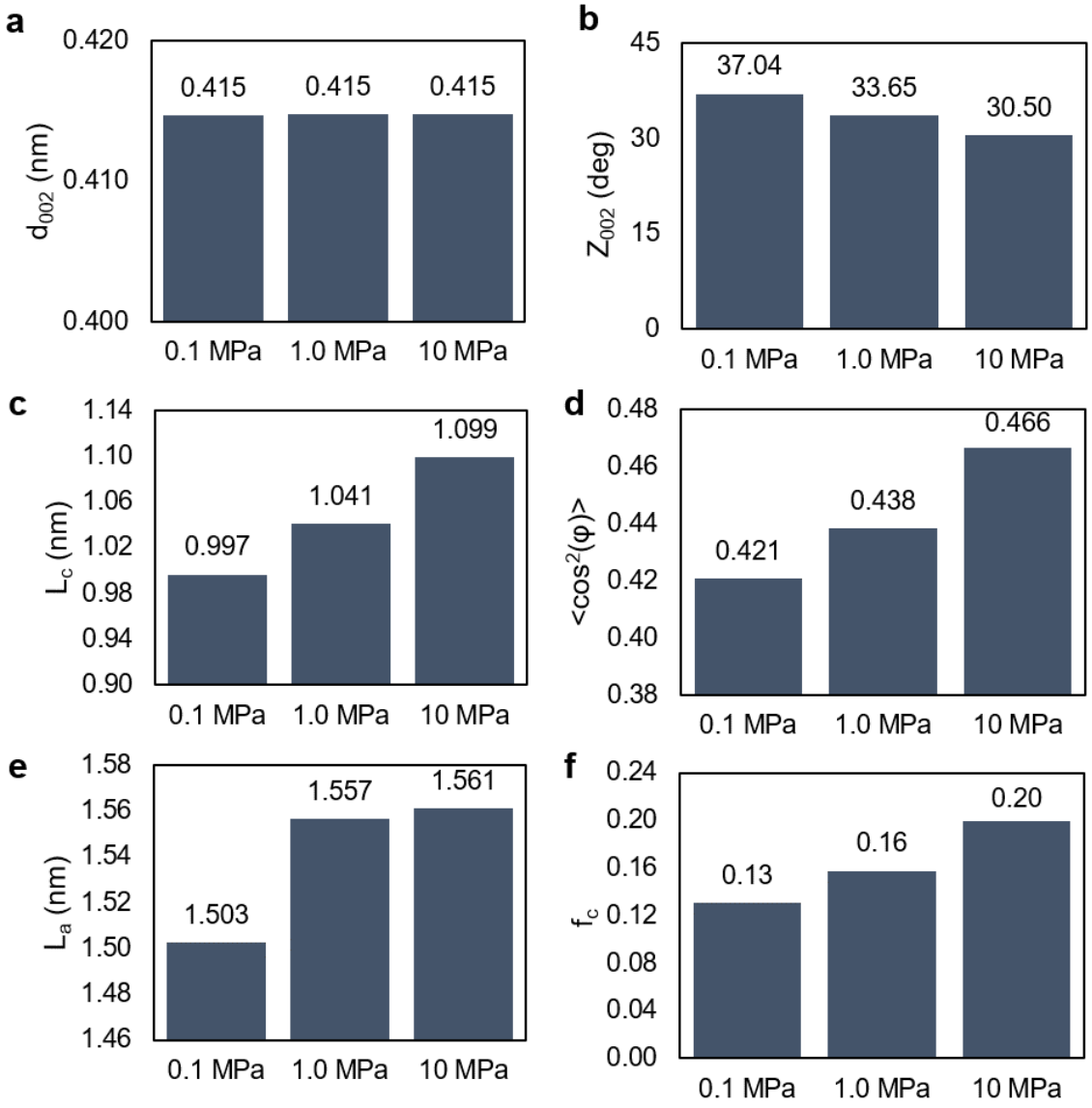

Figure 20. *Comparison of crystallite dimensions, a) d_{002}, c) L_c, and e) $L_{a\parallel}$, and orientation relative to the fiber axis as represented by b) Z_{002}, d) $<\cos^2(\varphi)>$, and f) Herman's orientation factor, f_{002}*

3.4. Carbon Fiber Mechanical Properties

Single-filament tensile testing showed a significant improvement in carbon fiber mechanical properties with increasing sulfonation tension. The fibers sulfonated with 0.1 MPa tensile stress were too fragile to be tensile tested, and the average mechanical properties of the carbon fibers derived from fibers sulfonated with 1.0 MPa and 10 MPa tensile stress are shown in Table 2.

***Table 2**. Mechanical properties and their respective coefficient of variance (COV) of carbon fibers derived from UHMWPE fibers sulfonated under different amounts of tensile stress. The carbon fibers from UHMWPE sulfonated under 0.1 MPa tensile stress could not be tested*

	Average Strength		**Average Modulus**		**Average Strain**	
Sulfonation Tension	(MPa)	COV (%)	(GPa)	COV (%)	(%)	COV (%)
1.0 MPa	115.25	50	37.84	45	0.36	26
10 MPa	257.35	47	52.26	22	0.53	29

Increasing tension from 1.0 MPa to 10 MPa resulted in a 123.3% increase in average tensile strength, 38.1% increase in average tensile modulus, and 47.2% increase in average strain to failure. The greatest mechanical properties were measured to be 469.5 MPa tensile strength, 62.8 GPa tensile modulus, and strain at failure of 0.76% from a carbon fiber derived from UHMWPE sulfonated under 10 MPa tensile stress. All the samples exhibited high variance in the measured properties, but the variance declined significantly with increasing tension. In many cases, two or more adjacent fibers fused together during sulfonation resulting in complex cross-sectional geometries with internal voids and cracks at the intersections of the original fibers, Figure 21.

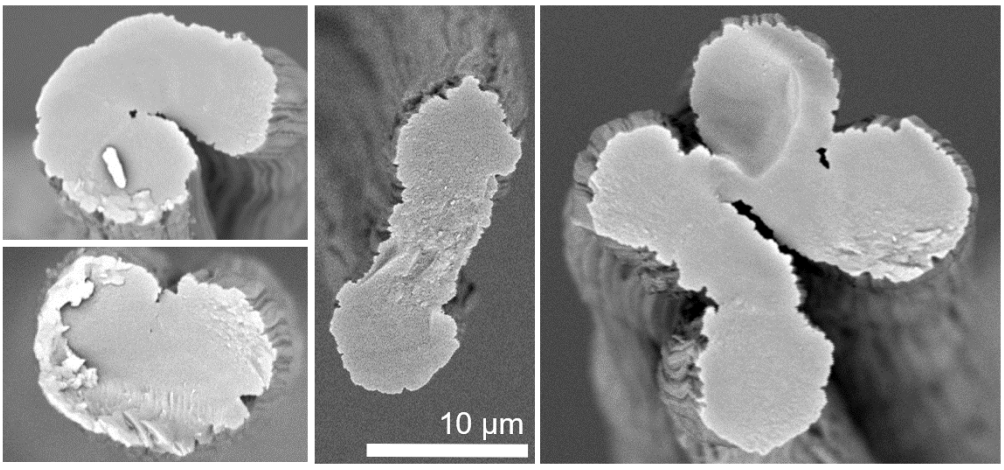

***Figure 21.** SEM images of tensile fracture surfaces from carbon fibers derived from UHMWPE sulfonated under 10 MPa tensile stress exemplifying the variety of cross-sectional shapes and sizes present in the sample. Scale bar applies to all images in this figure*

Furthermore, the axial striations in the fiber surface resulting from the precursor microfibrils, combined with the kink banding induced during sulfonation, results in surface defects that range from tens of nanometers to greater than one micrometer in depth. Much like earlier carbon fibers, these fibers are strength-limited due to these large surface flaws [106,166]. The fracture surfaces of the fibers largely lack the granular texture common of high-modulus carbon fibers [167], which reinforces the Raman and XRD results indicating a highly amorphous microstructure.

Although faint mist and hackle region textures emanate from the fracture critical flaw in some of the tensile sample fracture surfaces, Figure 22, most of the fracture surfaces lack a clear indication of the crack initiation point and the brittle fracture features, Figure 21, that would be used to calculate the fracture toughness of these fibers [168]. However, the potential strength of these fibers can be estimated for different critical flaw sizes using the Griffith-Irwin relation,

$$\sigma_f = \sqrt{\frac{EG}{\pi a}} \tag{2.5}$$

where σ_f is the tensile strength at fracture, E is the measured modulus, a is the critical flaw size, and G is the total fracture energy, which is the sum of the surface energy, γ, and energy dissipation due to plastic deformation, G, as shown in equation 2.6,

$$G = 2\gamma + G_p \tag{2.6}$$

The surface energy of the carbon fibers (γ_{CF}) can be estimated via equation 2.7,

$$2\gamma_{CF} = 2\gamma_G \frac{\rho_{CF}}{\rho_G} \langle \cos(\phi) \rangle \tag{2.7}$$

where γ_G is the thermodynamic surface energy for a lateral surface of a graphite crystal (4.8 J/m^2 [169]), ρ_{CF} is the density of the sample carbon fibers, ρ_G is the density of a graphite crystal (2.265 x 10^3 kg/m^3 [170]), and $\langle \cos(\phi) \rangle$ is the average cosine of the crystallite orientation, ϕ,

which was determined via XRD. The density of the carbon fibers is assumed to be 1.8 x 10^3 kg/m^3 [41,168].

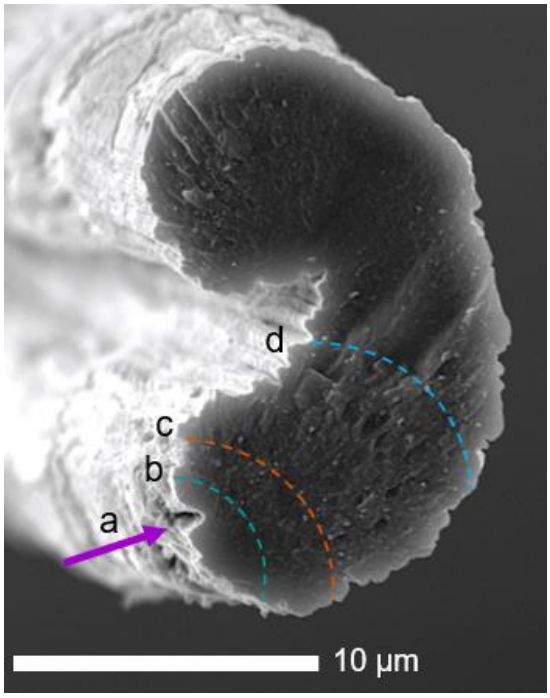

Figure 22. *SEM image of carbon fiber tensile fracture surface (10 MPa sulfonated) with an a) 641 nm critical flaw and featuring brittle fracture features highlighted by their respective fronts: b) mirror region, c) mist region, and d) hackle region*

Although the fracture surfaces from the single fiber tensile tests indicate some amount of plastic deformation during fracture, the plastic deformation energy dissipation was neglected to establish a lower bound of the predicted ultimate tensile strength. This Griffith-Irwin relation was applied across critical flaw lengths ranging from 10 nm to 1 µm to estimate the potential ultimate strength of the fibers developed in this work. This range spans the large flaws observed in the test specimens, for example Figure 23a, down to the small flaws found in modern commercial carbon fibers, which are commonly less than 50 nm [171]. This analysis shows that the carbon fibers derived from UHMWPE sulfonation stabilized under 10 MPa tensile stress could achieve an ultimate tensile strength of 3.31 GPa with a critical flaw size of 10 nm. Furthermore, it demonstrates that the benefits of increased tension are amplified with decreasing flaw size; the

carbon fibers derived from UHMWPE sulfonation stabilized under 1.0 MPa tensile stress would achieve a significantly lower tensile strength at failure of 2.77 GPa at the same critical flaw size. The predicted strength at a critical flaw size of 1 μm also correlates well with the observed failure tensile strengths, which confirms the presence of 1 μm and greater critical flaws in the fibers.

A critical first step to improving the magnitude and consistency of the mechanical properties is preventing the fusion of adjacent fibers during the stabilization process, which may be achieved during a continuous tow sulfonation stabilization process by employing tow spreaders to separate the filaments. Next, the large voids induced by microfibril splitting and contraction must be reduced in size and frequency. Finite element analysis was employed to simulate the stress concentration of a conical surface flaw in the fiber as a proxy to the flaw shown in Figure 23a. The relative stress increase across the fiber diameter approaching the flaw is shown in Figure 23c,d and demonstrates the significance of such stress concentrations. Finally, the conversion methods and parameters must be optimized for greater graphitic structure growth to achieve high tensile modulus in tandem with high tensile strength. This has been accomplished for LLDPE by increasing the carbonization temperature and the use of boron as a crosslinking catalyst, which resulted in significantly improved mechanical properties [118].

Although the tensile properties of the UHMWPE-derived carbon fibers produced in this study are not competitive with commercial-grade, PAN-derived carbon fibers, they are competitive with the tensile properties of activated carbon fibers [172]. It is estimated that several 10,000s of tons of UHMWPE fiber are produced annually [173], and the limited ability to melt-process it makes conventional recycling nearly impossible. The results of this work present an opportunity to upcycle this waste into activated carbon fibers, which have garnered increasing attention in the past several years thanks to their wide spanning applications from air and water purification to

supercapacitors [174]. The axially striated macro and micro texture of these carbon fibers may offer the high surface area that is characteristic of highly effective activated carbon fibers. Future studies on the surface area and adsorption capacity of these carbon fibers will unveil their potential as activated carbon fibers.

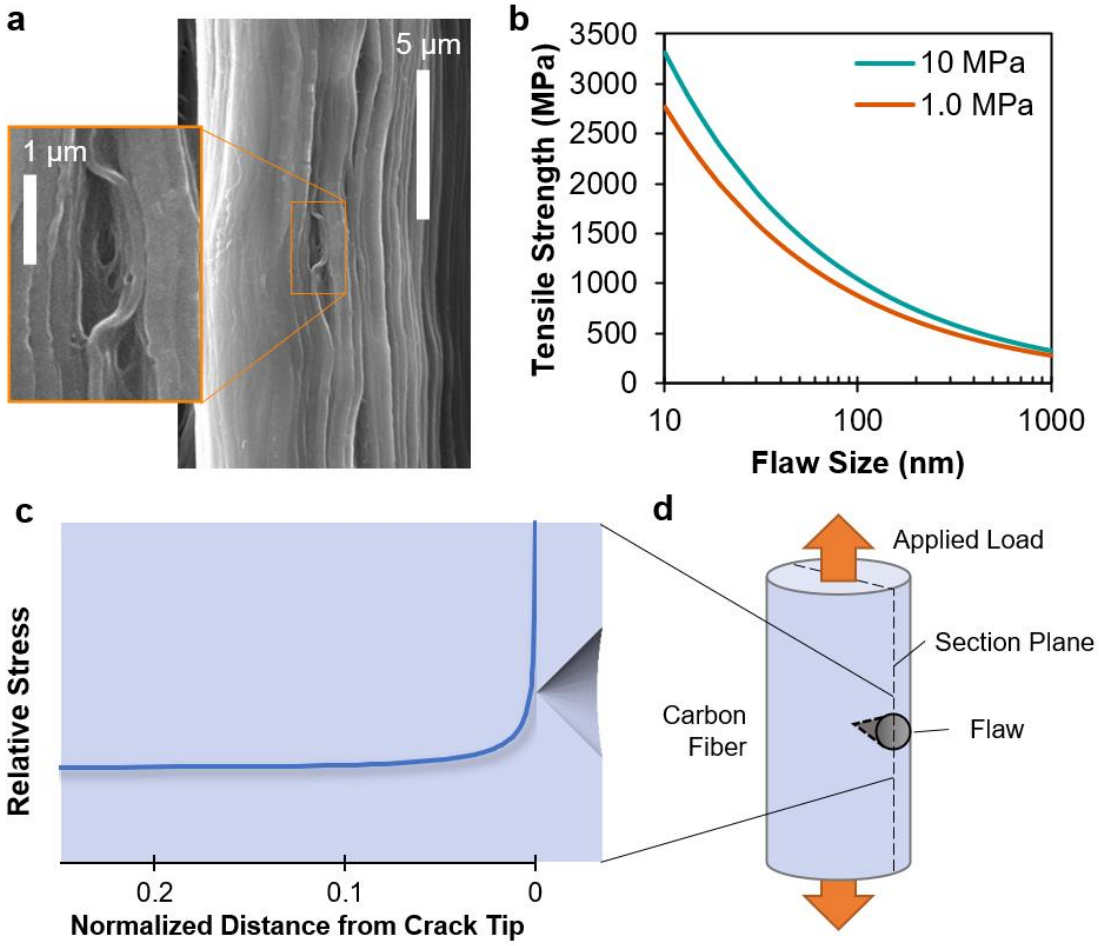

Figure 23. *a) SEM of a carbon fiber derived from UHMWPE sulfonation-stabilized under 10 MPa tensile stress with magnified view of large fiber defect, b) predicted fiber tensile strength relative to critical flaw size per Griffith-Irwin relation, c) normalized stress across fiber diameter approaching conical flaw as determined via finite element analysis and with CAD geometry underlaid for reference, d) schematic of tensile finite element analysis setup of fiber with conical flaw*

4. Conclusion

In this work, carbon fibers were produced from commercially available UHMWPE fibers sulfonation-stabilized under various tensile loads to examine its effect on the fibers' morphology,

microstructural evolution, and mechanical properties. Increasing the tension applied during sulfonation significantly reduced the amplitude and frequency of kink bands in the sulfonated and carbonized fibers and reduced the amount and rate of axial shrinkage of the fibers. Increasing sulfonation tension did not affect the Raman response of the fibers, but Raman spectroscopy revealed that the fibers were highly amorphous with a significant amount of lattice disorder. XRD corroborated this finding by exhibiting a large response of single layer and amorphous content in all the carbon fiber samples. XRD also showed that the crystallite dimensions and orientation relative to the fiber axis increased significantly when tension was increased from 0.1 MPa to 10 MPa. The improvements in morphology and crystallite properties culminated in increased mechanical performance for the resulting carbon fibers. Carbon fibers produced with a sulfonation tensile stress of 0.1 MPa were too fragile for tensile testing, whereas carbon fibers from a sulfonation tensile stress of 10 MPa exhibited a maximum tensile strength of 469.5 MPa, modulus of 62.8 GPa, and strain at failure of 0.76%. This work shows that maximizing tension applied during the sulfonation of UHMWPE fibers can significantly improve the morphology, microstructure, and properties of the resulting carbon fibers. Increasing the performance of carbon fibers derived from these UHMWPE precursors may be achieved by preventing the fusion of adjacent fibers during stabilization to reduce the occurrence of surface and internal flaws, further reducing the occurrence of surface flaws induced by microfibril separation and contraction and increasing the crystallite orientation and size of the fibers. If the critical flaw size can be reduced to the scale of those found in modern commercial carbon fibers (10 nm or less), these fibers may exhibit tensile strengths up to 3.31 GPa based on the Griffith-Irwin relation. Graphitizing the fibers may then result in high modulus and high strength fibers, but it must be acknowledged that a remaining challenge will be the high cost of UHMWPE precursor fibers compared to PAN and

lower molecular weight polyethylene. However, the high surface area exhibited by the fibers' surface morphology may make these fibers highly effective activated carbon fibers. Converting end-of-life UHMWPE fibers into activated carbon fibers could reduce tens of thousands of tons of plastic waste from landfills thereby extending the lifecycle of UHMWPE and purifying our water and air at the same time.

Chapter 3. UHMWPE Micro-Ribbon Fibers Gel Spun Using Orange Terpenes

1. Introduction

Although initial studies of orange terpenes as an alternative spin-solvent for UHMWPE gel spinning showed promise, a fuller picture of the microstructure and mechanical properties of these fibers is needed to assess its true potential. This work aims to fill this gap in the understanding of the physical, microstructural, and tensile properties of UHMWPE fibers spun using orange terpenes as the solvent. UHMWPE fibers were spun using orange terpenes and hot drawn at a ratio of 5:1. The as-spun and drawn fibers' morphology were then evaluated via optical and scanning electron microscopy, thermal properties and crystallinity via differential scanning calorimetry, crystallite properties via X-ray diffraction, and tensile properties via single filament tensile testing.

2. Experimental Methods

2.1. Lab-Scale Gel Spinning System

A custom gel spinning line was designed using Solidworks computer aided design (CAD) software featuring a Harvard Apparatus PhD 2000 syringe pump mounted vertically on a custom frame with a vertically translating sled so that the extruder could be positioned over top of a coagulation bath with adjustable height to control the air quench length. Custom positionable Teflon rollers were designed and fabricated to guide the extrudate through the coagulation bath, and a custom takeup winder was designed and fabricated to collect the spun fibers. Several nozzles were fabricated from stainless steel o-ring boss plugs featuring orifice diameters ranging from 1100 μm down to 200 μm. The ratio of the orifice diameter to orifice channel length was set at 2:1 for all nozzles. A CAD rendering of the assembly and cross-sectional view of a nozzle is shown in Figure 24.

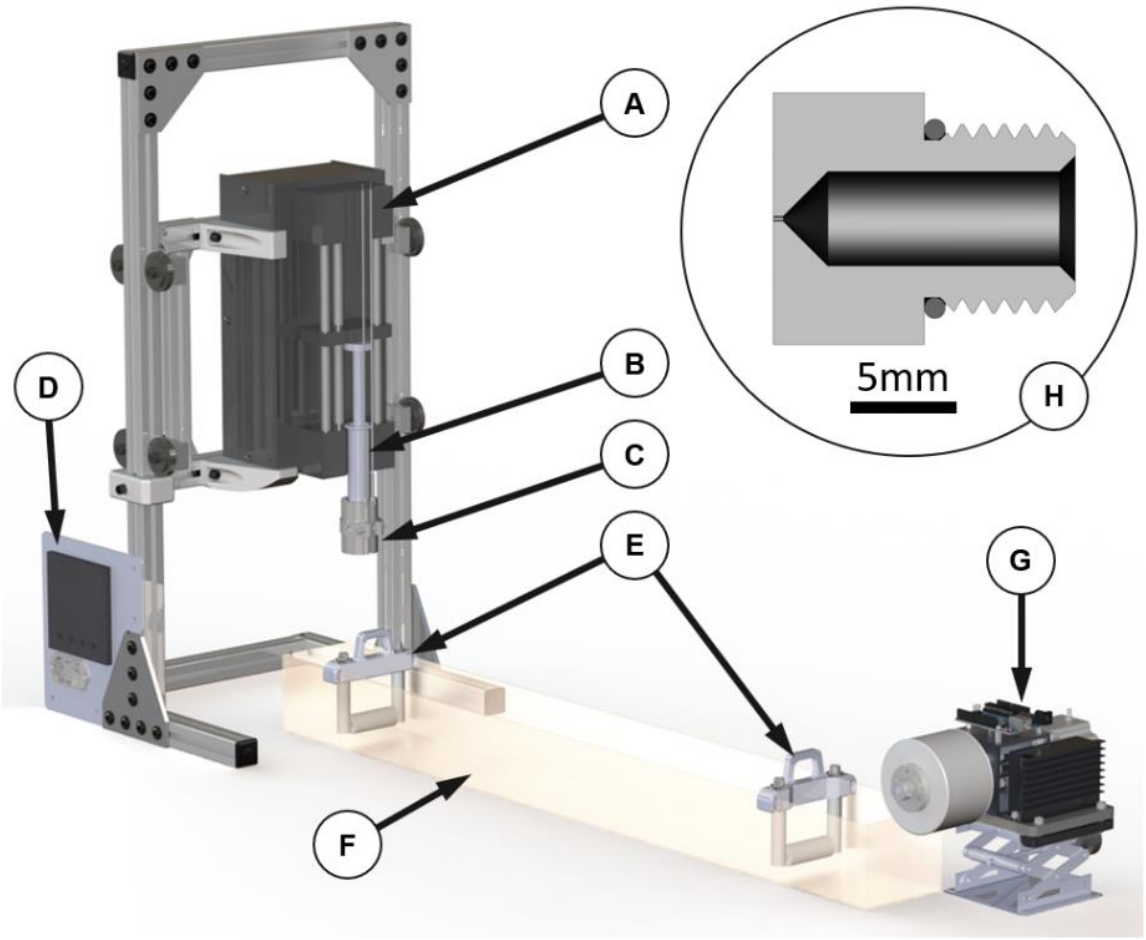

Figure 24*. CAD rendering of the custom gel spinning line including a) syringe pump on vertical sled for height adjustment, b) stainless steel syringe, c) band heater controlled by d) a Tempco temperature controller, e) positionable guide rollers for fiber transfer through the coagulation bath, f) a stainless steel tank for the coagulation bath, g) Arduino-controlled, stepper motor-driven takeup winder mounted on a lab jack for 4-degrees of positional freedom, and h) a custom stainless steel nozzle turned from an o-ring boss plug. The nozzle features a 250 μm diameter orifice and 500 μm channel length*

2.2. Materials

UHMWPE powder with an average molecular weight of 3M-6M g/mol was used as the feedstock, and food-grade orange terpenes were used as the solvent. 2,6-Di-tert-butyl-4-methylphenol was used as an antioxidant. All materials were purchased from Sigma-Aldrich and used without further purification. Orange terpenes is a conglomeration of terpenes and sesquiterpenes extracted from orange peels and is composed of 90-95% limonene, a terpene bio-solvent commonly used in industrial processes and cleaning products [175,176]. Dyneema SK60

UHMWPE fibers were characterized as delivered from the manufacturer in select methods to provide context for the properties of commercially produced UHMWPE fibers.

2.3. Sample Preparation

2.3.1. Dissolution of UHMWPE in Orange Terpenes

The UHMWPE-orange terpenes solution was formed by preheating a solution of orange terpenes and 2,6-di-tert-butyl-4-methylphenol above the melting temperature of UHMWPE then adding the polymer to the heated solution under stirring. The UHMWPE concentration was 3 wt% of the total solution and the antioxidant concentration was 0.15 wt% of the total solution. The polymer concentration was selected based on preliminary spinning trials through which it was found that consistent and continuous spinning could be achieved at 3 wt% UHMWPE. This concentration is consistent with previously published results and commercial production processes [91]. In preliminary trials, it was found that this antioxidant concentration prevented yellowing of the solution during heating in the extruder barrel, which indicates sufficient prevention of oxidation. The mixture was heated and stirred until the UHMWPE completely dissolved.

2.3.2. Fiber Spinning

Upon formation, the polymer solution was immediately transferred to the barrel of the extruder, which was preheated to 130°C, and allowed to equilibrate in the barrel for five minutes. Following equilibration, the syringe piston was inserted, and the air in the syringe was evacuated. The spinning nozzle was installed, and the solution was allowed to equilibrate once again for five minutes before beginning extrusion. The nozzle orifice is round with a nominal diameter of 250 μm and length of approximately 500 μm. The barrel temperature was set to 130°C for extrusion, and the syringe pump was set to extrude at a rate of 0.07 mL/min. The extruded filament descended a 10 cm air gap into a deionized water coagulation bath at ambient temperature. The fiber was

immersed in this bath for approximately 68 cm before being taken up onto a spool at a rate of 2.5 m/min. The collected fibers were retained on the spool while the solvent remaining in the fibers evaporated in ambient air for no less than 12 hours. Thermogravimetric analysis (TGA) was used to verify that the orange terpenes, boiling point 178°C, was completely extracted. A 7.5 mg sample of the as-spun fibers was heated to 190°C at 10°C/min followed by a 30 minute hold in a pierced-lid aluminum pan with no measurable weight loss.

2.3.3. Fiber Drawing

The fibers were drawn by transferring the fiber from a driven payout spool, across the surface of a heated, polished aluminum plate and onto a takeup spool. The fiber draw ratio is defined as the ratio of the takeup speed to the payout speed. The hot plate surface temperature was set to 130°C, and the draw ratio was set to 5:1 for consistency with previous works using orange terpenes as the spin solvent [89].

2.4. Characterization Methods

2.4.1. Morphological Analysis

The shape and surface of the fibers were observed via optical microscopy and scanning electron microscopy (SEM). Optical microscopy was conducted using a Hirox RH-8800 digital microscope (700x – 1000x magnification), and SEM was conducted using an FEI Quanta 650. All samples were sputter coated with gold using a Cressington sputter coater to prevent charging during SEM.

2.4.2. Thermal Properties

A Netzsch STA 449 F1 Jupiter Simultaneous Thermal Analyzer was used to conduct TGA and differential scanning calorimetry (DSC) of the samples. At least 5 mg of the fibers per sample were cut into short strands, pressed into an aluminum crucible, and sealed with a cold weld crimped lid to ensure contact between the sample and the crucible bottom. A two-cycle heating routine was

applied to observe the effect of spinning and drawing then observe the behavior of the material after the thermal history is erased. The samples were heated to 180°C and cooled twice with a directed heating and cooling rate of 10°C/min.

2.4.3. Microstructural Analysis

The orientation, crystallite sizes, and overall crystallinity of the fibers were acquired via wide angle X-ray scattering (WAXS) on a Bruker D8 Venture in Debye-Scherrer configuration (fiber axis orthogonal to beam and detector). The fibers were illuminated with monochromated (Helios™ monochromator, multilayer optics) Cu-Kα radiation (λ=0.154184 nm) and diffraction patterns were collected with a Photon III 2D detector. Orientation of the fibers was determined by analysis of the azimuthal intensity along the (110) orthorhombic peak using Herman's orientation factor (HOF), as shown in Equations 3.1 and 3.2 [177].

$$HOF = \frac{3\langle \cos^2\varphi \rangle - 1}{2} \tag{3.1}$$

$$\langle \cos^2\varphi \rangle = \frac{\int_0^{\pi/2} I(\varphi)\cos^2\varphi \sin\varphi d\varphi}{\int_0^{\pi/2} I(\varphi)\sin\varphi d\varphi} \tag{3.2}$$

To obtain 1D patterns, the 2D frames were integrated over a 90° azimuthal region for determination of the crystallite sizes and overall crystallinity. The crystallite sizes, L_{hkl}, and d-spacings, d_{hkl}, of the orthorhombic phase, (110) and (200), were determined by applying the Scherrer equation [178], Equation 3.3, and Bragg's Law [179], Equation 3.4, respectively. In both equations, λ is the angle of the incident X-rays, and θ_{hkl} is the relevant 2θ peak position. In Equation 3.3, K is a shape factor assumed to be unity when it is not well-defined [180], and β_{hkl} is the full width at half maximum of the peak of interest. In Equation 3.4, n is the diffraction order. Peak fitting was done using LIPRAS software [181].

$$L_{hkl} = \frac{K\lambda}{\beta_{hkl} \cos \theta_{hkl}} \quad (3.3)$$

$$n\lambda = 2d_{hkl} \sin \theta_{hkl} \quad (3.4)$$

Crystallinity was determined by taking the ratio of the crystalline peak areas from 10-35° 2θ divided by the total area, which consists of amorphous and crystalline peak areas, A_a and A_c respectively, Equation 3.5.

$$\% \, crystallinity = \frac{A_c}{A_c + A_a} * 100 \quad (3.5)$$

2.4.4. Mechanical Properties

The linear density of the fibers was measured according to ASTM standard D1577 whereby single filaments were cut into 320 mm lengths and a bundle of these segments was weighed using a Mettler-Toledo XSE205DU analytical balance for each sample. The linear density was then used to evaluate the tensile properties of the fibers in accordance with ASTM standard D3822. An MTS Nano Bionix Universal Testing Machine with a maximum load capacity of 500 mN and 150 mm of extension was used to conduct single filament testing. A gauge length of 25 mm was selected for this study, and at least 15 successful tests, as defined by the applied ASTM standard, were recorded for each sample. The breaking tenacity (cN/dtex) is the fiber load at fracture divided by the linear density of the fibers. The initial modulus was obtained by calculating the slope of the initial linear region of the load-strain curve for each test.

3. Results and Discussion

3.1. Morphological Analysis

The fibers spun from UHMWPE-orange terpenes solution exhibited a flat, ribbon-like profile, as shown in Figure 25, with an average width of 94 μm and thickness of 11 μm yielding an average aspect ratio of 9.2:1.

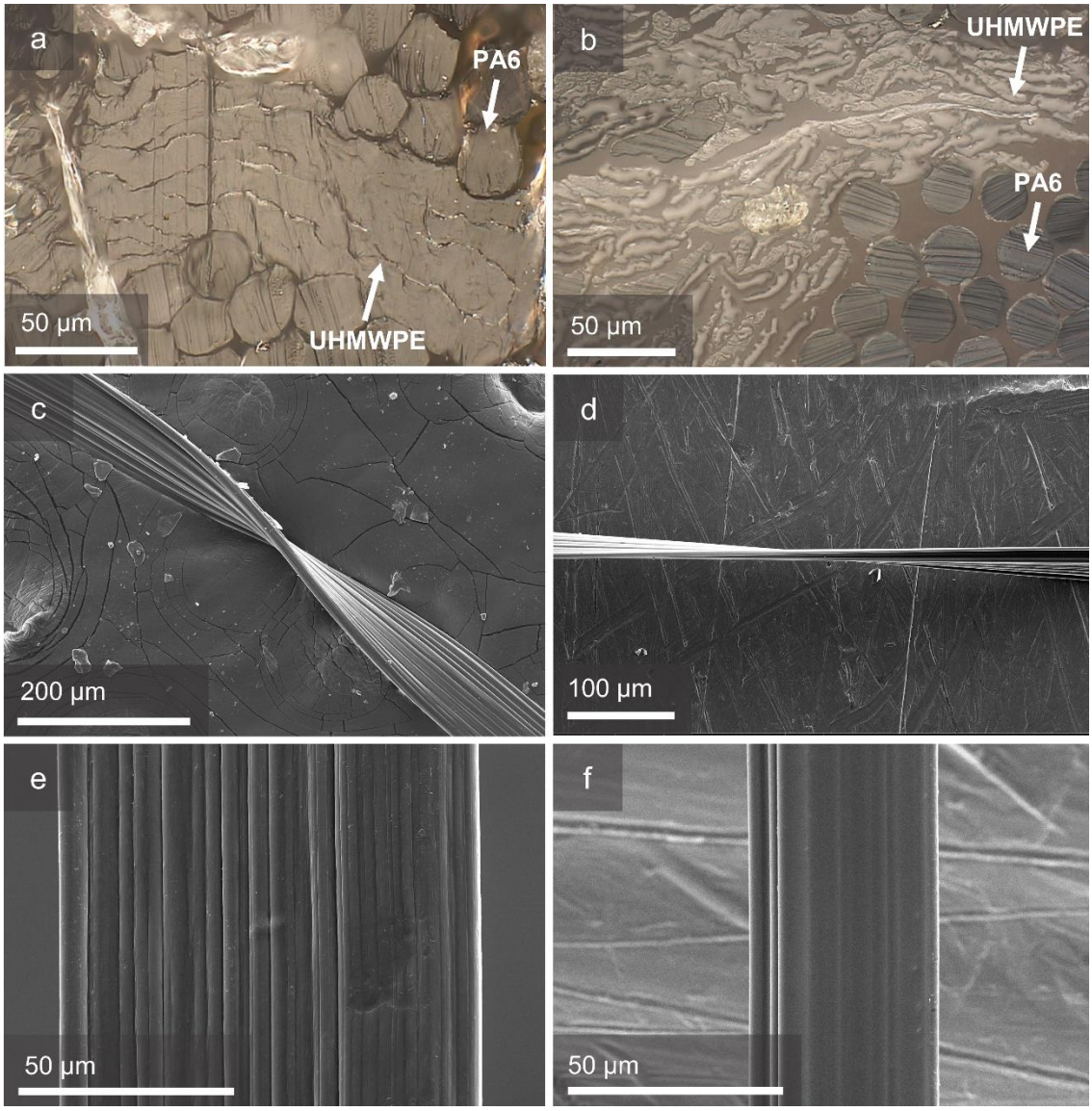

Figure 25. *Optical microscope cross-sectional image of a) as-spun and b) drawn UHMWPE fibers surrounded by round cross-section polyamide 6 (PA6) fibers with an average diameter 24 µm that were used as a mounting filler, and SEM images of twisted c) as-spun fiber and d) drawn fiber further demonstrating the flat shape of the fibers, and SEM side view of e) as-spun fiber and f) drawn fiber showing significant reduction in width*

The drawing process significantly reduced the size of the fibers yielding an average width of 41 µm and average thickness of 4 µm. The average aspect ratio of the fibers remained approximately the same after drawing at 9.5:1 indicating that the fibers reduced evenly in width and thickness. The axial fibrillar structure characteristic of UHMWPE fibers is strongly present in the as-spun fibers and slightly smoothed in the drawn fibers, Figure 25e,f. Some small defects

were observed on the fiber surfaces, which may be attributed to imperfections in the spinning and takeup hardware. This flat profile allows for strikingly compact stacking of the fibers as shown in Figure 25a,b where the wide profile conforms to fill gaps unlike the round profile of the adjacent polyamide-6 fibers. This effect may enable extremely high fiber volume fractions in composites reinforced with UHMWPE fibers. Hot flattening of commercially-produced round UHMWPE fibers was explored in 2016 to achieve this shape, but the physical deformation process resulted in damage to the crystalline structure of the fibers and reduced mechanical properties [182]. Achieving micro-ribbon UHMWPE fibers directly from spinning will remove this secondary step thereby potentially retaining high mechanical properties. It is hypothesized that the round profile of the fiber induced by the extrusion orifice deforms to flat after contact with the first roller of the coagulation bath. Although the UHMWPE-orange terpenes solution gels rapidly after exiting the extrusion die due to cooling in the ambient air, the solvent concentration remains high when the fiber encounters the first roller in the spin line. The line tension from the take-up winder deforms the gel fiber against this roller into a flat shape, and the subsequent quenching and partial solvent extraction in the coagulation bath initiate solidification in this form. This may be indicative of incomplete gelation at the fiber's first interaction with the spin line roller, at which point the polymer molecules have not formed sufficient crosslinks to prevent this deformation. Considering the similarity between decalin and orange terpenes as volatile solvents, this hypothesis is supported by the gelation/crystallization mechanisms put forth by Shi *et al*. [183] wherein gelation occurs slowly and crystallization occurs later relative to paraffin oil-UHMWPE solutions. Understanding the gelation and crystallization behavior of UHMWPE-orange terpenes is crucial to understanding the formation of this morphology and the progression of lamellar crystal formation, and so it should be a high priority for future studies of this method.

3.2. Thermal Properties

The melting onset, melting peak, recrystallization peak, and remelting peak temperatures were measured via DSC, Table 3. The peak melting temperature, T_{m1}, of the as-spun and drawn fibers were consistent with UHMWPE fibers spun from conventional solvents [11]. Consistent with published literature, fiber drawing increased the melting temperature of the fibers due to increased molecular order [16]. This effect is accentuated by the significantly higher melting temperature of Dyneema SK60 fibers (150°C [184]), which benefit from much greater drawing. Each sample was cooled and remelted to erase the thermal history induced by the fiber spinning and drawing processes. The heat flow, and consequently the recrystallization temperature, T_c, were identical for the first and second cooling cycles with respect to each sample, which confirms the erasure of thermal history during the first melting. In both the as-spun and drawn fiber samples, the melting temperature decreased by approximately 3°C upon remelting indicating that spinning and drawing were each responsible for inducing molecular order. The recrystallization temperature of the drawn fibers was 1.1°C higher than the as-spun fibers. Furthermore, the re-melting temperature, T_{m2}, of the drawn fibers was approximately the same as the initial melting temperature of the as-spun fibers. This indicates that the drawing process induced an irreversible change to the polymer microstructure, which was investigated in depth via DSC and WAXS.

Table 3. *Melting onset temperature (T_{m0}), melting peak temperature (T_{m1}), recrystallization temperature (T_c), and remelting peak temperature (T_{m2}) of the as-spun and drawn UHMWPE fibers spun using orange terpenes with commercially-produced Dyneema SK60 fibers included for comparison*

	T_{m0} (°C)	T_{m1} (°C)	T_c (°C)	T_{m2} (°C)
As-Spun	127.4	141.6	114.6	138.3
5:1 Drawn	130.1	144.4	115.7	141.1

3.3. Fiber Microstructure

3.3.1. Crystallinity

The microstructural changes indicated by the changes in melting, crystallization, and re-melting temperatures were probed analytically via DSC and WAXS. A quick and simple method of assessing polymer bulk crystallinity is commonly made via DSC by comparing the melting enthalpy of the sample (Δh_m) with the melting enthalpy of a perfectly crystalline representation of the material (Δh_u), which is assumed to be 293 J/g for polyethylene [185], Equation 3.6.

$$\chi_{dsc} = \frac{\Delta h_m}{\Delta h_u} \tag{3.6}$$

The melting enthalpy and crystallinity as recorded by the first and second melts of the fiber samples are shown in Table 4 with results from commercially produced Dyneema SK60 fibers included for reference.

Table 4. *Comparison of the melting enthalpy and calculated crystallinity of the sample fibers and Dyneema SK60 reference fibers after the first and second melting cycles*

	Initial Melt Cycle			**Re-Melt Cycle**		
	As-Spun	**Drawn**	**SK60**	**As-Spun**	**Drawn**	**SK60**
Melting Enthalpy (J/g)	125.8	111.0	215.4	90.1	102.3	120.8
Crystallinity	42.6%	37.9%	73.5%	30.8%	34.9%	41.2%

It is not surprising that the fibers spun from orange terpenes possess significantly lower crystallinity than their commercially-produced counterpart, Dyneema SK60, because the SK60 fibers undergo significantly more hot drawing [16]. However, the decline in crystallinity following drawing was unexpected. This result was confirmed via WAXS and is discussed in more detail below. Notably, the drawn fibers exhibited greater retention of crystallinity after recrystallization than the as-spun fibers. The crystallinity of the as-spun fibers decreased by nearly 12% after the first melt cycle whereas the drawn fibers' crystallinity only decreased by 3%. This reflects the

irreversible microstructural change indicated by the elevated re-melting temperature of the drawn fibers with respect to the as-spun fibers. This change is also evident in the shape of the melting endotherm of the drawn fibers, in which a secondary peak is evident near 155°C, Figure 26b.

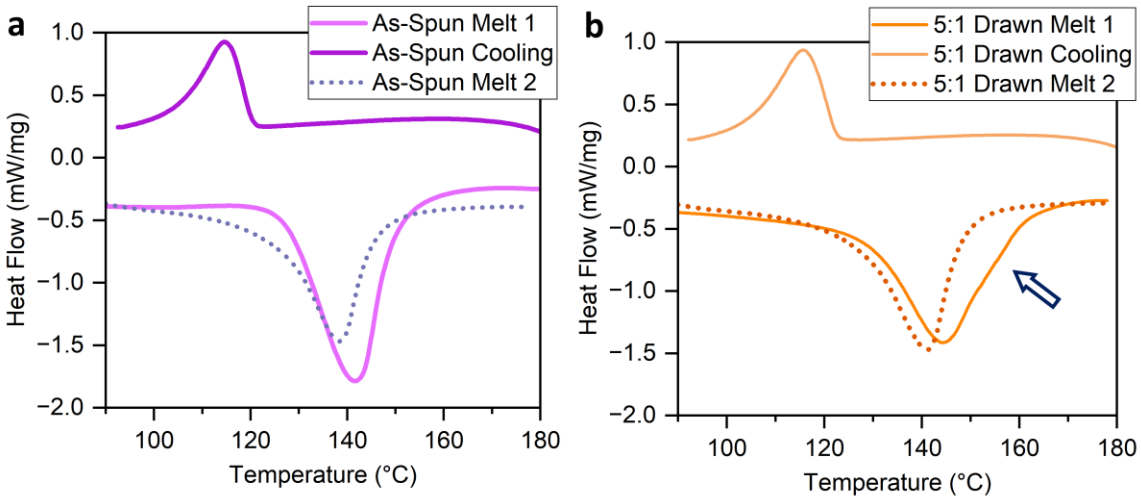

Figure 26. *DSC plots of a) as-spun and b) drawn UHMWPE fibers spun using orange terpenes with arrow indicating the melting endotherm deviation indicative of secondary melting peak related to solid-state phase transition of orthorhombic crystals to pseudo-hexagonal*

This secondary peak is ascribed to a solid-state phase transition from orthorhombic to a metastable pseudo-hexagonal structure during heating, which is induced by the close proximity of the polymer chains that results from the drawing process [131,186]. It has been shown that this secondary peak is a consequence of constrained melting of the fibers, such as being constrained by a crimped-lid DSC pan like those used in this study [23,187,188], which provides an additional insight into the microstructure of the fibers. The as-spun fibers in this study were prepared for DSC in the same way as the drawn fibers and exhibited no secondary peak. This may be the result of folded-chain crystals that inhibit the formation of this hexagonal phase. These folded-chain crystals are converted to extended-chain crystals during drawing [189], and these structures make this solid-state phase transition to pseudo-hexagonal. This transformation in the higher-order

crystal structure from folded-chain lamellae to extended chain crystals is also evident in the increased peak melting temperature and broadening of the melting endotherm [190,191].

WAXS results confirmed the decline in crystallinity induced by drawing observed via DSC; the crystallinity of the as-spun fibers was found to be 76.0% whereas the crystallinity of the drawn fibers was 60.8%. The relationship between the experimental fibers and Dyneema SK60 was also confirmed via WAXS; The crystallinity of the commercially-produced fibers was calculated to be 88.6%. It should be acknowledged that the WAXS-measured crystallinity is significantly higher than that measured via DSC. However, the results of each method are consistent with other works reporting the DSC-measured crystallinity of Dyneema SK60 [192] and WAXS-measured crystallinity of experimental UHMWPE fibers [16,88]. This underestimation via DSC has been reported before [190,193], and there are many factors, such as sample mass and heating rate, that can affect DSC results [187,188,194]. This is why it is crucial to investigate crystallinity via several techniques to provide a more complete picture [187,195].

Typically, UHMWPE fiber drawing increases crystallinity, which is ascribed to strain-induced crystallization as amorphous chains align and compact transversely [16]. The reduction in crystallinity from the as-spun fibers to the drawn fibers is likely the result of the drawing temperature, 130°C, exceeding the melting onset temperature of the as-spun fibers, 127.4°C. It is hypothesized that some of the fiber crystals, perhaps imperfect or small crystals, melt at this drawing temperature [187,196], and the dislocation and reorientation of these molecules during drawing inhibits the reformation of these crystals after cooling [23]. This partially molten state also results in reduced deep entanglement and thus lower applied stress leading to less stress-induced crystallization [197]. This effect has been shown in commercially-produced UHMWPE fibers undergoing drawing at similar proximity to the melting temperature; the fibers reduced from

92% to 83% crystallinity after drawing at 131.5°C [198]. A similar reduction in crystallinity was observed in UHMWPE films formed at 160-180°C then drawn at a ratio of 12:1 at 150°C. However, increasing the draw ratio beyond 20:1 ultimately resulted in increased crystallinity [199,200]. It has been shown that UHMWPE fibers can be drawn at approximately 35:1 with a drawing temperature of 135°C [201], so deeper drawing of the UHMWPE fibers spun from orange terpenes and drawn at 130°C may be possible thereby increasing crystallinity.

3.3.2. Crystallite Size and Orientation

Beyond bulk crystallinity, WAXS revealed information about the nature of the crystallites in the fiber. The primary orthorhombic peaks, (110) and (200) located at 21.2° and 23.6° 2θ, are strongly present in the fibers while the monoclinic peak, (010) located at 19.6° 2θ, is largely masked by the amorphous response at low 2θ, Figure 27a. This amorphous response is visibly greater in the drawn fibers compared to the as-spun fibers. Peak deconvolution was employed to determine the peaks' full width at half maximum (FWHM) and area, which were then used to determine the concentration of each crystalline phase and the crystallites' lateral size and d-spacing. Orthorhombic crystallites accounted for 94.5% of the crystalline content of the as-spun fibers and the remainder was monoclinic crystallites. After drawing, the orthorhombic crystallites decreased to 89.2% of the crystallinity of the fibers, and the monoclinic content increased to 10.8%. This increase in monoclinic phase content is consistent with other hot-drawn UHMWPE fibers that exhibited reduced crystallinity [198]. The nature of the orthorhombic crystallites is of particular interest because they are the primary contributor to the mechanical properties of UHMWPE [16]. Notably, the crystallite size perpendicular to the (110) plane of the orthorhombic phase increased slightly from 13.1 nm to 13.4 nm after drawing, while the crystallite size perpendicular to the (200) reflection decreased from 12.3 nm to 11.6 nm. The lateral size of these

crystallites and d-spacing are consistent with those of commercially spun UHMWPE fibers [202]. The (200), (110), and (010) reflections are interpreted to be the dimensions of crystalline microfibrils perpendicular to the fiber axis and have been shown to increase with increasing draw ratio [203,204]. This is well exemplified by the significantly larger dimensions exhibited by Dyneema SK60 fibers, Table 5. The limited growth and even decrease in these dimensions in the experimental fibers correlates with the crystallite melting and destruction indicated via DSC and WAXS. However, the anisotropic change in crystallite dimensions of the fibers produced for this study is unique. It is unclear if this is an artifact of the large reorientation of the crystal structures from the as-spun to drawn states moving the crystals into or out of Bragg condition [205], an aspect of the anisotropic fiber morphology, or a consequence drawing parameters. Further study via small angle X-ray scattering (SAXS) and nuclear magnetic resonance spectroscopy (NMR) will provide insight into crystalline dimensions inaccessible via WAXS, which may resolve this open question. In all crystallites, the d-spacing was effectively unchanged by drawing as was the size of the monoclinic crystallites (4.7 nm). The crystallite size and d-spacing for each crystallographic plane is shown in Table 5.

Table 5. *Crystallite sizes (L_{hkl}), d-spacing (d_{hkl}), and Herman's orientation factor (HOF) for as-spun and drawn fibers produced in this study as well as commercially-produced Dyneema SK60 fibers for context*

	L_{010} (nm)	**L_{110} (nm)**	**L_{200} (nm)**	**d_{010} (nm)**	**d_{110} (nm)**	**d_{200} (nm)**	**HOF**
As-Spun	4.73	13.12	12.31	0.45	0.42	0.38	0.55
5:1 Drawn	4.73	13.42	11.62	0.46	0.42	0.38	0.88
SK60	5.33	15.77	12.98	0.46	0.41	0.37	0.86

As expected for fiber drawing, the crystallite orientation significantly increased with drawing, which is crucial to the development of high mechanical properties [16,192]. The Herman's orientation factor increased by 60% from 0.55 for the as-spun fibers to 0.88 for the drawn fibers.

The degree of orientation of the drawn fibers is consistent with fibers spun from other alternative solvents and drawn, such as polybutene [22]. The orientation of the drawn fibers created in this study are approximately that of Dyneema SK60, Table 5, which is unsurprising considering the high rate of increase of alignment induced at low draw ratios that then plateaus at greater draw ratios [16]. This increase in orientation is dramatically apparent in the clarification of the 2θ peaks from circular bands in the as-spun fibers to nearly points in the drawn fibers as shown in the 2D WAXS plot, Figure 27b,c.

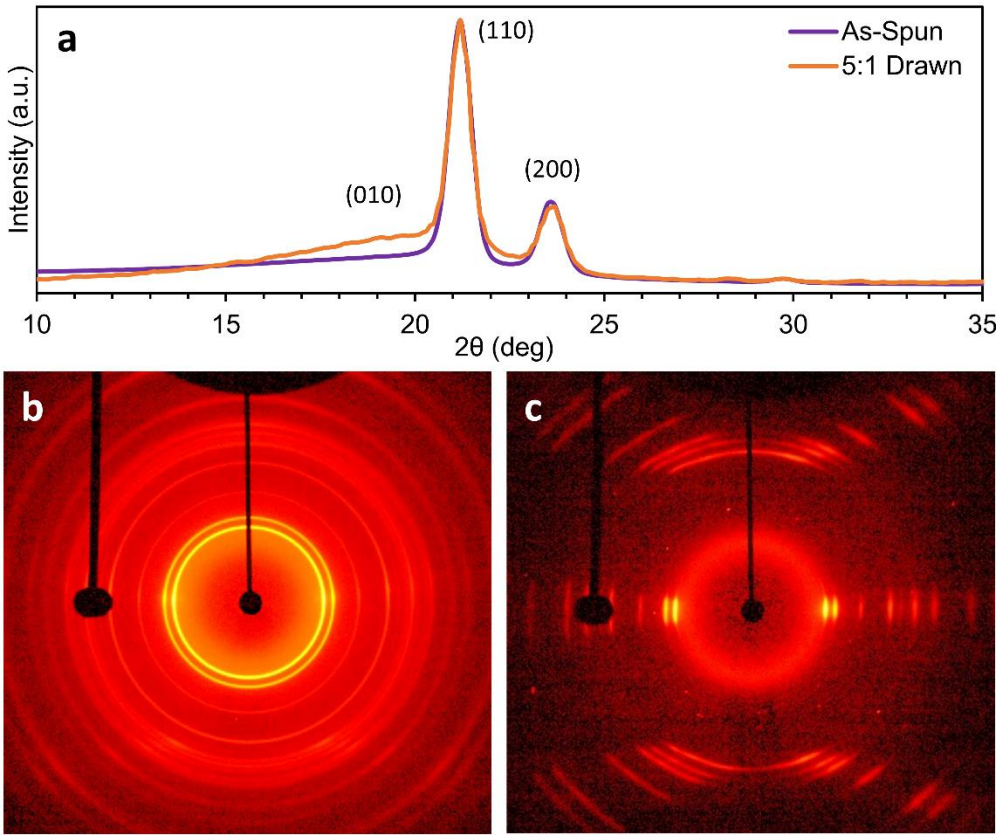

Figure 27. *a) 1D WAXS pattern for as-spun and drawn fibers showing the positions of the orthorhombic peak, (110) and (200), and 2D WAXS plots for the b) as-spun and c) drawn fibers*

3.4. Tensile Properties

The linear density of the as-spun and drawn fibers was determined to be 12.0 dtex and 1.6 dtex respectively, which aligns with the change in cross-section size observed via SEM. The drawing

process resulted in significant increases in breaking tenacity (+511%) and modulus (+986%), as well as a corresponding decline in strain at break (-1736%), Table 6. The coefficient of variation (COV) of each property sharply declined after drawing, which indicates that the drawing process significantly reduced variability in the fiber micro- and macro-structure. This is visibly evident in the smoother surface of the drawn fibers via SEM in Figure 25, and may also be the result of the drawing process resolving internal defects trapped during the crystallization of the gel fiber after extrusion [204].

Table 6. *Summary of mean mechanical properties ± standard error with corresponding COV of the as-spun and drawn samples from a minimum of fifteen valid single-filament tensile tests*

	Initial Modulus		**Breaking Tenacity**		**Strain at Break**	
	cN/dtex	COV (%)	cN/dtex	COV (%)	%	COV (%)
As-Spun	21.1 ± 1.2	22.3	1.41 ± 0.04	10.6	202 ± 21	40
Drawn	229.2 ± 2.4	4.3	8.62 ± 0.06	3.0	11 ± 0.52	18.7

The mechanical properties of the as-spun fibers are comparable to the highest properties previously published for UHMWPE fibers spun using orange terpenes, and the tenacity of the drawn fibers in this work is 4x greater [89]. Although these fibers fall short of the mechanical properties offered by UHMWPE fibers produced industrially using conventional solvents, their properties closely follow a trend of exponentially increasing mechanical properties with decreasing strain-to-failure, Figure 28. The fibers produced in this study possess a significantly higher strain to failure compared to Dyneema SK60 fibers, which is a result of the significantly higher non-crystalline content enabling greater deformation before internal stresses rise to the point of crystal shear and failure [192,206]. Failure occurs at lower tenacity due to the significantly lower crystalline content reducing the bulk load carrying capacity. This inverse relationship is well exemplified in Smith and Lemstra's [20] early UHMWPE drawing experiments with samples

ranging from as-spun fibers to a draw ratio of 31.7:1. The fibers produced in the present study perform similarly to the Smith and Lemstra [20] fibers at similar draw levels, which approach the tenacity of Dyneema SK60 at the highest draw ratio, Figure 28. Other works demonstrating alternative solvents, such as polybutene (Fang et al. [22]), or pre-swelling using decalin and olive oil (Wang et al. [88]), have also achieved properties akin to Dyneema SK60 with total draw ratios of 120:1 and 40:1 respectively, Figure 28. Therefore, orange terpenes-spun UHMWPE fibers demonstrate strong potential for development into high-performance fibers competitive with those currently on the market if the extended chain crystalline content and molecular alignment can be further improved.

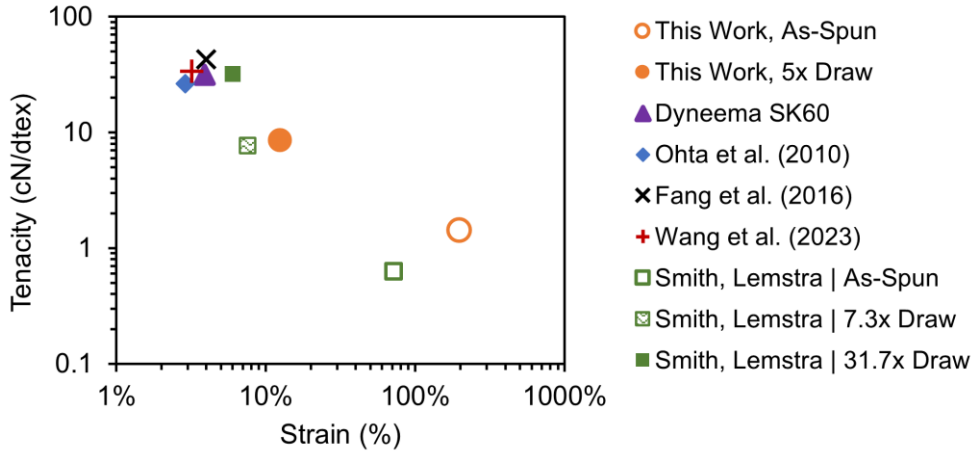

Figure 28. *Comparison of tenacity and strain-at-failure of fibers produced in this study with commercially produced Dyneema SK60 fibers and selected results published in literature*

Parametric optimization of the fiber drawing process is a logical first step to improving the mechanical properties based on the results of this work. The decrease in fiber crystallinity due to the drawing temperature exceeding the melting onset temperature of the as-spun fibers should be rectified first by tuning the drawing temperature to promote crystallite growth rather than degradation. It is well understood that increasing draw ratio significantly increases mechanical properties [16], and with an optimized drawing temperature the upper limit of drawability can be

explored. While it has been shown that draw ratio can be increased with increasing drawing temperature, up to 40:1 at 143°C [201], the optimum temperature is strain rate sensitive and can be much lower [196]. Furthermore, the exceptional mechanical properties of commercially-produced UHMWPE fibers are achieved by applying multiple drawing stages to achieve high crystallinity and molecular alignment [139]. The increase in melting temperature after drawing can be leveraged to increase the drawing temperature thereby increasing draw ratio for subsequent drawing stages. For example, Xu et al. [189] found that crystallite orientation increased to nearly perfect alignment with a HOF of 0.99 following a two-stage hot drawing with an initial drawing temperature of 120°C and second-stage drawing temperature of 130°C using industrial hot drawing equipment. Processing aids, such as supercritical carbon dioxide, can be employed to improve the drawing process as well [207].

Further optimization can be achieved by investigating the characteristics of UHMWPE-orange terpenes gelation and the spinning process parameters. It has been shown that the gelation and crystallization mechanisms vary significantly between the two leading solvents for UHMWPE gel spinning, decalin and paraffin, resulting in significantly different maximum draw ratios [183]. Rheological analysis, light scattering, and SAXS in addition to the methods used in this work will elucidate these mechanisms for UHMWPE-orange terpenes. The draw-down of the gel fiber after extrusion prior to solvent removal also affects the solid-state drawability of the fibers by inducing molecular disentanglement. It was found that an optimal draw-down ratio exists for UHMWPE-decalin gel fibers to maximize solid-fiber mechanical properties [208,209], and the same relationship should be explored for UHMWPE-orange terpenes. Furthermore, the strain rate applied during gel spinning using decalin affects the crystallization kinetics and crystalline structure of the as-spun fiber, which vary as a function of the relationship between the strain rate

and polymer solution relaxation time, referred to as Wi. Increasing Wi increased crystallization kinetics and induced the formation of straight chain crystals as opposed to isotropic lamellae. Crystalline structure development during post-spin drawing was affected by the strain-rate induced crystal structure as a function of draw ratio, and it was found that longer straight chain crystals formed during drawing of fibers spun at low Wi [210]. The effect of these microstructural relationships on the drawability and consequent mechanical properties of the fibers was left an open question, but the potential for optimization is apparent nonetheless. While crystallite dimensions and bulk crystallinity were explored in the present work, the higher-order crystalline structure of the as-spun and drawn fibers, such as the shish-kebab and microfibril structures that can be captured via NMR, SAXS, atomic force microscopy, will be a crucial element of conducting any of these investigations [203,204,211].

4. Conclusion

Orange terpenes were successfully used as a solvent for UHMWPE fiber gel spinning, and the resulting fibers were hot-drawn to reduce the size of the fibers and improve molecular alignment. The morphological, thermal, microstructural, and mechanical properties of the as-spun and drawn fibers were analyzed. The fibers exhibited a flat, micro-ribbon profile and the drawing process resulted in a significant reduction in fiber dimensions and linear density without affecting the aspect ratio of the fibers, which was measured to be 9.2:1 as-spun and 9.5:1 after drawing.

The thermal characteristics of the fibers are consistent with other UHMWPE fibers, and the drawing process increased the melting and crystallization temperatures by 2.8°C and 1.1°C respectively. Each sample was heated twice to unveil the effect of the spinning and drawing processes by erasing thermal history in the samples. The re-melting temperature of the drawn fibers remained higher than that of the as-spun fibers indicating that a permanent microstructural change,

potentially the formation of extended chain crystals from folded-chain crystals, was induced during drawing.

The microstructure of the fibers was assessed analytically via DSC and WAXS. The crystallinity of the fibers decreased due to the hot drawing temperature exceeding the melting onset temperature, but the crystallite alignment increased by 60% to a HOF of 0.88. The orthorhombic crystalline phase dominated the crystalline composition in as-spun and drawn forms, but the monoclinic phase content increased from 5.5% to 10.8% after drawing. Despite the reduction in crystallinity and increase in monoclinic crystallites, the increased molecular order resulted in a 511% increase in fiber breaking tenacity and 986% increase in tensile modulus. The drawn fibers in this study are 4x stronger than the strongest UHMWPE fibers previously spun using orange terpenes. Further studies optimizing the drawing of these UHMWPE fibers may lead to further significant increases in mechanical properties by increasing fiber crystallinity and orientation. This work demonstrates great potential for orange terpenes as a sustainable replacement for decalin-based commercial UHMWPE fiber production.

Chapter 4. 1,4-Cineole: A Bio-Derived Solvent for Highly Stable Graphene Suspensions and Well-Dispersed UHMWPE/Graphene Nanocomposite Fibers

1. Introduction

In this work, the field of bio-derived solvents was surveyed for opportunities to replace the harmful petrochemical solvents currently used for dry-extraction gel spinning of UHMWPE fibers with one that is suitable for the dissolution of UHMWPE and dispersion of graphene nanoplatelets (GnPs) simultaneously for the formation of UHMWPE/graphene nanocomposite fibers via gel spinning. One candidate, 1,4-cineole, was selected based on suitability predicted by Hansen solubility parameters and was evaluated for other properties relevant to nanoparticle dispersion, viscosity and surface tension. The dispersion stability of GnPs in this solvent was observed, and the dissolution of UHMWPE in this solvent was confirmed. UHMWPE fibers were spun with and without GnPs, hot stretched to a fine diameter, and characterized for their mechanical, microstructural, and thermal properties to demonstrate nanocomposite fiber formation via gel spinning. These characterizations enabled a greater understanding of the mechanisms governing the interactions between the GnPs and highly crystalline polymers.

2. Experimental Methods

2.1. Solvent Selection

The ideal solvent to produce UHMWPE/GnP nanocomposite fibers must be capable of dissolving UHMWPE into a semi-dilute solution and maintaining a stable dispersion of GnPs to prevent agglomeration. Hansen solubility parameters can be used to predict the solubility of both graphene and UHMWPE in a candidate solvent and was chosen as the first selection criteria. Per this method [212], a material can be ascribed three parameters, dispersion energy (δ_d), polar-dipolar energy (δ_p), and hydrogen bonding energy (δ_h), which can be visualized as the axes of a

three-dimensional Hansen space. A solute has a prescribed interaction radius, R_0, and if a solvent's position in Hansen space falls within this interaction radius, then it is predicted to be a "good" solvent for that solute. The HSP distance between the solvent and solute, R_a, is calculated via Equation 4.1:

$$R_a^2 = 4(\delta D_1 - \delta D_2)^2 + (\delta P_1 - \delta P_2)^2 + (\delta H_1 - \delta H_2)^2 \quad (4.1)$$

The solubility of a pairing can then be quickly assessed by calculating the relative energy difference (RED) of the two molecules via Equation 4.2, where a RED < 1 indicates "good" solubility:

$$RED = R_a/R_0 \quad (4.2)$$

The HSPs for UHMWPE [213] and graphene [68] are included at the top of Table 7 followed by the two leading commercial solvents for UHMWPE gel spinning, decalin [214] and paraffin oil [215] for comparison. The HSPs for thirty candidate bio-derived alternative solvents and their HSP distance and RED relative to the two solutes of interest are listed in Table 7. The HSPs for each solvent were acquired from several sources [68,214,216,217]. Nine of the candidate solvents were predicted to be good solvents for UHMWPE, and 1,4-cineole was the one most likely to be a good solvent for graphene. Dissolution of UHMWPE in 1,4-cineole at concentrations consistent with commercial gel spinning methods (2-3 wt%) was confirmed by heating UHMWPE powder in the solvent above the melting point of UHMWPE and stirring until a highly viscous solution was formed. 1,4-cineole is a monoterpene found in plant extracts containing 1,8-cineole, such as eucalyptus oil or cardamom, and can be synthesized from another terpene, α-terpineol [218]. It has received growing attention in biological and medical research for its anxiolytic and antidepressant properties [219], it has been demonstrated as an effective bio-derived degreaser in industrial

applications [220], and it has been shown to be an important component of the flavor profile of Australian Cabernet Sauvignon red wine [221].

***Table 7**. HSPs of the materials investigated in this study including the target solutes (*). The commercially prominent solvents for UHMWPE gel spinning are included for reference (†) and the remainder are the candidate bio-derived alternatives. RED values indicating good solubility with the corresponding solute (RED < 1) are shown bolded in green, and RED values indicating poor solubility (RED > 1) are shown in red. All terms other than RED have units of $MPa^{1/2}$*

				UHMWPE R_0 = 4.0		**Graphene R_0 = 6.5**		
Material	**δ_d**	**δ_p**	**δ_h**	**R_a**	**RED**	**R_a**	**RED**	**Ref**
UHMWPE*	18	1.2	1.4	-	-	-	-	[213]
Graphene*	18	9.3	7.3	-	-	-	-	[68]
Decalin†	17.6	0	0	1.844	***0.461***	11.823	*1.819*	[214]
Paraffin oil†	15.7	2.7	8.7	8.758	*2.189*	8.166	*1.256*	[215]
1,4 Cineole	17.1	3.6	3.7	3.780	***0.945***	6.978	*1.074*	[217]
1,8-Cineole	16.7	4.6	3.4	4.724	*1.181*	6.638	*1.021*	[217]
Artemisia keton	15.9	5.8	5.1	7.245	*1.811*	5.893	***0.907***	[217]
Bisabolene	16.7	2.2	4	3.811	***0.953***	8.250	*1.269*	[217]
Butyl lactate	15.8	6.5	10.2	11.175	*2.794*	5.967	***0.918***	[68]
Carvone	18	5.6	6.4	6.660	*1.665*	3.808	***0.586***	[217]
Citral	16.3	2.3	6.2	5.984	*1.496*	7.859	*1.209*	[217]
Citronellol	16.2	5.9	5.2	7.035	*1.759*	5.379	***0.827***	[217]
Cyrene	18.8	10.6	6.9	11.008	*2.752*	2.100	***0.323***	[68]
Dipentene	16.7	2.2	4	3.811	***0.953***	8.250	*1.269*	[217]
D-limonene	17.2	1.8	4.3	3.366	***0.842***	8.235	*1.267*	[68]
Eugenol	19	7.5	13	13.351	*3.338*	6.303	***0.970***	[68]
γ-valerolactone	16.9	11.5	6.3	11.616	*2.904*	3.268	***0.503***	[68]
Geraniol	16	4.7	11	10.973	*2.743*	7.131	*1.097*	[216]
Linalool	16.5	2	9.1	8.302	*2.076*	8.095	*1.245*	[217]
Linalyl acetate	16	2.8	5.5	5.947	*1.487*	7.842	*1.206*	[217]
Menthone	17	8.1	4.4	7.785	*1.946*	3.722	***0.573***	[217]
Myrcene	16	2.2	5.1	5.540	*1.385*	8.441	*1.299*	[217]
Nerolidol	16.4	2.7	8.7	8.110	*2.028*	7.467	*1.149*	[217]
Ocimene	15.8	3.2	4.7	5.852	*1.463*	7.958	*1.224*	[216]
Phellandrene	16.9	1.8	4.1	3.534	***0.884***	8.446	*1.299*	[217]
Pinene	17.4	3	3.2	2.814	***0.704***	7.612	*1.171*	[216]
Piperitone	17	6.2	4.5	6.214	*1.553*	4.631	***0.713***	[217]
Sylvestrene	16.6	3	4.1	4.286	*1.072*	7.601	*1.169*	[217]
Terpinene	17.2	1.8	4.3	3.366	***0.842***	8.235	*1.267*	[217]
Terpineol	17	5.3	10.9	10.539	*2.635*	5.741	***0.883***	[217]
Terpinolene	16.9	1.8	4.1	3.534	***0.884***	8.446	*1.299*	[217]
Triacetin	16.5	4.5	9.1	8.898	*2.225*	5.940	***0.914***	[68]
Umbellulone	17.7	6.6	4.1	6.067	*1.517*	4.230	***0.651***	[217]
Zingiberene	16.6	1.4	4.1	3.895	***0.974***	8.972	*1.380*	[217]

2.2. Materials

UHMWPE powder with an average molecular weight of 3M-6M g/mol (Sigma-Aldrich) was used as the feedstock polymer. Food-grade 1,4-cineole (≥95%, Sigma-Aldrich) was used to disperse GnPs (XG Sciences, xGNP C-750) and dissolve the UHMWPE powder. 2,6-Di-tert-butyl-4-methylphenol (Sigma-Aldrich) was used as an antioxidant. Food-grade orange terpenes, decahydronaphthalene (decalin), and paraffin oil, all purchased from Sigma-Aldrich, were used to compare the solution stability of GnPs in each solvent presented in this study. All chemicals were used as delivered without further purification.

2.3. Sample Preparation

2.3.1. 1,4-Cineole Properties

The viscosity of 1,4-cineole was measured using a Thermo Scientific HAAKE Viscotester iQ Air in parallel plate geometry with a ramped shear rate range from 10-1000 1/s. The surface tension of 1,4-cineole was estimated via pendant drop tensiometry. Droplet images were taken using a Ramé-Hart automatic goniometer (Model 290-F4), and the surface tension was calculated using the associated DropImage Advanced software.

2.3.2. Graphene Dispersion

To observe the stability of GnP suspensions over time, GnPs were dispersed in various solvents at a concentration 1 mg GnPs / 1 mL solvent via ultrasonication in a Branson ultrasonic bath for 90 minutes. The suspensions were created simultaneously and photographed at regular intervals over the course of 40 days. To disperse GnPs for UHMWPE/GnP composite gel formation, shear mixing and ultrasonication were used successively prior to the dissolution of the UHMWPE powder and antioxidant. Shear mixing was conducted using a Silverson L5M-A laboratory high-shear mixer with a 5/8” mix head and slotted stator operating at 7500 rpm for 1 hour. The solution

was then ultrasonicated (Sonics VCX 500) at 20 KHz with a 1/4" probe tip operating at 30% amplitude and pulsing on for 9 seconds and off for 1 second for 30 minutes. The solution was contained in a jacketed beaker with flowing water to maintain the solution temperature at 20°C during shear mixing and ultrasonication. A GnP concentration of 0.266 mg/mL was used as the primary concentration for nanocomposite formation and lower concentration solutions were formed by diluting the parent solution.

2.3.3. Polymer Solution Formation

UHMWPE powder and 2,6-di-tert-butyl-4-methylphenol were added to pure 1,4-cineole for the control sample and 1,4-cineole/GnP dispersion for the experimental nanocomposite samples. Preliminary trials indicated that 3 wt% UHMWPE was optimal for fiber spinning pure and nanocomposite fibers in the concentrations selected for this study. So, in all solutions, the UHMWPE concentration was 3 wt%, and the antioxidant concentration was 0.3 wt%. The GnP concentration was varied by orders of magnitude from 0.01 wt% to 1.0 wt% relative to the UHMWPE to identify a concentration decade of peak performance and understand the evolution of the fiber microstructure and properties across relevant decades. Increasing the GnP concentration to 10 wt% led to phase separation during extrusion and continuous fibers could not be spun. Dissolution of the UHMWPE occurred at elevated temperature in a heated silicone oil bath while under direct ultrasonic agitation using a custom 1/4-inch sonicating probe designed for use at 150-170°C. The ultrasonication amplitude was set to 20% and was pulsed at 5 second on and 1 second off intervals. Dissolution occurred in less than 20 minutes resulting in an evenly dispersed and highly viscous polymer solution.

2.3.4. Fiber Spinning and Drawing

Upon formation, the polymer solution was immediately transferred to the barrel of a custom gel spinning extruder, see Chapter 3 section 2.1, that was preheated to 130°C. The solution was allowed to equilibrate in the barrel for 5 minutes before inserting the extruder piston and evacuating the air from the barrel. The system was allowed to equilibrate for an additional 5 minutes before beginning fiber spinning. The solution was extruded through a nozzle with an orifice diameter of 250 μm and channel length of 500 μm. The extruded gel fiber descended a 20 cm air gap before entering a coagulation bath of deionized water at ambient temperature. The fiber was immersed in the coagulation bath for 68 cm before being taken up at 2.5 m/min on a winding bobbin. Solvent extraction was completed via evaporation in ambient air for no less than 24 hours. The as-spun fibers were hot drawn at a ratio of 5:1 by passing the fiber over a polished and lubricated aluminum plate heated to 110°C using two driven bobbins. The draw ratio is defined as the ratio of the speed of the takeup bobbin to the payout bobbin.

2.4. Characterizations

2.4.1. Morphological Analysis

Transmission electron microscopy (TEM, FEI Titan) was used to characterize the morphology of the GnPs after shear mixing and ultrasonication. The dispersed graphene suspension was deposited onto lacey carbon TEM grids immediately following shear mixing and ultrasonication and dried at 65°C under vacuum. The profile and surface of the fibers were observed via scanning electron microscopy (SEM, FEI Quanta 650). All SEM samples were sputter coated with gold (Cressington 108 Auto/SE) to prevent charging during SEM. The dispersion and geometry of the graphene particles in the UHMWPE matrix were observed via atomic force microscopy (AFM) operated in tapping mode. Samples for AFM analysis were prepared by aligning fibers vertically

in an epoxy mount and polishing to expose their axial cross sections. Measurements were taken using a Bruker Dimension Icon AFM, using an OTESPA-R3 (Bruker) probe with a nominal tip radius of 7 nm. Maps of entire fiber cross sections were obtained to assess the spatial distribution and frequency of embedded particles. Close-up detail images of representative particles were then obtained to identify morphology. During analysis, particles adsorbed to the fiber surfaces were not included in distribution evaluation.

2.4.2. Thermal Properties

A Netzsch STA 449 F1 Jupiter Simultaneous Thermal Analyzer was used to conduct differential scanning calorimetry (DSC) and thermogravimetric analysis (TGA) experiments on the fiber samples. The fibers were cut into short lengths and 3 ± 0.2 mg of each sample were placed in aluminum crucibles. Pierced lids were cold weld crimped onto the crucibles to ensure contact between the sample and the crucible bottom while allowing any vaporized material to escape. A two-cycle heating routine was applied to observe the effect of spinning and drawing then observe the behavior of the material after the thermal history is erased. The samples were heated to 200°C at a rate of 10°C/min and cooled twice. A 30-minute isothermal hold was applied after the first ramp to 200°C to observe any mass loss above the boiling point of the spin solvent.

2.4.3. Mechanical Properties

The mechanical properties of the fibers produced in this study were evaluated via single-filament tensile testing according to ASTM standard D3822 using an MTS Nano Bionix Universal Testing Machine (UTM). The UTM has a maximum load capacity of 500 mN and 150 mm of extension. A gauge length of 10 mm was selected for this study, and at least 20 successful tests, as defined by the standard, were recorded for each sample. The mechanical properties are reported in

textile units (cN/dtex), and a Mettler-Toledo XSE205DU analytical balance was used to measure the linear density of the fiber samples according to ASTM standard D1577.

2.4.4. Microstructural Analysis

The characteristics of the GnPs before and after dispersion in 1,4-cineole were examined via Raman spectroscopy using a Renishaw inVia Confocal Raman microscope with a 50x objective lens and 514 nm wavelength laser. Wide-angle and small-angle X-ray scattering, WAXS and SAXS respectively, of the experimental fibers were used to assess the crystalline characteristics of the fibers. WAXS was conducted with a Bruker D8 Venture in Debye-Scherrer configuration. The fibers were illuminated with monochromated (Helios™ monochromator, multilayer optics) Cu-Kα radiation (λ=0.154184 nm) and diffraction patterns were collected with a Photon III 2D detector. To obtain 1D patterns, the 2D frames were integrated over a 90° azimuthal region for determination of the crystallite sizes and overall crystallinity. The same WAXS quantitative analysis methods used in Chapter 3 of this dissertation were applied to the WAXS data collected for this chapter. See equations 3.1-5.

SAXS experiments were performed using a Xenocs Xeuss 3.0 SAXS/WAXS equipped with a GeniX 3D Cu HFVLF microfocus X-ray source utilizing Cu Kα radiation (λ = 0.154 nm). The sample-to-detector distance was 900 mm, and the q-range was calibrated using a silver behenate standard. Two-dimensional scattering patterns were obtained using a Dectris EIGER 4M detector with an exposure time of 2 hours. Data reduction was performed using XSACT software provided by Xenocs. Semicrystalline polymers possessing lamellar crystal mesostructures exhibit meridional lobes in 2D SAXS scatter patterns, which arise from alternating domains of higher and lower electron density [194]. The length of this repeating pattern, or the center-to-center spacing

of the lamellar crystals, is called the long period (L). This can be calculated from the q of peak scattering intensity along the fiber axis (q_{max}), Equation 4.3.

$$L = \frac{2\pi}{q_{max}} \tag{4.3}$$

3. Results and Discussion

3.1. Graphene Suspension in 1,4-cineole

Three key characteristics have been identified as strong predictors for a solvent that can achieve stable dispersion and efficient exfoliation of graphene: polarity, surface tension, and viscosity [68]. None of these three can independently predict a solvent's suitability for graphene, but together they can form an efficient framework for evaluating solvents using directly measurable qualities. This has been applied effectively for evaluating environmentally friendly alternatives to the harmful petrochemical solvents, n-methylpyrrolidone (NMP) chief among them, that are known for excellent graphene dispersion [68]. The most commonly used characteristic for evaluating a candidate solvent is Hansen solubility parameters (HSP) because the similarity of the solvent's polarity with graphene's polarity is a strong predictor of a good solvent. HSP is especially relevant in this study since the solvent must also be a good solvent for UHMWPE to enable gel spinning. Three parameters, dispersion energy (δ_d), polar-dipolar energy (δ_p), and hydrogen bonding energy (δ_h), can be ascribed to any material, and they provide a convenient coordinate system, called Hansen space, for visualizing the HSP relationships between materials. Each material also possesses an interaction radius (R_0), and if the position of a solvent in Hansen space falls within the interaction radius of the solute, then the solvent is described as a "good" solvent for the solute. Of the 30 bio-derived solvents evaluated in this study, none were simultaneously "good" solvents for UHMWPE and graphene according to HSP, so a candidate capable of solvating UHMWPE that was also closest to being a "good" solvent for graphene, 1,4-cineole, was selected. This was

hardly discouraging considering that 1,4-cineole was very nearly inside the interaction radius of graphene, whereas the leading solvents for UHMWPE fiber gel spinning, paraffin oil (PO) and decalin, are predicted to be poor solvents for graphene via HSP, Figure 29.

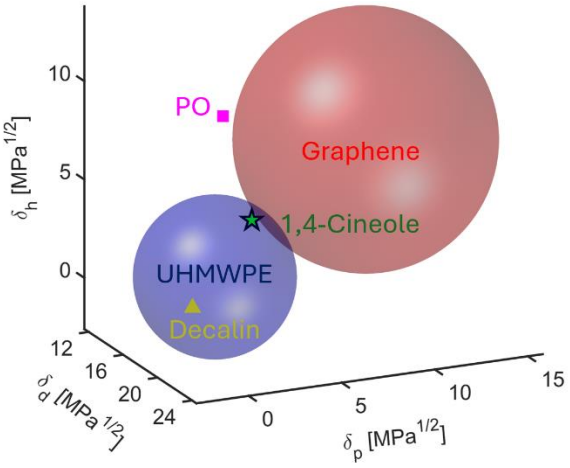

***Figure 29**. HSP space showing the relationship between the solutes of interest, UHMWPE (blue sphere) and graphene (red sphere), commercially prominent UHMWPE fiber spin solvents, paraffin oil (PO, pink square) and decalin (yellow triangle), and the bio-derived alternative candidate, 1,4-cineole (green star)*

This prediction was then tested by dispersing GnPs in 1,4-cineole at a concentration of 1 mg/mL via ultrasonication for 90 minutes. This procedure was also applied in parallel to the two leading solvents for commercial UHMWPE gel spinning, paraffin oil and decalin, as well as orange terpenes for comparison [25,89,91,133]. Photographs were taken of the dispersions in each solvent at regular intervals over the course of several weeks, and it was found that the graphene suspension in 1,4-cineole possessed remarkable stability. 40 days after the initial ultrasonic dispersion, the GnPs had settled out of each solvent except for 1,4-cineole, Figure 30.

Of the solvents tested, 1,4-cineole was closest to meeting the criteria for a good solvent per HSP, but this result far exceeded expectations considering that HSP does not predict it to be a "good" solvent for graphene. The two other key indicators of a good solvent for graphene dispersion, viscosity and surface tension, were then considered to explain this phenomenon. At the time of this dissertation, neither of these properties could be found in manufacturer datasheets or

academic literature, so they were measured via parallel plate viscometry and pendant drop tensiometry respectively.

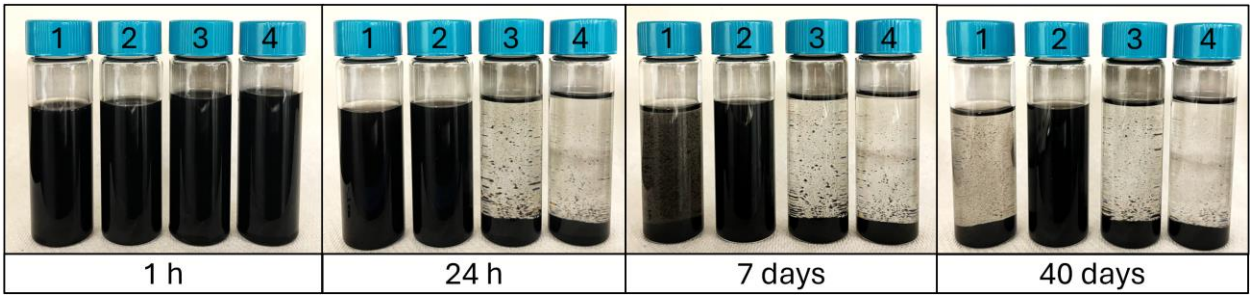

***Figure 30**. Timelapse photos of graphene dispersions in various solvents with concentration of 1 mg/mL: 1) paraffin oil, 2) 1,4-cineole, 3) decalin, and 4) orange terpenes*

A minimal ratio of solvent density to viscosity reduces particle settling velocity, according to Stoke's law, resulting in more stable dispersions [68], and higher viscosities increase the shear force that can be applied during rotary shear exfoliation thereby increasing exfoliation efficiency [65]. This effect is well demonstrated by the relatively stable dispersion of paraffin oil, Figure 30. HSP predicts that paraffin oil is a poor solvent for graphene, but the high viscosity of paraffin oil dramatically reduces the settling velocity of the particles. The viscosity of 1,4-cineole approaches an equilibrium value of 0.00171 Pa*s averaged across the shear rate range of 700-1000 1/s, Figure 31a. This is lower than that of decalin (0.00178 Pa*s [222]), from which the graphene suspension settled out in less than 24 hours, yet it maintained a suspension well beyond 40 days.

Solvents capable of stably dispersing graphene typically possess a surface energy similar to that of graphene (~40 mJ/m^2), which maximizes the affinity of graphene to the solvent thereby limiting the van der Waals attraction between nearby graphene flakes [223]. The surface energy of the solvent (called surface tension for liquids) can be measured via analysis of the shape of a droplet suspended from a needle, which is called the pendant drop method [224]. The droplet image for 1,4-cineole is shown in Figure 31b and associated dimensions measured and calculated using the software are included in Table 8. Seven measurements were taken at a frequency of 10

Hz and averaged. The surface tension of 1,4-cineole was measured to be 24.68 mJ/m^2, which is not in the range typically associated with good graphene dispersion [68]. Rather, it is close to that of ethanol (22.1 mJ/m^2), which has demonstrated varied degrees of efficacy for the exfoliation of graphene [225,226]. Principal component analysis conducted by Salavagione *et al.* [68] indicates that the role of surface energy is less specific than that of HSP or viscosity, but this mismatch in surface energy is significant.

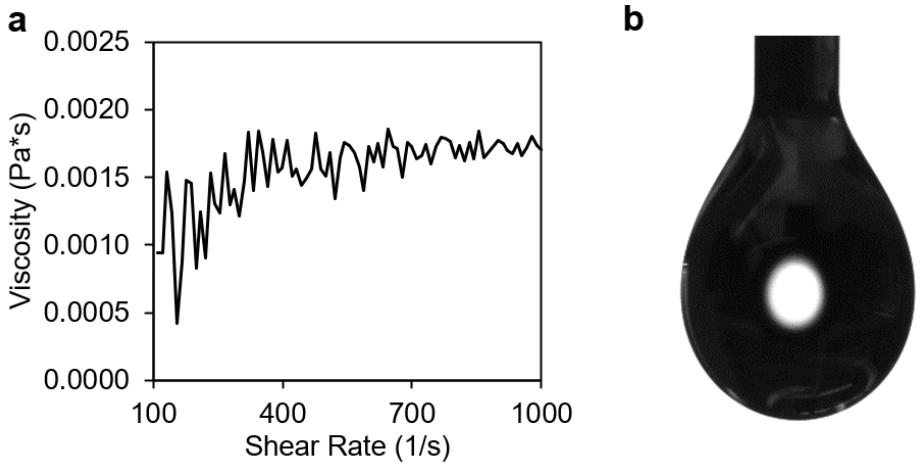

***Figure 31**. a) Dynamic viscosity measured via parallel plate viscometry across a shear rates ranging from 100-1000 1/s, and b) droplet image of 1,4-cineole for pendant drop tensiometry*

***Table 8**. Measurements of pendant drop tensiometry images of 1,4-cineole droplet.*

No.	**γ** (mN/m)	**β**	**R0** (mm)	**Area** (mm^2)	**Volume** (mm^3)	**Θ** (deg)	**Height** (mm)	**Width** (mm)
1	24.66	0.302	0.925	14.01	4.97	108.40	2.542	1.964
2	24.68	0.302	0.926	13.97	4.97	108.61	2.539	1.961
3	24.65	0.302	0.925	13.94	4.96	109.01	2.532	1.960
4	24.66	0.302	0.925	13.96	4.96	108.67	2.537	1.960
5	24.63	0.302	0.925	13.97	4.96	108.45	2.539	1.959
6	24.72	0.301	0.926	13.96	4.96	108.90	2.535	1.964
7	24.78	0.301	0.926	13.90	4.95	110.30	2.514	1.962
Mean	**24.68**	**0.302**	**0.925**	**13.96**	**4.96**	**108.91**	**2.534**	**1.961**

Considering that 1,4-cineole only meets one of the three criteria set out by Salavagione et al. [68] for evaluating candidate solvents for graphene dispersion and exfoliation, Table 9, the stability of the GnP dispersion in it is unexpected. However, computational methods have provided new insights into seemingly anomalous cases such as this. A key aspect common to good solvents for graphene dispersion is the formation of a structured solvent layer at the graphene particle surface. Molecular dynamics simulations and density functional theory have shown that this is achieved for molecules with a π-electron system that can align parallel to the graphene sheet and has an opposing saturated section that creates a steric barrier repelling nearby graphene sheets and preventing stacking [227]. The formation of this structured layer constitutes a solvation shell, and it has been shown that reaggregation is less likely in solvents with low diffusion coefficients along the graphene layer [228].

Table 9*. Comparison of 1,4-cineole to target properties for three key characteristics that indicate a solvents suitability for dispersing and exfoliating graphene.*

Measurement	**Target** [68]	**1,4-cineole**
Polarity (HSP distance, $MPa^{0.5}$)	< 6.5	6.98
Surface Tension (mN/m)	38.2 +/- 6	24.7
Density/Viscosity ($s*m^2$)	$< 1.2*10^6$	$5.19*10^5$

3.2. Nanoparticle Morphology

A two-stage dispersion and exfoliation method was applied to 1,4-cineole/GnP suspensions prior to the dissolution of UHMWPE to ensure that the particles were well dispersed and deagglomerated. Discerning the nature of the particles after this process is crucial to understanding how the particles are incorporated into the polymer matrix, so the particle dimensions were measured via TEM and particle quality was measured via Raman spectroscopy. The shear mixed and ultrasonicated particles appear as wrinkled and folded multi-layer sheets, Figure 32a. High-resolution TEM (HRTEM) revealed the presence of single graphene layers, which can be

confirmed by the characteristic hexagonal diffraction pattern of graphene that appears in the fast Fourier transform of the a single-layer region of the HRTEM image, Figure 32b.

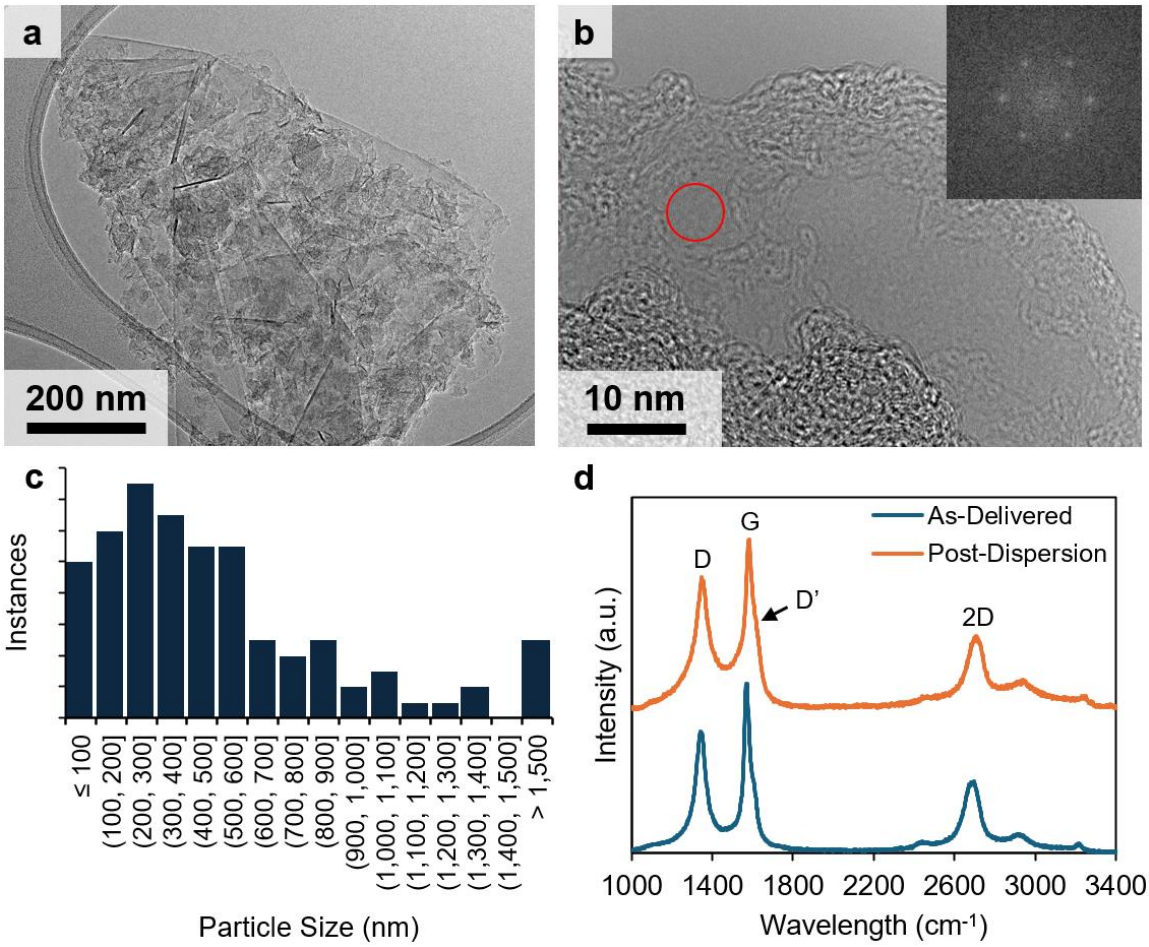

***Figure 32**. a) TEM image of a GnP deposited after the two-stage dispersion/exfoliation featuring wrinkled and folded graphene sheets, b) HRTEM image of a region of a GnP showing a single layer region with an inset of the fast Fourier transform of the region encircled in red showing the hexagonal diffraction pattern characteristic of graphene, c) a histogram of the maximum dimension measured of 100 randomly selected particles viewed with TEM, and d) Raman spectra of the GnPs as delivered and after dispersion with relevant peaks labeled for reference.*

The average maximum dimension of 100 randomly selected particles viewed via TEM was 558 nm, and 88% of the particles had a major dimension less than 1 μm, Figure 32c. The relative ratios of the intensities of the G-peak and 2D-peak of the Raman response of the as-delivered and dispersed particles confirms that on average the particles are multilayer GnPs [229], Figure 32d. The ratio of the intensities of the D-band and G-band provides insight into the degree of disorder

in the particles [230], and it was found that the shear mixing and ultrasonication process only slightly increased this ratio from 0.71 to 0.78 indicating that the exfoliation process did not extensively damage the particles. The presence of the D' peak before and after dispersion and exfoliation indicates that multiple defect modes may be present as delivered from the GnP manufacturer [231], and they are unaffected during processing. These results indicate that the shear mixing and ultrasonication methods did not have a significant exfoliating effect but were effective at dispersing the agglomerated as-delivered particles.

3.3. Fiber Morphology

The UHMWPE fiber spun from 1,4-cineole solution exhibited oblong to flat cross sections sometimes featuring short lobes, as exemplified in Figure 33a.

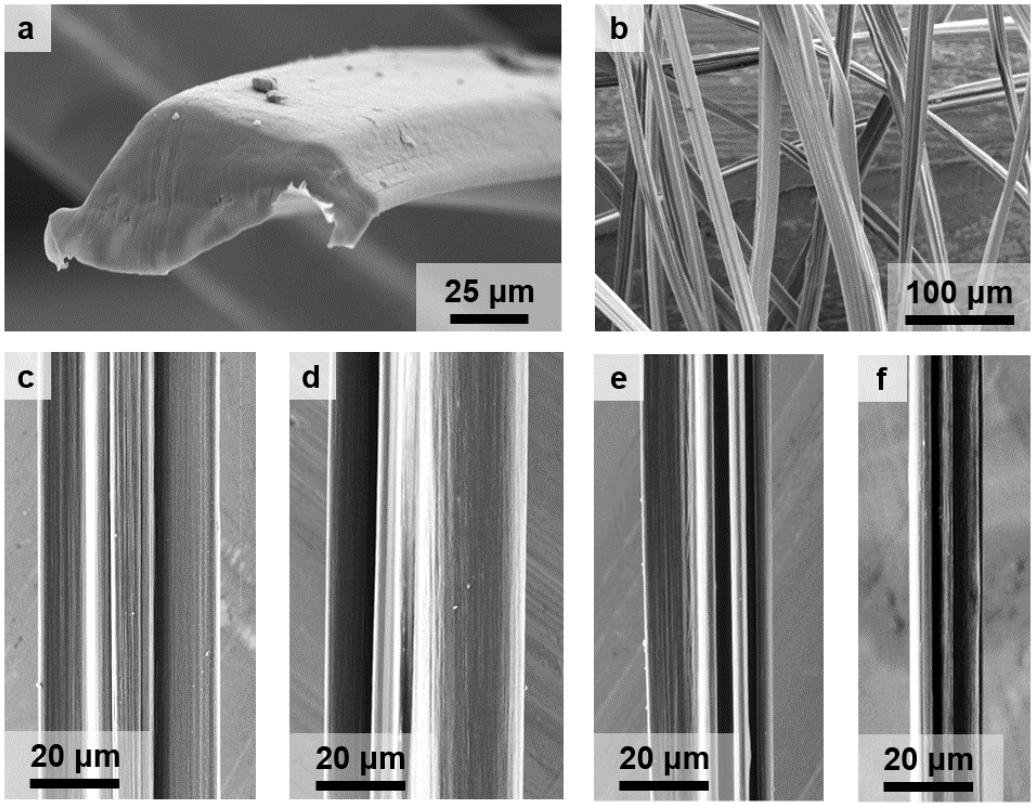

***Figure 33**. Scanning electron micrographs of a) a cryo-fractured cross-section of UHMWPE/GnP nanocomposite fiber as-spun, b) multiple UHMWPE/GnP fibers (1 wt% GnP) after 5:1 drawing highlighting their flat/oblong shape, and profile views of drawn UHMWPE fibers with GnP concentrations of c) 0 wt%, d) 0.01 wt%, e) 0.1 wt%, and f) 1 wt%*

No voids were present in the cross section of the fibers. Hot drawing at a ratio of 5:1 was accomplished for all graphene concentrations and the control sample without affecting the cross-sectional shape of the fibers, Figure 33. While the linear density of the fibers increased from 0 wt% GnP to 0.01 wt% GnP, the linear density decreased with increasing GnP concentration thereafter, Table 10. As has been shown in the electrospinning of polymer/graphene solutions [232], increasing the graphene concentration increased the viscosity of the polymer solution, which led to increased draw down during spinning and a lower final linear density. The surfaces of the drawn fibers feature the axial striations characteristic of UHMWPE fibers indicating the alignment of the fiber molecule chains, Figure 33c-f. The irregular cross-sectional profile of the fibers results from the relationship between the crystallization rate of the gel and the diffusion rate of the solvent. This is a common feature of UHMWPE fibers as well as other fibers spun using solvent dry extraction. An outer shell is formed as solidification proceeds from the outer surface inward, and the as-extruded round profile collapses [49]. Obtaining an in-depth understanding of the crystallization process for UHMWPE fibers spun using 1,4-cineole in a future study will shed light on the spinning conditions responsible for this morphology and may enable control of this geometry [183].

TGA showed that the fibers exhibited less than 1.5% mass loss after an initial ramp to 200°C. An equilibrium residual mass of 96.4% was reached for the as-spun pure UHMWPE fibers after a 30 min hold at 200°C. The slow rate of mass loss well above the boiling temperature of 1,4-cineole indicates that the remaining residue may be higher molecular weight impurities in the solvent, which is unsurprising considering that it is a food-grade material that may contain as much as 5% impurities. The residual mass of the drawn fibers after the initial 30 min isotherm was slightly lower than the as-spun fibers, Table 10. The addition of GnPs did not affect this result. However,

the residual mass changed slightly corresponding to the linear density of the fibers. Considering the lower mass loss of the as-spun fibers, which are much larger than the drawn fibers, it can be concluded that the diffusion rate of the residue at elevated temperature was inversely related to the linear density of the fibers and not affected by the concentration of GnPs.

***Table 10**. Linear density of the sample fibers as measured via ASTM D1577 and the residual mass measured via TGA following a ramp of 10°C/min to 200°C and 30 min isotherm at that temperature. Samples are listed by their GnP concentration in wt%*

	As-Spun	**Drawn**			
	0 wt%	0 wt%	0.01 wt%	0.1 wt%	1 wt%
Linear Density (dtex)	11.72	2.77	3.44	2.45	1.25
Residual Mass (%)	96.5	95.1	95.4	95.2	94.9

SEM images of the nanocomposite fibers did not reveal any large agglomerations on or near the fiber surfaces, and AFM was employed to identify particles within the UHMWPE matrix from polished cross sections of the fibers. Tapping amplitude error mapping of entire fiber cross sections revealed the presence of several randomly distributed, sub-micron particles, Figure 34a. High resolution scanning of individual particles showed atomic layer stepping indicative of the wrinkled and layered morphology of the GnPs as viewed under TEM, Figure 34b. The size of the particles in the matrix was consistent with the size distribution measured via TEM indicating that the particles remained well dispersed during the dissolution of UHMWPE and spinning of the fibers. This shows that ultrasonic agitation is a viable method of maintaining nanoparticle dispersion during the formation of semi-dilute polymer/nanoparticle solutions for fiber gel spinning.

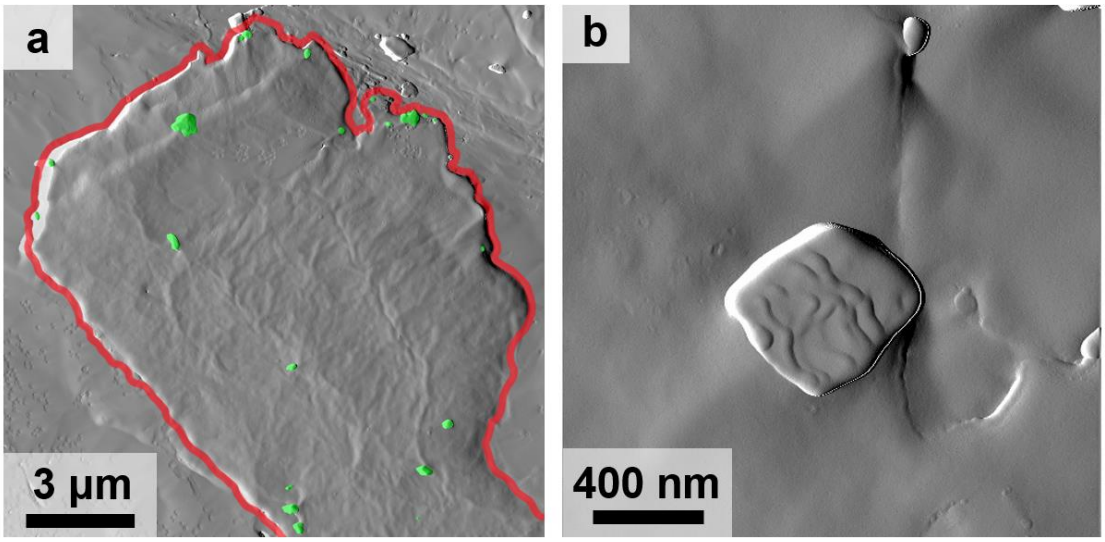

***Figure 34**. AFM tapping amplitude error images of a) the cross section of a drawn UHMWPE / 1 wt% GnP nanocomposite fiber outlined in red with exposed nanoparticles highlighted in green, and b) an individual GnP showing stacked graphene layers*

3.4. Fiber Mechanical Properties

UHMWPE fibers spun from a 1,4-cineole solution and hot drawn at a ratio of 5:1 exhibited an average breaking tenacity, 8.08 cN/dtex, commensurate with that of fibers spun from orange terpenes at the same draw ratio, 8.58 cN/dtex, with a significantly greater strain to failure [133]. In the context of commercial fibers and experimental fibers presented in literature, the fibers fall onto a power law curve relating the strain to failure and initial modulus in UHMWPE fibers, Figure 35. A loose direct relationship between draw ratio and strain to failure can also be observed in Figure 35, so it can be expected that the tensile properties of these fibers can be improved significantly by increasing the draw applied to the fibers. This demonstrates significant potential in 1,4-cineole as a UHMWPE fiber spin solvent with lower environmental impact given further optimization of the spinning and drawing processes.

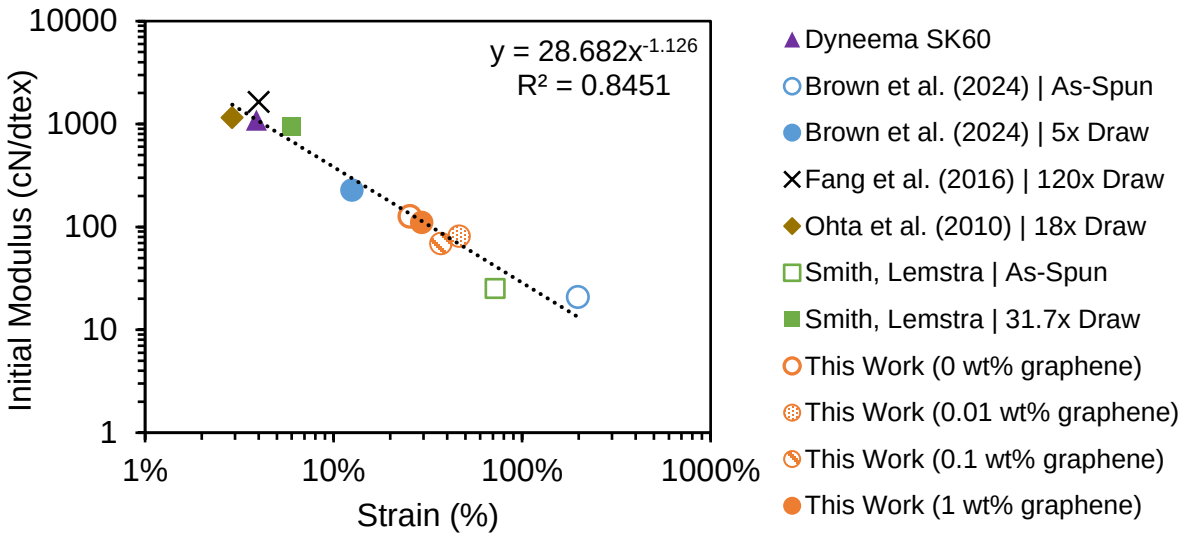

***Figure 35**. Log-log plot comparing initial modulus and strain to failure across several fibers produced commercially or experimentally*

However, the addition of GnPs did not provide the anticipated reinforcing effect. The tensile properties of the fibers declined precipitously at low GnP concentrations while mostly recovering at a concentration of 1 wt% without exceeding the properties of the pure UHMWPE fibers, Table 11. A similar result was reported by Dayyoub *et al.* [233] wherein drawn UHMWPE/GnP films at 0.1 wt% and 1.0 wt% GnP showed reduced mechanical properties compared to the pure UHMWPE control sample. However, a robust understanding of why the addition of these particles falls short of their promise has not previously been presented in literature. Accordingly, a battery of microstructural characterizations was undertaken to understand the mechanism underlying this result. The first hint at the nanoparticles' interaction with the polymer matrix lies in the reduction in the coefficient of variation (COV) of the initial modulus and breaking tenacity with increasing graphene concentration, which indicates that the nanoparticles tend to regulate the microstructure development in the fibers rendering more consistent tensile properties between test samples [64].

***Table 11**. Tensile properties and corresponding coefficient of variation (COV) of UHMWPE and UHMWPE/GnP fibers at varying GnP concentrations. Average tensile properties are shown ± standard error*

	Initial Modulus		Breaking Tenacity		Strain at Failure	
	cN/dtex	COV (%)	cN/dtex	COV (%)	%	COV (%)
0 wt%	127.4 ± 5.1	17.5	8.08 ± 0.12	6.7	25.3	37.6
0.01 wt%	81.7 ± 2.5	16.6	4.35 ± 0.08	10.2	46.3	44.8
0.1 wt%	69.4 ± 1.2	9.0	3.93 ± 0.04	5.2	37.0	35.5
1.0 wt%	111.1 ± 1.6	6.8	7.03 ± 0.08	5.2	29.3	39.9

3.5. Fiber Thermal Properties

The thermal properties of the fibers are a critical component of their functionality, and they provide a window into the bulk microstructure of the fibers as well. DSC was used to assess the initial melting onset (T_o) temperature and peak melting temperature for the first (T_{p1}) and second (T_{p2}) melt cycles, Figure 36.

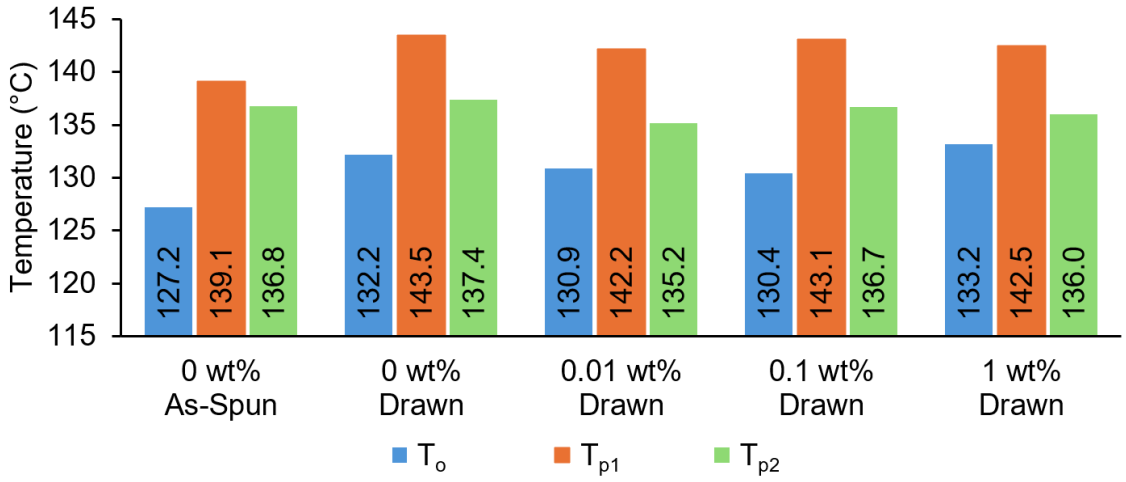

***Figure 36**. First cycle melting onset (T_o), first cycle melting peak (T_{p1}), and second cycle melting peak (T_{p2}) temperatures for pure and nanocomposite UHMWPE fibers spun using 1,4-cineole*

The as-spun and drawn pure UHMWPE fibers exhibited melting temperatures consistent with those spun using orange terpenes and drawn to the same degree [133]. The drawing process increased the melting onset and peak temperatures indicating increased molecular order [16]. This

is advantageous because it increases the maximum temperature that can be applied for a second drawing of the fibers, which can significantly increase the molecular alignment, crystallinity, and mechanical properties of the fibers [189]. The second melt cycle was included in the DSC routine to observe the melting behavior of the material after the thermal history has been removed by the first heating cycle. The pure UHMWPE fibers exhibited a slight increase in the second peak melting temperature from the as-spun to the drawn fibers (+0.6°C), which indicates that some irreversible microstructural change occurred during drawing, but the majority of the microstructural was reverted upon the first melting. The addition of GnPs slightly reduced the peak melting temperature of the fibers, but no correlation between the GnP concentration and peak melting temperature could be discerned. The 1 wt% GnP sample exhibited the greatest melting onset temperature indicating that the GnP concentration reached a threshold concentration where they begin to hinder molecular chain relaxation [234].

3.6. Fiber Microstructure

The microstructure of UHMWPE fibers is organized in hierarchical structures ranging from nano- to micro-scale formed largely of crystalline phases interspersed with amorphous and tie molecules that transfer the load between crystallites in the fiber. The development of crystalline microstructures with long range order is the key feature of UHMWPE enabling its remarkable mechanical properties; the theoretical modulus of a polyethylene chain has been estimated at zero temperature to be 374 GPa [235], and quantum mechanical analysis of polyethylene crystals estimates up to 326 GPa [236]. This has nearly been realized in highly drawn crystalline polyethylene nanofibers (312 GPa) [237], and commercially produced UHMWPE fibers achieve a significant portion of that (up to 200 GPa) [238]. DSC and X-ray scattering of the fibers offers

insight into the bulk crystallite characteristics in these fibers, which is crucial to understanding process-structure-property relationships for this material.

3.6.1. Crystallinity

The bulk crystallinity of the UHMWPE fibers spun using 1,4-cineole is consistent with those spun using orange terpenes and drawn to the same degree [133], which implies a similar level of microstructural development. The crystallinity of a semicrystalline polymer can be measured via DSC by comparing the measured melting enthalpy of the sample material (Δh_m) to the melting enthalpy of a perfectly crystalline version of that polymer (Δh_u), as shown in Equation 4.4.

$$\chi_{dsc} = \frac{\Delta h_m}{\Delta h_u} \tag{4.4}$$

The melting enthalpy of a polyethylene crystal has been estimated to be 293 J/g [185]. The effect of fiber drawing is evident in the increase in the crystallinity from as-spun to drawn for the neat (0 wt% GnP) UHMWPE fibers, Figure 37.

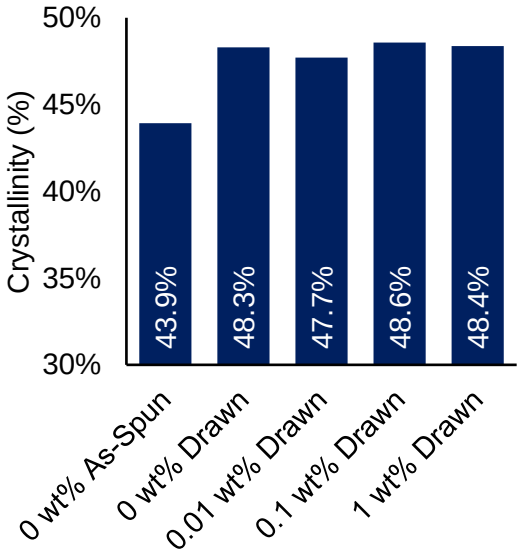

***Figure 37**. DSC-measured crystallinity of UHMWPE fibers spun with 1,4-cineole*

The hot drawing process increased the crystallinity of the fibers by 4.4% indicating that the residual material did not prevent strain-induced crystallization of the amorphous phase, Figure 37. This is visually identifiable by the deeper endothermic peak of the drawn fiber, which is shifted to a higher temperature, Figure 38a. However, the DSC-measured crystallinity was not sensitive to the incorporation of GnPs, Figure 37.

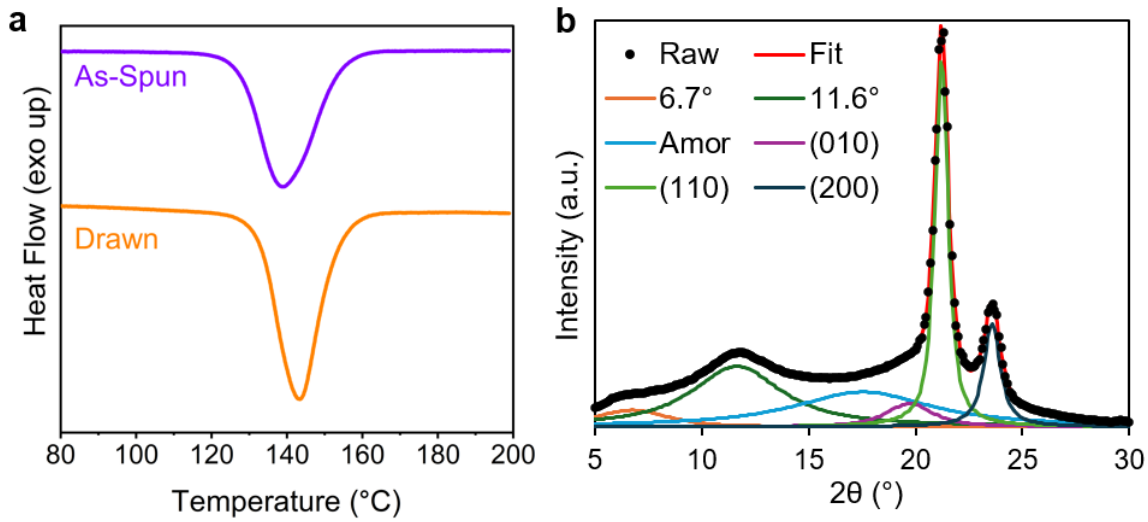

***Figure 38**. a) DSC thermograms of the melting endotherm for as-spun and drawn neat UHMWPE fibers, which shows the increased melting onset and peak temperatures as well as the larger area of the endotherm indicating greater crystallinity. b) 1D WAXS scattering of a drawn UHMWPE fiber with six peak fit*

Greater detail on the crystalline phase composition in the fibers can be achieved via WAXS. The primary crystallographic phases of UHMWPE are orthorhombic and monoclinic. The former can be identified by WAXS peaks at approximately 21.2° and 23.6° 2θ corresponding to the (110) and (200) planes and typically make up the vast majority of the crystalline content of the fiber. Monoclinic crystals are indicated by the (010) reflection occurring at approximately 19.6° 2θ, which is oftentimes obscured by the intensity of the adjacent orthorhombic peak. The UHMWPE fibers spun in this work exhibited these characteristic peaks in addition to peaks at 6.2° and 11.7° 2θ and a broad underlying peak at 17.5° 2θ ascribed to the amorphous phase, Figure 38. The lattice spacing corresponding to the 11.7° 2θ peak is approximately the sum of the primary orthorhombic

reflection (110) lattice spacing, 0.419 nm, and the thickness of a 1,4-cineole molecule, which indicates the intercalation of the residual solvent molecules into the crystalline structure of the fibers [239]. The peak at 6.2° 2θ has a lattice spacing approximately double that of the first order intercalated structure.

Peak deconvolution allows for quantitative analysis of these peaks, which can be used to assess the crystallinity of the fibers and crystallographic dimensions. The concentration of each phase is summarized in Table 12. The WAXS-measured crystallinity of the drawn fiber (74.0%) is greater than the DSC-measured crystallinity (48.3%), as is typically expected [190,193] consistent with other works [133]. However, it is lower than that of fibers spun using decalin and drawn the same amount (83.4%) [16]. The intercalated phase and orthorhombic phase share an approximately equal portion of the crystallinity of the pure fibers which indicates significant integration of the solvent residue into the crystalline structure.

***Table 12**. Composition of the fibers' crystallinity by phase as measured via WAXS*

Crystallinity (%)	**0 wt%**	**0.01 wt%**	**0.1 wt%**	**1 wt%**
Orthorhombic	34.0	28.6	33.3	22.1
Monoclinic	5.4	6.0	5.8	6.4
Intercalated	34.6	33.8	33.5	36.2
Total	74.0	68.4	72.6	64.8

The bulk crystallinity of the fibers varies with the linear density of the samples from 0 wt% to 0.1 wt%. This reflects the effect of draw down during gel spinning on crystallization. The 0 wt% and 0.1 wt% samples have a similar linear density and similar crystallinity whereas the 0.01 wt% sample has a greater linear density and lower crystallinity. Greater draw results in greater crystallinity and vice versa, especially at low draw ratios [208,210]. However, at 1 wt% the crystallinity declines despite the decrease in linear density, which indicates that the GnPs disrupt

the crystallite growth that typically occurs during spinning and drawing. Within the bulk crystallinity at this GnP concentration, the orthorhombic phase concentration decreases significantly while the monoclinic and intercalated phases increase slightly. These variations are visualized in Figure 39. An increase in the monoclinic concentration is typically seen during lateral compression of orthorhombic crystals [194] and occurs at very high draw ratios [16]. The increase in the amorphous and intercalated phases coincides with the decrease in orthorhombic concentration as the drawing induced crystallization is physically limited by the presence of the GnPs. This latter mechanism is clearly represented in the effect of the GnPs on the crystallite dimensions discussed in the next section.

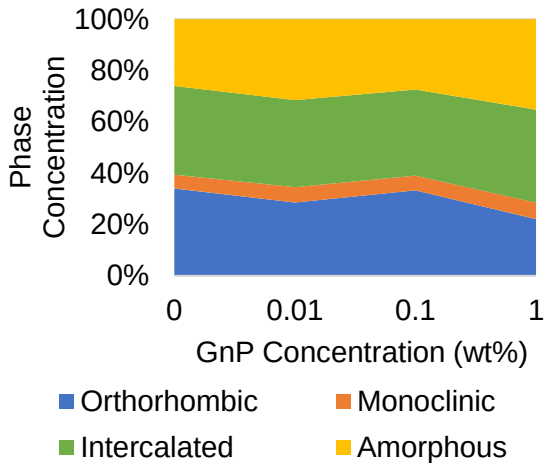

***Figure 39**. Total phase composition of the neat and nanocomposite UHMWPE fibers*

3.6.2. Crystalline Morphology

The crystalline phases of the UHMWPE fibers are organized into nanoscale and mesoscale structures that can be probed via WAXS and SAXS. During the gel spinning of UHMWPE, lamellar crystals are formed and oriented loosely towards the fiber axis during crystallization upon gel spinning [183,210]. Heated drawing of the fibers highly orients these crystals along the fiber axis and the lamellar crystals are converted into extended chain crystals with increasing draw ratio [16,240]. Ultimately, the crystallites are completely extended into fibrillar crystals, but the

intermediate structure is referred to as “shish-kebab”, owing to a combination of extended-chain crystals (shishes) skewering regions of folded-chain crystals (kebabs). This shish-kebab structure is identifiable by the presence of a equatorial streak and meridional lobes in the 2D SAXS patterns, wherein the equatorial streak is associated with the extended chain shish crystals and the meridional lobes are associated with the lamellar kebab crystals [211]. With and without GnPs, the sample fibers exhibited these general scattering features, Figure 40, which is consistent with UHMWPE fibers drawn to a similar degree [240].

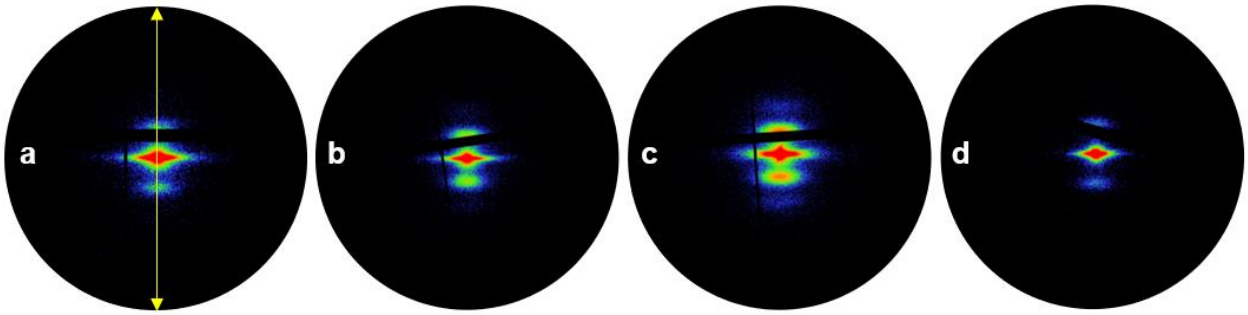

***Figure 40**. 2D SAXS patterns for the UHMWPE fibers with a) 0 wt%, b) 0.01 wt%, c) 0.1 wt%, and d) 1 wt% GnP concentration. All scattering patterns are rotated to align the fiber axis (equatorial direction) vertically as indicated by the yellow arrow in (a)*

The 2D SAXS patterns can be used to quantitatively measure the average axial dimensions of these crystallites based on the characteristics of the equatorial streak and meridional lobes, which arises from the electron density differences between the lamellar crystallites and other polyethylene phases. The average center-to-center spacing of adjacent lamellar crystals, referred to as the long period, can be measured via Bragg’s law of the peak position of the lamellar lobe from the 1D intensity curve along the fiber axis direction. The thickness of this lamellar crystal can be can be assessed by the 1D correlation function of the electron density distribution [241], which can be used to identify the long and short periodicity of the lamellar structure in the fibers. The lamellar crystals are composed of orthorhombic and monoclinic crystallites excluding the intercalated phase, which is not featured in the SAXS pattern meridional lobes due to its expanded

structure. Therefore, the short period is considered to represent the lamellar crystallites, and the difference between the long period and short period is composed of the intercalated crystallites, tie molecules, and the amorphous phase, Figure 41.

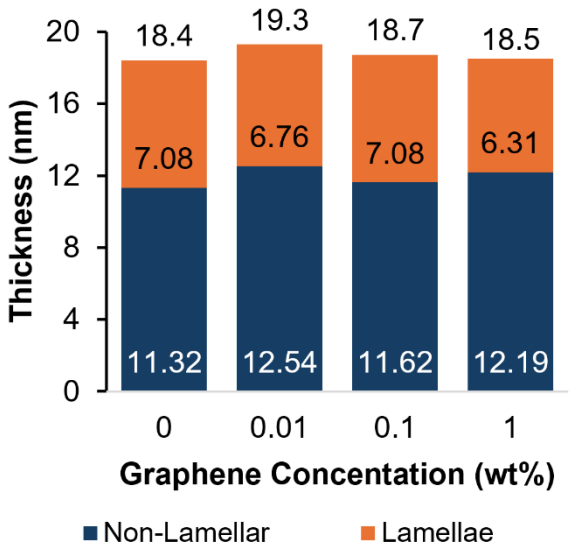

Figure 41. *Periodicity of the lamellar crystalline structure in the fibers showing the center-to-center spacing of the lamellae (bar total) and lamellae thickness as measured via SAXS*

The long period of the neat UHMWPE fibers spun using 1,4-cineole are similar to that of fibers using conventional spin solvents and drawn to a similar degree [211,240]. From 0 wt% to 0.1 wt% the short period is in keeping with the linear density of the fibers, but the short period shrinks at 1 wt% GnP, Figure 41. It is expected that the lamellar thickness and long period would increase with increasing draw down at a low total draw ratio because the amorphous molecules extend and strain-crystallize into the lamellar structure, which also extends [240]. However, at this concentration the GnPs prevent this anticipated extension resulting in a smaller than expected long and short periods.

The average lateral dimensions of the crystallites in the fibers can be related to the coherence length of the crystallographic planes determined via Scherrer's equation applied to the WAXS scattering along the fiber axis. These dimensions are detailed in Table 13. The lateral dimensions of the crystallites in these fibers are smaller than those spun using orange terpenes [133], which is

a consequence of the solvent residue intercalation observed in the 1D WAXS peaks. The WAXS-measured coherence length represents a bulk average in the material, and the presence of the intercalated phases disrupts the coherence length on average. The addition of GnPs had no effect on the lateral dimensions of the monoclinic crystallites, but the orthorhombic crystallites followed the trend of crystallinity and long period whereby a sharp decline occurred in the 1 wt% decade.

***Table 13**. Coherence lengths for the main crystallographic planes of the UHMWPE fibers of this study and orientation of the crystallites via Herman's Orientation Factor (HOF)*

	0 wt%	**0.01 wt%**	**0.1 wt%**	**1 wt%**
L_{010} (nm)	3.45	3.41	3.42	3.42
L_{110} (nm)	11.94	11.71	11.89	11.1
L_{200} (nm)	9.03	8.37	8.98	6.38
HOF	0.83	0.74	0.68	0.69

The average orientation of the crystallites is approximated by calculating Herman's orientation factor (HOF) from the WAXS peak of the major orthorhombic reflection (110), Table 13. The neat UHMWPE fibers exhibited significant orientation after drawing with a HOF of 0.83, which is consistent with other fibers spun under similar conditions albeit slightly lower [133,189]. The incorporation of GnPs negatively affected crystallite orientation. HOF decreased with increasing GnP concentration up to 0.1 wt% where it reached a floor that continued to 1 wt%, Table 13. The reduced crystallite growth at 1 wt% GnP is a symptom of this prevention of greater molecular alignment. By preventing the reorientation of the crystallites, they cannot coalesce into larger crystalline structures.

3.7. Mechanism of Structural and Tensile Property Evolution

Based on these characterizations, a mechanistic understanding of the interactions between GnPs and UHMWPE during fiber formation can be assembled. At low concentrations, the inclusion of GnPs exhibited little effect on the crystalline morphology of the fibers except for

inhibiting the orientation of the crystallites in the fiber direction, yet the tensile properties declined sharply. Therefore, despite being well dispersed, the particles act merely as point defects in the polymer matrix indicating poor load transfer at the nanoparticle-polymer interface. At 1 wt%, the concentration reaches a percolation threshold wherein the presence of the particles inhibits the growth of the crystallites during drawing. However, the mechanical properties exhibit a sharp increase compared to the lower concentration nanocomposite fibers. A network effect takes hold in this concentration decade whereby the particles reinforce the matrix despite their detrimental effect on the crystalline structure of the fibers. Although less aligned with the fiber axis and smaller, the crystallites are held in configuration against the GnPs, which promotes increased stiffness and breaking tenacity, Figure 42. Nevertheless, at 1 wt%, this effect is not strong enough to exceed the properties of the neat UHMWPE fibers. The negative impact of the inhibited microstructural development is greater than the reinforcing effect offered by the GnPs.

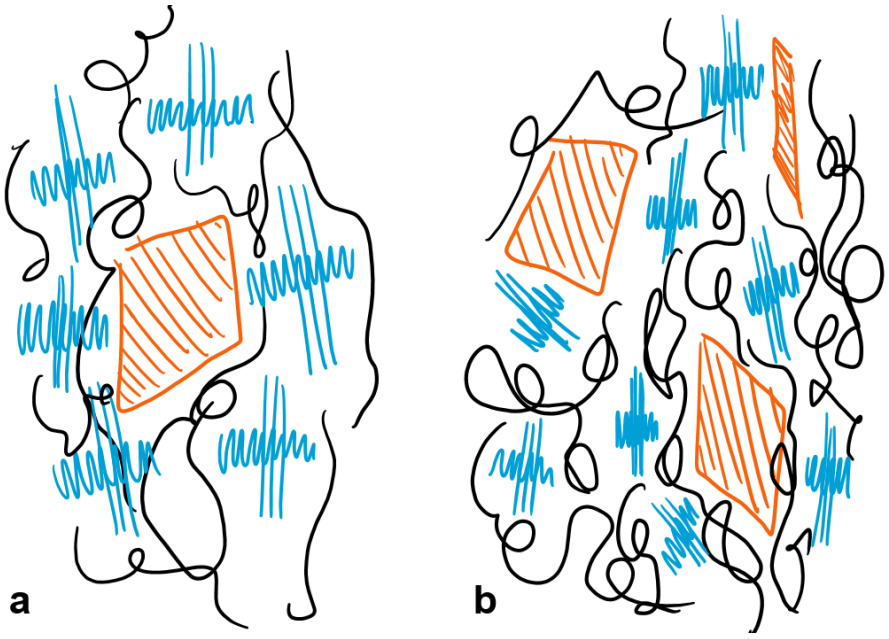

***Figure 42**. Sketched representations of the hypothesized UHMWPE/GnP microstructure developed a) below the reinforcing percolation threshold and b) above. Black strokes indicate amorphous UHMWPE chains, blue strokes indicate crystalline UHMWPE featuring folded- and extended-chain lamellae, and orange strokes indicate GnPs*

Micromechanical modeling highlights the complexity of this mechanism and the limitations of existing micromechanical models, which would predict at least some degree of enhancement in a well-dispersed composite such as these [77]. The simplest of models, the rule of mixtures, can be used to establish an upper bound on the performance of the composite because it assumes perfect load transfer efficiency and an entirely even distribution of idealized particles that are perfectly aligned with the tensile axis [242]. The upper-limit elastic modulus of the composite, E_{c1}, can be found using Equation 4.5,

$$E_{c1} = \nu_r E_r + (1 - \nu_m) E_m \tag{4.5}$$

where ν is the volume fraction and the subscripts *r* and *m* refer to the reinforcement and matrix, respectively. The rule of mixtures can also be used to set a lower limit expectation for these composites by assuming that the same idealized particles are oriented entirely transverse to the tensile axis. The lower-limit elastic modulus of the composite, E_{c2}, can be found using Equation 4.6,

$$E_{c2} = \left(\frac{\nu_r}{E_r} + \frac{1 - \nu_r}{E_m}\right)^{-1} \tag{4.5}$$

Conspicuously missing is any consideration of the geometry of the particles, and a more practical distribution of particle orientation should be applied for a more realistic prediction. A simple approach to making these considerations is assuming that the particles are thin rectangular plates. Thus, a modified Halpin-Tsai model [243] can be applied to predict the elastic modulus of the composite, E_{cHT}, as shown in Equation 4.6,

$$E_{cHT} = \left(a\left(\frac{1 + \zeta \eta_L \nu_r}{1 - \eta_L \nu_r}\right) + (1 - a)\left(\frac{1 + 2\eta_W \nu_r}{1 - \eta_W \nu_r}\right)\right) E_m \tag{4.6}$$

where a is a constant, and η_L, η_W, and ζ, are given in Equations 4.7 and 4.8:

$$\zeta = \left(\frac{W + L}{t}\right) \tag{4.7}$$

$$\eta_L = \frac{(E_r/E_m) - 1}{(E_r/E_m) + \zeta}\ ,\ \eta_W = \frac{(E_r/E_m) - 1}{(E_r/E_m) + 2} \tag{4.8}$$

W is the width, L is the length, and t is the thickness of the graphene nanoplatelet.

Elastic modulus predictions for the nanocomposites developed in this work were made using both models. The elastic modulus of the neat fibers was used as the matrix modulus, and several assumptions about the GnPs had to be made. In both models, the tensile modulus of the GnPs was assumed to be 1 TPa to provide an upper limit for the properties of these particles [4]. For the modified Halpin-Tsai model, the particles were assumed to be square for simplicity with a side length of 290 nm, which is the mode of the nanoparticle size distribution identified via TEM, Figure 32c. The manufacturer's datasheet notes that the particles are "a few nanometers" thick, so the thickness was assumed to be 3. Finally, a is a constant used to modulate the contributions of the longitudinal and transverse moduli of the composite, and it is commonly assumed to be 3/8 for a 2-dimensionally dispersed fiber reinforcement, 0.184 for 3-dimensionally dispersed fibers, and 0.49 for randomly aligned platelets [244]. Precisely determining the bulk average orientation of the graphene nanoplatelets in the experimental nanocomposite fibers produced in this work would require the use of high-resolution computed tomography that was not available during this study. However, assuming that the particles are as aligned with the fiber axis as the polymer crystallites provides a convenient starting point, so the experimentally determined Herman's orientation factor at each concentration was used for a. The model predictions are shown in Figure 43 alongside the experimental results.

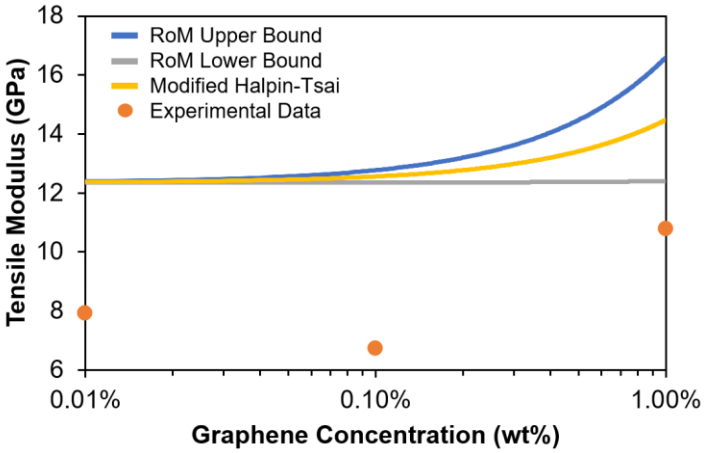

***Figure 43**. Micromechanical modeling predictions of tensile modulus for UHMWPE/GnP fibers spun using 1,4-cineole compared to experimental data. Two models were employed: the rule of mixtures (RoM) and a modified Halpin-Tsai model*

At the upper limit, 1 wt% graphene could increase the tensile modulus of the UHMWPE by 34.4%, which is predicted to be limited to 17.2% when considering the particle geometry and orientation using the modified Halpin-Tsai model. Although the nanocomposites underperform the neat UHMWPE fibers, the improvement in experimental results from 0.01 wt% to 1.0 wt% GnPs, 35.8%, exceeds the total improvement predicted via the rule of mixtures.

While more detailed models include additional parameters for other geometric conditions of the particles, such as waviness [245], or take other approaches, such as shear lag theory [77], no micromechanical models would have predicted the decrement in performance observed in this work. The discrepancy arises when the performance of the matrix depends on microstructural development that is affected by the presence of the nanoparticles. It has been shown that UHMWPE can be reinforced with unmodified GnPs in undrawn formats such as selective laser sintering [246,247] where crystalline orientation is low and crystalline mesostructure development is not a feature of the manufacturing process. However, in other highly drawn formats, such as films, unmodified GnPs have a negative impact on mechanical properties much like what was observed in the present work [233]. Unmodified GnPs are relegated to weak CH-π bonding with

the linear polyethylene chains limiting load transfer [248,249]. At low concentrations, the orientation of the load bearing crystallites and their crucial tie molecule interconnections are disrupted by the presence of these poorly adhered particles due to significantly lower chain mobility at the particle interface [250,251]. At higher GnP loading, this effect becomes an "advantage" as the polymer molecules are limited to a degree that renders greater integration of the nanoparticles into the molecular structure. However, UHMWPE is a composite unto itself wherein folded- and extended-chain crystalline regions reinforce an amorphous matrix [252], and the reduction of the reinforcing crystalline phase overcomes the benefit of the nanoparticle reinforcement. Consequently, tailoring the GnP/UHMWPE interface via functionalization or other means is paramount for mechanical property enhancement in highly drawn UHMWPE formats. Furthermore, the use of higher aspect ratio nanofillers that impede polymer chain mobility less, such as carbon nanotubes [253], may offer advantages by allowing for greater alignment of the polymer molecules during drawing consequently allowing greater strain-induced crystallization.

4. Conclusion

In this study, 1,4-cineole was investigated as a bio-derived alternative to the petrochemical solvents typically used for graphene dispersion and UHMWPE fiber gel spinning. Dispersions of commercially produced GnPs in 1,4-cineole showed exceptional stability compared to other solvents used for UHMWPE spinning, and its viscosity and surface tension properties were presented for the first time in literature. This bio-derived solvent met only one of three criteria conventionally used to predict graphene dispersion stability, so potential molecular interactions explaining this phenomenon were proposed based on literature review. TEM and Raman spectroscopy were used to show that the high shear mixing and tip-probe ultrasonication dispersion

method resulted in sub-micron lateral size GnPs with intact graphene lattices and a minimal increase in disorder.

UHMWPE fiber gel spinning at a commercially relevant concentration of 3 wt% UHMWPE in the 1,4-cineole solution was successfully completed with dry extraction of the spin solvent in air, and the spun fiber was continuously hot drawn at a ratio of 5:1. The fibers exhibited an oblong profile with short lobes and fully densified cross section. The microstructure and mechanical properties were commensurate with those spun using other solvents and drawn to the same degree. UHMWPE/GnP nanocomposite fibers were formed with the GnP concentration varied across three decades, from 0.01 wt% to 1 wt%, to search for an optimal range for mechanical property reinforcement and study its effect on microstructural evolution in the fibers. The nanocomposite fibers' morphology was like their neat counterparts, and AFM was used to show that the GnPs were well dispersed in the polymer matrix.

The addition of GnPs significantly reduced mechanical properties at low concentrations (0.01 and 0.1 wt%) but had little to no effect on the fiber microstructure. The particles act as point defects at these concentrations, due to poor interfacial adhesion, disrupting the load transfer between the load bearing PE crystallites. However, at 1 wt%, the mechanical properties increased significantly compared to the lower concentration regimes. Paradoxically, at this concentration the particles limited the axial and lateral crystallite growth as well as crystallite orientation typically induced during drawing, which is crucial to the development of high mechanical properties. This indicates that a percolation threshold is reached in the 1 wt% decade whereby a network effect takes hold and reinforcement is realized. However, this reinforcement is insufficient to surpass the properties of the neat fibers. This result shows that the 1 wt% decade may offer significant mechanical property enhancement if greater UHMWPE/GnP interfacial adhesion can be realized.

Chapter 5. Concluding Remarks and Recommendations

1. Summary

UHMWPE fiber is an advanced high-performance material used in myriad applications ranging from bulletproof vests [14] to medical implants [15] to offshore wind turbine mooring ropes [19]. It can be converted into carbon fibers for or used directly in in lightweight fiber-reinforced polymer-matrix composites [17,112]. Polymer composites possess low density and high-performance mechanical properties due to the low-density matrix and reinforcement materials used to make them. The discovery of carbon nanoparticles with outstanding mechanical properties in the past thirty years has generated significant interest in forming nanoparticle-reinforced composites for the same purpose as fiber-reinforced composites. With looming and growing challenges due to climate change, such lightweight and high-performance materials will be crucial to improving the energy efficiency and sustainability of human mobility. However, replacing metals with composites is not a complete solution due to the expensive and environmentally unfriendly nature of producing UHMWPE and carbon fibers as well as nanoparticles. Contemporary carbon fiber, UHWMPE fiber, and graphene nanoparticle production requires extensive use of non-renewable organic solvents that are harmful to human health and the environment. Furthermore, UHMWPE fibers are difficult or impossible to recycle. Through this dissertation I aimed to tackle these challenges by replacing UHMWPE fiber spin solvents with sustainable alternatives, expanding the performance envelope of UHMWPE fiber through nanoparticle reinforcement, and converting UHMWPE fibers into carbon fibers as a method of reducing carbon fiber production cost or valorizing UHMWPE fiber waste. In so doing, new understandings of the process-structure-property relationships underlying the formation of UHMWPE fibers using bio-derived solvents, the interaction of UHMWPE microstructure with

graphene nanoparticles, and the crucial processing parameters for carbon fiber conversion from PE have been generated. These contributions to the fields of UHMWPE fibers, polymer nanocomposites, and carbon fibers are summarized here.

2. Key Contributions and Broader Impacts

2.1. Polyethylene-Derived Carbon Fibers

The search for a cost-reducing alternative precursor material for carbon fiber production continues, but now with new knowledge regarding one of the leading candidates: PE. In Chapter 2, the hypothesis that the highly aligned microstructure of UHMWPE may lead to greater mechanical properties in PE-derived carbon fibers was tested by searching for the optimal tension applied during the sulfonation stabilization of the fibers prior to carbonization. It had previously been acknowledged that optimizing tension during this phase of conversion may enhance carbon fiber mechanical properties [110,111,113], but no test of that hypothesis had been published. Indeed, the high performance of UHMWPE fibers enabled the application of greater sulfonation tension than had been applied in previous works, which resulted in significantly reduced kink-banding, fewer defects, and greater mechanical properties. The results highlighted that tension during sulfonation stabilization should be maximized for maximal mechanical properties, and the increased tension did not hinder the stabilization process. Microstructural analysis revealed that increasing stabilization tension increased the size and alignment of the crystallites in the carbon fiber microstructure. However, this work also showed that the high alignment and crystallinity of UHMWPE is not an advantage in the carbon fiber conversion process as the resultant carbon fibers significantly underperformed other PE-derived carbon fibers [118] and even the UHMWPE precursor fibers themselves. Disproving this hypothesis winnows the field of PE grades as alternative precursors for high-performance carbon fibers, and both findings will accelerate the

development of alternative precursors for carbon fiber development by narrowing the fields of precursor materials and processing parameters. Additionally, the UHMWPE-derived carbon fibers produced in this work presented an interesting opportunity. The fibers exhibited multiscale surface features offering high surface area, which is a key characteristic of activated carbon fibers that can be used for air and water purification. Upcycling end-of-life UHMWPE fibers into activated carbon fibers can reduce landfill while creating materials that can capture greenhouse gasses and remove contaminants from water.

2.2. Sustainable UHMWPE Gel Spinning

Much of UHMWPE fiber research in recent decades has focused on the optimization of the spinning and drawing processes to maximize mechanical properties using conventional petrochemical solvents, but only a handful of studies have probed the use of renewable spin solvent alternatives. Only two previous studies explored dry extraction gel spinning of UHMWPE fibers using only one naturally derived solvent, orange terpenes, and the results lacked a comprehensive investigation of the properties of the fibers from the nano- to the macro-scale [90,91]. In Chapter 3, this gap was filled by showing that UHMWPE fibers spun using orange terpenes possess microstructural characteristics and mechanical properties consistent with UHMWPE fibers spun using conventional solvents and drawn to a similar degree. This shows that the fibers have the potential to meet the properties of contemporary commercially produced UHMWPE fibers given parametric optimization of the processing parameters and lays a foundation for realizing this by detailing the evolution of the morphology, microstructure, and properties from as-spun to drawn fibers. Achieving this may significantly reduce the environmental impact of UHMWPE fiber gel spinning by replacing petrochemical solvents with renewable bio-derived solvents produced from fruit peel waste.

In Chapter 4, several other terpenes were identified as potential alternative bio-derived spin solvents for UHMWPE using Hansen solubility parameters (HSP), and one, 1,4-cineole, was successfully demonstrated while the others remain open opportunities. The mechanical properties of the resulting fibers approached but fell short of those of the fibers spun using orange terpenes. The fibers were found to retain some residue after dry extraction, potentially due to impurities in the 1,4-cineole grade selected for the study, that evaporated away at temperatures above 180°C. This residue intercalated into the crystalline structure of the fibers, likely resulting in the depreciated mechanical properties relative to the orange terpenes-spun fibers, which had not been previously published. The profile geometry of the orange terpenes-spun and 1,4-cineole-spun fibers varied greatly from each other and relative to decalin-spun UHMWPE fibers showing that the morphology formation during dry extraction gel spinning process is heavily influenced by the solvent despite all sharing similar characteristics. This highlights that much remain to be learned of bio-derived dry-extraction solvents for UHMWPE gel spinning and that there may be opportunities lying in other terpenes, such as pinene.

2.3. Polymer Nanocomposites

1,4-Cineole was chosen as the spin solvent in Chapter 4 because, of thirty bio-derived candidates, it was the option capable of dissolving UHMWPE with the greatest likelihood of dispersing GnPs well, according to HSP. The long-term stability of 1,4-cineole/GnP suspensions exceeded expectations despite failing two of the three criteria most commonly used to predict the suitability of a solvent for exfoliating and dispersing graphene, HSP and surface energy [68]. The viscosity and surface energy of 1,4-cineole had not been published before this work and will provide researchers and engineers with crucial data for all areas of interest for 1,4-cineole, such as conversion into a sustainable alternative to jet fuel [254]. Furthermore, this result challenges

conventional approaches to selecting solvents for graphene dispersions and emphasizes molecular dynamics driven understandings of the interaction between the solvent and nanoparticle. Shifting focus towards using these tools may identify new suitable solvents previously eschewed by the conventional evaluation framework.

Ultrasonic dissolution of UHMWPE powder into 1,4-cineole/GnP suspension resulted in a semi-dilute solution that could be gel spun into UHMWPE/GnP fibers. GnP concentration was varied across four decades from 0.01 wt% to 10 wt% GnP, and the 1 wt% regime was identified as the upper limit for fiber spinning because phase separation at 10 wt% prevented the continuous uptake of fibers with consistent dimensions. It was shown that the ultrasonic dissolution method maintained the dispersion of the GnPs from the suspension to the polymer solution, and then to the gel fibers thereby overcoming one of the greatest challenges in polymer nanocomposite formation: nanoparticle agglomeration [70]. Despite being well dispersed, the nanocomposite fibers underperformed the GnP-free control samples significantly at 0.01 wt% and 0.1 wt% GnP. Microstructural analysis revealed that poor interfacial adhesion between the particles and UHMWPE matrix resulted in the GnPs acting only as point defects without affecting the microstructure of the polymer fibers at low concentration resulting in damaging effects on the mechanical properties of the fibers. However, at 1 wt% GnP a percolation threshold was surpassed, and the nanoparticles formed a reinforcing network that restored some of the mechanical properties of the fibers despite hindering the movement of the polymer chains enough to impede crystallite growth and orientation. This result challenges contemporary micromechanical modeling methods that would otherwise predict an improvement in the mechanical properties of a well-dispersed nanocomposite such as these and emphasizes the importance of the nanoparticle/matrix interface. Shifting research focus towards interfacial tailoring of GnPs to UHMWPE as a result of this work

will accelerate the development of high-performance and multifunctional UHMWPE nanocomposite fibers.

3. Recommendations for Future Work

The ultimate result of this dissertation is the creation of a foundation for improving the performance and sustainability of UHMWPE fibers across its lifecycle. The results of each chapter of this dissertation present opportunities for further exploration on their own path, and cross-cutting investigations integrating these findings arise as well.

3.1. Sustainable UHMWPE Gel Spinning

An immediate next step for gel spinning UHMWPE fibers is the parametric optimization of the gel spinning and drawing process using orange terpenes as the spin solvent to realize the potential demonstrated in Chapter 3. This may begin with rheological analysis of the UHMWPE/orange terpenes solution to enable modeling and optimization of the flow conditions in the spinning nozzle. Few publications discuss the nozzle geometry in great detail let alone probe its effect on the flow characteristics and resulting fiber structure. Such explorations are crucial to understanding the development of the structure and properties of other spun fibers, such as mesophase pitch [255,256]. Establishing a relationship between the flow conditions in the spinning nozzle and the microstructure development thereafter may enable greater control of crystallite development towards compositions that encourage extended-chain crystal growth during drawing thereby improving mechanical properties. Next, analyzing the gelation and crystallization kinetics of the UHMWPE/orange terpenes solution will inform everything from the extrusion temperature to the spin line configuration (air gap length, coagulation bath design, etc) [183].

As shown in Chapter 4, however, many bio-derived solvents could be used for UHMWPE gel spinning, and some may offer new opportunities. For example, pinene was found to have a Hansen

relative energy difference with UHMWPE significantly lower than that of d-limonene (the primary component of orange terpenes), which implies greater solubility. Pinene may enable the use of greater concentrations of UHMWPE, which would improve throughput and consequently the sustainability of the method by reducing total solvent volume required for processing. The thirty bio-derived solvents reviewed for Hansen solubility parameters in Chapter 4 represent a drop in the bucket of terpenes and other bio-solvents that could be useful for UHMWPE fiber spinning, so broader study may uncover new opportunities. One crucial characteristic to screen for is the α_c relaxation rate. Faster α_c relaxation indicates greater crystalline chain mobility that results in greater crystallinity and drawability of the fibers [257].

3.2. UHMWPE Nanocomposite Modeling

A major outcome of Chapter 4 is that more needs to be understood about the interaction of nanoparticles and UHMWPE crystallites to be able to predict the properties of UHMWPE nanocomposites. This will require the application of molecular dynamics simulation or advanced micromechanical models. The former case has been well applied in other polymer nanocomposites [64] and used to understand interchain behavior within UHMWPE [258]. In the latter case, recent work has revealed the relationship between the various phases in UHMWPE and the axial and transverse properties of UHMWPE fibers [252]. Extending these works to UHMWPE/GnP nanocomposites will enhance our understanding of the defective nature of the nanoparticles at low concentration and network effect induced at 1 wt% GnP concentration. Such models will reveal insights on the effects of the particle geometry in the matrix, which may indicate greater potential in other nanoparticle morphologies such as carbon nanotubes.

3.3. PE-derived Carbon Fibers and Activated Carbon Fibers

The results of Chapter 2 make a strong case against the pursuit of converting commercially-produced UHMWPE fibers into carbon fibers. The carbon fibers failed to exceed the properties of the precursor due to multiscale flaws and poor development of crystallographic structure and order in the carbon fibers. Furthermore, the sulfonation stabilization process takes significantly longer than for other grades of polyethylene due to the slow diffusion of sulfuric acid into the fibers due to its high crystallinity. Finally, commercial production of UHMWPE is expensive due to the gel spinning process and multiple drawing/conditioning steps required to achieve the high crystallinity and order that gives them their impressive mechanical properties. However, the bio-solvent spun fibers produced in Chapters 3 and 4 do not suffer these conditions and may offer some unique advantages. In both cases, the fibers were drawn to fine size, less than 2 dtex for 5:1 drawn orange terpenes-spun fibers and 5:1 drawn 1 wt% GnP 1,4-cineole spun fibers. While appreciable crystalline microstructure was developed, it is significantly lower than that found for the much more highly drawn commercial fibers of the same linear density, which should result in significantly lower stabilization time. Additionally, the flat profile observed in the orange terpenes-spun UHMWPE fibers reduces the distance from the surface to the center of the fiber, which may further reduce stabilization time. Combining these factors with boron catalyzation to induce graphitic structure formation during PE-carbon fiber conversion [118] may open new doors to using this material as a more environmentally friendly precursor for high-performance carbon fiber production. Furthermore, the results of Chapter 4 indicate that graphene nanoparticles inhibit the motion of UHMWPE chains. While this presented a challenge for developing high-performance UHMWPE fibers, it may also present an opportunity for UHMWPE-derived carbon fibers by impeding the polymer molecule rearrangement during the chemical shrinkage phase of

sulfonation. Understanding the relationship between the linear shrinkage observed in this work and the still unknown volumetric effects during this process will be a core component of understanding the mechanism underlying this process.

The factors that make UHMWPE fibers difficult to melt spin also make UHMWPE difficult to recycle like other thermoplastics. One pathway may lie in upcycling waste UHMWPE fibers into activated carbon fibers. In Chapter 2, it was shown via SEM that UHMWPE-derived carbon fibers exhibited high surface area due to the expansion of the microfibrillar structure of the fibers, which is a desirable quality for effective activated carbon fibers. The activation of carbon materials for adsorption is commonly accomplished mechanically using high temperature steam or carbon dioxide or chemically via nitric acid, sulfuric acid, zinc oxide, or sodium hydroxide exposure [259,260]. A major challenge of this application is the state of the UHMWPE fibers as received at the end of life. As shown in Chapter 2, tension is crucial to maintaining the fibrous morphology of the fibers, and applying tension to recycled fibers may not be possible if they are not continuous. This may not be a problem in the case of activating this material since structural properties are not necessary in all applications for their main application as an adsorbent.

Bibliography

[1] Fact Sheet Climate Change, in: United Nations Sustain. Transp. Conf., Beijing, 2018.

[2] Fast Facts: U.S. Transportation Sector Greenhous Gas Emissions 1990-2022, 2024.

[3] P.K. Mallick, Fiber-Reinforced Composites: Materials, Manufacturing, and Design, Third Edition, 3rd ed., CRC Press, Boca Raton, FL, 2007. https://doi.org/10.1201/9781420005981.

[4] C. Lee, X. Wei, J.W. Kysar, J. Hone, Measurement of the elastic properties and intrinsic strength of monolayer graphene, Science. 321 (2008) 385–388. https://doi.org/10.1126/science.1157996.

[5] X. Du, I. Skachko, A. Barker, E.Y. Andrei, Approaching ballistic transport in suspended graphene, Nature Nanotech. 3 (2008) 491–495. https://doi.org/10.1038/nnano.2008.199.

[6] A.A. Balandin, S. Ghosh, W. Bao, I. Calizo, D. Teweldebrhan, F. Miao, C.N. Lau, Superior thermal conductivity of single-layer graphene, Nano Lett. 8 (2008) 902–907. https://doi.org/10.1021/nl0731872.

[7] G.M. Pinto, J.M. O Cremonezzi, H. Ribeiro, R.J. E Andrade, N.R. Demarquette, G.J. M Fechine, From two-dimensional materials to polymer nanocomposites with emerging multifunctional applications: A critical review, Polym. Compos. 44 (2023) 1438–1470. https://doi.org/10.1002/pc.27213.

[8] C. Zhao, Y. Li, Y. Liu, H. Xie, W. Yu, A critical review of the preparation strategies of thermally conductive and electrically insulating polymeric materials and their applications in heat dissipation of electronic devices, Adv. Compos. Hybrid Mater. 6 (2022) 1–26. https://doi.org/10.1007/S42114-022-00584-2.

[9] Polyethylene (PE) Plastic: Properties, Uses & Application, (n.d.). https://omnexus.specialchem.com/selection-guide/polyethylene-plastic (accessed May 18, 2021).

[10] T. Okamura, Polyethylene (PE; Low Density and High Density), in: S. Kobayashi, K. Müllen (Eds.), Encycl. Polym. Nanomater., Springer Berlin Heidelberg, Berlin, Heidelberg, 2015: pp. 1826–1829. https://doi.org/10.1007/978-3-642-29648-2_252.

[11] C. Roiron, E. Lainé, J.-C. Grandidier, N. Garois, C. Vix-Guterl, A review of the mechanical and physical properties of polyethylene fibers, Textiles. 1 (2021) 86–151. https://doi.org/10.3390/textiles1010006.

[12] L.C. Wang, M.K. Harvey, J.C. Ng, U. Scheunemann, Ultra-high molecular weight polyethylene (UHMW-PE) and its application in microporous separators for lead/acid batteries, J. Power Sources. 73 (1998) 74–77. https://doi.org/10.1016/S0378-7753(98)00023-8.

[13] R. Li, P. Gao, Nanoporous UHMWPE membrane separators for safer and high-power-density rechargeable batteries, Glob. Challenges. 1 (2017) 1700020. https://doi.org/10.1002/gch2.201700020.

[14] H. Van Der Werff, U. Heisserer, High-performance ballistic fibers: Ultra-high molecular weight polyethylene (UHMWPE), in: X. Chen (Ed.), Adv. Fibrous Compos. Mater. Ballist. Prot., Woodhead Publishing, 2016: pp. 71–107. https://doi.org/10.1016/B978-1-78242-461-1.00003-0.

[15] N.A. Patil, J. Njuguna, B. Kandasubramanian, UHMWPE for biomedical applications: Performance and functionalization, Eur. Polym. J. 125 (2020) 109529. https://doi.org/10.1016/J.EURPOLYMJ.2020.109529.

[16] J.T. Yeh, S.C. Lin, C.W. Tu, K.H. Hsie, F.C. Chang, Investigation of the drawing mechanism of UHMWPE fibers, J. Mater. Sci. 43 (2008) 4892–4900. https://doi.org/10.1007/s10853-008-2711-1.

[17] S. Chhetri, H. Bougherara, A comprehensive review on surface modification of UHMWPE fiber and interfacial properties, Compos. Part A. (2020) 106146. https://doi.org/10.1016/j.compositesa.2020.106146.

[18] A.A. Candadai, E.J. Nadler, J.S. Burke, J.A. Weibel, A.M. Marconnet, Thermal and mechanical characterization of high performance polymer fabrics for applications in wearable devices, Sci. Rep. 11 (2021) 1–11. https://doi.org/10.1038/s41598-021-87957-7.

[19] M.P. Vlasblom, J. Boesten, S. Leite, P. Davies, Development of HMPE fiber for permanent deepwater offshore mooring, in: Offshore Technol. Conf. Proc., Houston, TX, 2012: pp. 1944–1958. https://doi.org/10.4043/23333-MS.

[20] P. Smith, P.J. Lemstra, Ultra-high-strength polyethylene filaments by solution spinning/drawing, J. Mater. Sci. 15 (1980) 505–514. https://doi.org/10.1007/BF02396802.

[21] P.J. Lemstra, Chapter 1: High-performance polyethylene fibers, Adv. Ind. Eng. Polym. Res. 5 (2022) 49–59. https://doi.org/10.1016/j.aiepr.2022.03.001.

[22] X. Fang, T. Wyatt, Y. Hong, D. Yao, Gel spinning of UHMWPE fibers with polybutene as a new spin solvent, Polym. Eng. Sci. 56 (2016) 697–706. https://doi.org/10.1002/pen.24296.

[23] J. Smook, J. Pennings, Influence of draw ratio on morphological and structural changes in hot-drawing of UHMW polyethylene fibres as revealed by DSC, Colloid Polym. Sci. 262 (1984) 712–722. https://doi.org/10.1007/BF01451543.

[24] H.K. I Jen, W.N. Che, Y. Ing Chang, Gelation behaviour of UHMWPE/camphene, J. Mater. Sci. 32 (1997) 3607–3611. https://doi.org/10.1023/A:1018674212213.

[25] A.W. Rajput, A.U. Aleem, F.A. Arain, An Environmentally friendly process for the preparation of UHMWPE as-spun fibres, Int. J. Polym. Sci. (2014) 1–5. https://doi.org/10.1155/2014/480149.

[26] A. Ragothaman, W.A. Anderson, Air quality impacts of petroleum refining and petrochemical industries, Environments. 4 (2017) 66. https://doi.org/10.3390/environments4030066.

[27] A. Sharma, P. Sharma, A. Sharma, R. Tyagi, A. Dixit, Hazardous effects of petrochemical industries: A review, Recent Adv Petrochem Sci. 3 (2017) 25–27. https://doi.org/10.19080/RAPSCI.2017.03.555607.

[28] C. Capello, G. Wernet, J. Sutter, S. Hellweg, K. Hungerbühler, A comprehensive environmental assessment of petrochemical solvent production, Int. J. Life Cycle Assess. 14 (2009) 467–479. https://doi.org/10.1007/s11367-009-0094-4.

[29] E. Fitzer, Carbon Fibers - Present State and Future Expectations, in: J.L. Figueiredo, C.A. Bernardo, R.T.K. Baker, K.J. Hüttinger (Eds.), Carbon Fibers Filaments Compos., Springer Dordrecht, Alvor, Portugal, 1990: pp. 3–43. https://doi.org/10.1007/978-94-015-6847.

[30] D.D.L. Chung, Carbon Fiber Composites, Elsevier, 1994. https://doi.org/10.1016/C2009-0-26078-8.

[31] X. Huang, Fabrication and properties of carbon fibers, Materials (Basel). 2 (2009) 2369–2403. https://doi.org/10.3390/ma2042369.

[32] M. Minus, S. Kumar, The processing, properties, and structure of carbon fibers, JOM. 57 (2005) 52–58. https://doi.org/10.1007/s11837-005-0217-8.

[33] L.H. Peebles, Carbon Fibers from Acrylic Precursors, in: Carbon Fibers Form. Struct. Prop., CRC Press Inc., Boca Raton, FL, 1995: pp. 7–27.

[34] M.L. Minus, S. Kumar, The processing, properties, and structure of carbon fibers, JOM. 57 (2005) 52–58. https://doi.org/10.1007/s11837-005-0217-8.

[35] L. Fischer, W. Ruland, The influence of graphitization on the mechanical properties of carbon fibers, Colloid Polym. Sci. 258 (1980) 917–922.

[36] E. Fitzer, PAN-based carbon fibers-present state and trend of the technology from the viewpoint of possibilities and limits to influence and to control the fiber properties by the process parameters, Carbon. 27 (1989) 621–645. https://doi.org/10.1016/0008-6223(89)90197-8.

[37] S.K. Nataraj, K.S. Yang, T.M. Aminabhavi, Polyacrylonitrile-based nanofibers - A state-of-the-art review, Prog. Polym. Sci. 37 (2012) 487–513. https://doi.org/10.1016/j.progpolymsci.2011.07.001.

[38] D.D.L. Chung, Processing of Carbon Fibers, in: Carbon Fiber Compos., 1st ed., Butterworth-Heinemann, Boston, 1994: pp. 13–53. https://doi.org/10.1016/b978-0-08-050073-7.50006-3.

[39] K. Sada, K. Kokado, Y. Furukawa, Polyacrylonitrile (PAN), in: Encycl. Polym. Nanomater., Springer Berlin Heidelberg, 2015: pp. 1745–1750. https://doi.org/10.1007/978-3-642-29648-2_249.

[40] G. Konstantopoulos, S. Soulis, D. Dragatogiannis, C. Charitidis, Introduction of a methodology to enhance the stabilization process of PAN fibers by modeling and advanced characterization, Materials (Basel). 13 (2020) 2749. https://doi.org/10.3390/ma13122749.

[41] E. Frank, L.M. Steudle, D. Ingildeev, J.M. Spörl, M.R. Buchmeiser, Carbon fibers: Precursor systems, processing, structure, and properties, Angew. Chemie - Int. Ed. 53 (2014) 5262–5298. https://doi.org/10.1002/anie.201306129.

[42] D. Choi, H.-S. Kil, S. Lee, Fabrication of low-cost carbon fibers using economical precursors and advanced processing technologies, Carbon. 142 (2019) 610–649. https://doi.org/10.1016/j.carbon.2018.10.028.

[43] H. Khayyam, R.N. Jazar, S. Nunna, G. Golkarnarenji, K. Badii, S.M. Fakhrhoseini, S. Kumar, M. Naebe, PAN precursor fabrication, applications and thermal stabilization process in carbon fiber production: Experimental and mathematical modelling, Prog. Mater. Sci. 107 (2020). https://doi.org/10.1016/j.pmatsci.2019.100575.

[44] D.D. Edie, The effect of processing on the structure and properties of carbon fibers, Carbon. 36 (1998) 345–362. https://doi.org/10.1016/S0008-6223(97)00185-1.

[45] J. Chen, C.G. Wang, X.G. Dong, H.Z. Liu, Study on the coagulation mechanism of wet-spinning PAN fibers, J. Polym. Res. 13 (2006) 515–519. https://doi.org/10.1007/s10965-006-9075-5.

[46] E. Morris, M. Weisenberger, G. Rice, Properties of PAN fibers solution spun into a chilled coagulation bath at high solvent compositions, Fibers. 3 (2015) 560–574. https://doi.org/10.3390/fib3040560.

[47] S. Edrington, The Limits & Effects of Draw on Properties and Morphology of PAN-Based Precursor and the Resultant Carbon Fibers, University of Kentucky, 2017. https://doi.org/10.13023/ETD.2017.165.

[48] B.A. Newcomb, Processing, structure, and properties of carbon fibers, Compos. Part A Appl. Sci. Manuf. 91 (2016) 262–282. https://doi.org/10.1016/j.compositesa.2016.10.018.

[49] Y. Imura, R.M.C. Hogan, M. Jaffe, Dry spinning of synthetic polymer fibers, in: D. Zhang (Ed.), Adv. Filam. Yarn Spinn. Text. Polym., Woodhead Publishing, 2014: pp. 187–202. https://doi.org/10.1533/9780857099174.2.187.

[50] K.R. Brown, T.M. Harrell, L. Skrzypczak, A. Scherschel, H.F. Wu, X. Li, Carbon fibers derived from commodity polymers: A review, Carbon. 196 (2022) 422–439. https://doi.org/10.1016/J.CARBON.2022.05.005.

[51] J.-B. Donnet, ed., Carbon Black : Science and Technology, Second Edition, 2nd ed., Routledge, 1993. https://doi.org/10.1201/9781315138763.

[52] Y.W. Sun, D.G. Papageorgiou, C.J. Humphreys, D.J. Dunstan, P. Puech, J.E. Proctor, C. Bousige, D. Machon, A. San-Miguel, Mechanical properties of graphene, Appl. Phys. Rev. 8 (2021) 021310. https://doi.org/10.1063/5.0040578.

[53] M.-F. Yu, Fundamental mechanical properties of carbon nanotubes: current understanding and the related experimental studies, J. Eng. Mater. Technol. 126 (2004) 271–278. https://doi.org/10.1115/1.1755245.

[54] V.N. Popov, Carbon nanotubes: properties and application, Mater. Sci. Eng. R Reports. 43 (2004) 61–102. https://doi.org/10.1016/j.mser.2003.10.001.

[55] J.S. Bunch, S.S. Verbridge, J.S. Alden, A.M. Van Der Zande, J.M. Parpia, H.G. Craighead, P.L. McEuen, Impermeable atomic membranes from graphene sheets, Nano Lett. 8 (2008) 2458–2462. https://doi.org/10.1021/nl801457b.

[56] W.U. Khan, M.K. Bahar, H. Mazhar, F. Shehzad, M.A. Al-Harthi, Recent advances in nitride-filled polyethylene nanocomposites, Adv. Compos. Hybrid Mater. 6 (2023) 27. https://doi.org/10.1007/s42114-023-00802-5.

[57] K.S. Novoselov, D. Jiang, F. Schedin, T.J. Booth, V. V. Khotkevich, S. V. Morozov, A.K. Geim, Two-dimensional atomic crystals, Proc. Natl. Acad. Sci. U. S. A. 102 (2005) 10451–10453. https://doi.org/10.1073/PNAS.0502848102.

[58] K.S. Novoselov, A.K. Geim, S. V. Morozov, D. Jiang, Y. Zhang, S. V. Dubonos, I. V. Grigorieva, A.A. Firsov, Electric field in atomically thin carbon films, Science. 306 (2004) 666–669. https://doi.org/10.1126/SCIENCE.1102896.

[59] C. Lee, J.Y. Kim, S. Bae, K.S. Kim, B.H. Hong, E.J. Choi, Optical response of large scale single layer graphene, Appl. Phys. Lett. 98 (2011). https://doi.org/10.1063/1.3555425/935870.

[60] T.-Y. Liu, Y.-W. Cheng, S. Jung Lee, S. Jeong Yoon, I.-Y. Jeon, Graphene/polymer nanocomposites: preparation, mechanical properties, and application, Polymers (Basel). 14 (2022) 4733. https://doi.org/10.3390/polym14214733.

[61] X.X. Wei, C. Pei, J.H. Zhu, Towards the large-scale application of graphene-modified cement-based composites: A comprehensive review, Constr. Build. Mater. 421 (2024) 135632. https://doi.org/10.1016/J.CONBUILDMAT.2024.135632.

[62] T. Zhou, M. Lei, J. Xu, Recent progress in the development and properties of aluminum matrix composites reinforced with graphene: A review, Mater. Today Sustain. 25 (2024) 100674. https://doi.org/10.1016/J.MTSUST.2024.100674.

[63] Y. Li, P. Li, A review: progress in regulating the ductility loss of graphene-reinforced titanium matrix materials, Crit. Rev. Solid State Mater. Sci. (2024). https://doi.org/10.1080/10408436.2024.2314570.

[64] Z. Gao, J. Zhu, S. Rajabpour, K. Joshi, M. Kowalik, B. Croom, Y. Schwab, L. Zhang, C. Bumgardner, K.. Brown, D. Burden, J.W. Klett, A.C.T. van Duin, L.V. Zhigilei, X. Li, Graphene reinforced carbon fibers, Sci. Adv. 6 (2020). https://doi.org/10.1126/sciadv.aaz4191.

[65] K.R. Paton, E. Varrla, C. Backes, R.J. Smith, U. Khan, A. O'Neill, C. Boland, M. Lotya, O.M. Istrate, P. King, T. Higgins, S. Barwich, P. May, P. Puczkarski, I. Ahmed, M. Moebius, H. Pettersson, E. Long, J. Coelho, S.E. O'Brien, E.K. McGuire, B.M. Sanchez, G.S. Duesberg, N. McEvoy, T.J. Pennycook, C. Downing, A. Crossley, V. Nicolosi, J.N. Coleman, Scalable production of large quantities of defect-free few-layer graphene by shear exfoliation in liquids, Nat. Mater. 13 (2014) 624–630. https://doi.org/10.1038/nmat3944.

[66] A. V. Tyurnina, I. Tzanakis, J. Morton, J. Mi, K. Porfyrakis, B.M. Maciejewska, N. Grobert, D.G. Eskin, Ultrasonic exfoliation of graphene in water: A key parameter study, Carbon. 168 (2020) 737–747. https://doi.org/10.1016/J.CARBON.2020.06.029.

[67] W. Du, X. Jiang, L. Zhu, From graphite to graphene: direct liquid-phase exfoliation of graphite to produce single- and few-layered pristine graphene, J. Mater. Chem. A. 1 (2013) 10592. https://doi.org/10.1039/c3ta12212c.

[68] H.J. Salavagione, J. Sherwood, M. De Bruyn, V.L. Budarin, G.J. Ellis, J.H. Clark, P.S. Shuttleworth, Identification of high performance solvents for the sustainable processing of graphene, Green Chem. 19 (2017) 2550–2560. https://doi.org/10.1039/c7gc00112f.

[69] B. Gürünlü, Ç. Taşdelen-Yücedağ, M. Bayramoğlu, Graphene synthesis by ultrasound energy-assisted exfoliation of graphite in various solvents, Crystals. 10 (2020) 1–12. https://doi.org/10.3390/cryst10111037.

[70] R. Atif, F. Inam, Reasons and remedies for the agglomeration of multilayered graphene and carbon nanotubes in polymers, Beilstein J. Nanotechnol. 7 (2016) 1174–1196. https://doi.org/10.3762/bjnano.7.109.

[71] M. Lotya, P.J. King, U. Khan, S. De, J.N. Coleman, High-concentration, surfactant-stabilized graphene dispersions, ACS Nano. 4 (2010) 3155–3162. https://doi.org/10.1021/NN1005304.

[72] S. Lin, C.J. Shih, M.S. Strano, D. Blankschtein, Molecular insights into the surface morphology, layering structure, and aggregation kinetics of surfactant-stabilized graphene dispersions, J. Am. Chem. Soc. 133 (2011) 12810–12823. https://doi.org/10.1021/JA2048013.

[73] A. Liang, X. Jiang, X. Hong, Y. Jiang, Z. Shao, D. Zhu, Recent developments concerning the dispersion methods and mechanisms of graphene, Coatings 2018, Vol. 8, Page 33. 8 (2018) 33. https://doi.org/10.3390/coatings8010033.

[74] Z. Yuan, X. Chen, D. Yu, P. Fernandes, A. Faroughi, L.L. Ferrás, A.M. Afonso, Recent advances in elongational flow dominated polymer processing technologies, Polymers (Basel). 13 (2021) 1792. https://doi.org/10.3390/polym13111792.

[75] C.Y. Liu, A. Ishigami, T. Kurose, H. Ito, Wear resistance of graphene reinforced ultra-high molecular weight polyethylene nanocomposites prepared by octa-screw extrusion process, Compos. Part B Eng. 215 (2021) 108810. https://doi.org/10.1016/j.compositesb.2021.108810.

[76] W. Xu, Y. He, H. Xie, S. Qin, L. Tan, T. Wu, J. Qu, Ultrafast fabrication of graphene-reinforced nanocomposites via synergy of steam explosion and alternating convergent-divergent flow, Small. 17 (2021) 2100017. https://doi.org/10.1002/SMLL.202100017.

[77] R.J. Young, M. Liu, I.A. Kinloch, S. Li, X. Zhao, C. Vallés, D.G. Papageorgiou, The mechanics of reinforcement of polymers by graphene nanoplatelets, Compos. Sci. Technol. 154 (2018) 110–116. https://doi.org/10.1016/J.COMPSCITECH.2017.11.007.

[78] J.L. Apátiga, R.M. Del Castillo, L.F. Del Castillo, A.G. Calles, R. Espejel-Morales, J.F. Favela, V. Compañ, Non-covalent interactions on polymer-graphene nanocomposites and their effects on the electrical conductivity, Polymers (Basel). 13 (2021). https://doi.org/10.3390/POLYM13111714/S1.

[79] H.J. Salavagione, Covalent Graphene-Polymer Nanocomposites, in: A. Tiwari, M. Syväjärvi (Eds.), Graphene Mater. Fundam. Emerg. Appl., Scrivener Publishing LLC, 2015: pp. 101–149. https://doi.org/10.1002/9781119131816.ch4.

[80] G. Marom, H. Daniel Wagner, Should polymer nanocomposites be regarded as molecular composites?, J. Mater. Sci. 52 (2017) 8357–8361. https://doi.org/10.1007/S10853-017-1113-7.

[81] F.G. Calvo-Flores, M.J. Monteagudo-Arrebola, J.A. Dobado, J. Isac-García, Green and bio-based solvents, Top. Curr. Chem. 376 (2018) 40. https://doi.org/10.1007/s41061-018-0191-6.

[82] J.H. Clark, T.J. Farmer, A.J. Hunt, J. Sherwood, Opportunities for bio-based solvents created as petrochemical and fuel products transition towards renewable resources, Int. J. Mol. Sci. 16 (2015) 17101–17159. https://doi.org/10.3390/ijms160817101.

[83] R. Schaller, K. Feldman, P. Smith, T.A. Tervoort, High-performance polyethylene fibers "Al dente": Improved gel-spinning of ultrahigh molecular weight polyethylene using vegetable oils, Macromolecules. 48 (2015) 8877–8884. https://doi.org/10.1021/acs.macromol.5B02211.

[84] B.A.S. Machado, C.G. Pereira, S.B. Nunes, F.F. Padilha, M.A. Umsza-Guez, Supercritical fluid extraction using CO2: Main applications and future perspectives, Sep. Sci. Technol. 48 (2013) 2741–2760. https://doi.org/10.1080/01496395.2013.811422.

[85] J. Zhang, A.J. Busby, C.J. Roberts, X. Chen, M.C. Davies, S.J.B. Tendler, S.M. Howdle, Preparation of a poly(methyl methacrylate)/ultrahigh molecular weight polyethylene blend using supercritical carbon dioxide and the identification of a three-phase structure: An atomic force microscopy study, Macromolecules. 35 (2002) 8869–8877. https://doi.org/10.1021/ma012258v.

[86] Y. Wang, J. Fu, J. Yu, Q. Song, J. Zhu, Y. Wang, Z. Hu, Dissolving of ultra-high molecular weight polyethylene assisted through supercritical carbon dioxide to enhance the mechanical properties of fibers, Adv. Fiber Mater. 4 (2022) 280–292. https://doi.org/10.1007/s42765-021-00107-6.

[87] Y.Y. Wang, J. Fu, Q. Song, J. Yu, Y.Y. Wang, Z. Hu, Regulating the dissolving system of ultra-high molecular weight polyethylene to enhance the high-strength and high-modulus properties of resultant fibers, J. Appl. Polym. Sci. 139 (2022) 14. https://doi.org/10.1002/APP.52653.

[88] Y. Wang, X. Wang, J. Fu, J. Yu, Y. Wang, Z. Hu, Enhanced tensile properties of ultra-high molecular weight polyethylene fibers by solubility improvement with mixed solvents, J. Appl. Polym. Sci. 140 (2023) 1–14. https://doi.org/10.1002/app.53715.

[89] A.W. Rajput, An Investigation into the Production of UHMWPE Fibres and Coatings for Protective Apparel, Ph.D. Dissertation, Heriot-Watt University, 2013. http://hdl.handle.net/10399/2879.

[90] A.W. Rajput, A.U. Aleem, F.A. Arain, An Environmentally friendly process for the preparation of UHMWPE as-spun fibres, Int. J. Polym. Sci. 2014 (2014) 1–5. https://doi.org/10.1155/2014/480149.

[91] A.W. Rajput, U. Ali, B. Zahid, A. Abbas, H. Jamshaid, R.F. Qureshi, Application of Taguchi method to investigate the effect of temperature, heating time, concentration and particle size on improved gel spinning process of UHMWPE, Ind. Textila. 69 (2018) 347–351. https://doi.org/10.35530/it.069.05.1468.

[92] J. Sanes, C. Sánchez, R. Pamies, M.-D.D. Avilés, M.-D.D. Bermúdez, Extrusion of polymer nanocomposites with graphene and graphene derivative nanofillers: an overview of recent developments, Materials (Basel). 13 (2020) 549. https://doi.org/10.3390/ma13030549.

[93] P. Pötschke, T.D. Fornes, D.R. Paul, Rheological behavior of multiwalled carbon nanotube/polycarbonate composites, Polymer (Guildf). 43 (2002) 3247–3255. https://doi.org/10.1016/S0032-3861(02)00151-9.

[94] K. Honaker, F. Vautard, L.T. Drzal, Influence of processing methods on the mechanical and barrier properties of HDPE-GNP nanocomposites, Adv. Compos. Hybrid Mater. 4 (2021) 492–504. https://doi.org/10.1007/S42114-020-00181-1.

[95] L. Zhang, M. Kowalik, Z. Gao, C.M. Ashraf, S. Rajabpour, C. Bumgardner, Y. Schwab, B. Damirchi, J. Zhu, D. Akbarian, J.W. Klett, A.C.T. van Duin, X. Li, Converting PBO fibers into carbon fibers by ultrafast carbonization, Carbon. 159 (2020) 432–442. https://doi.org/10.1016/j.carbon.2019.12.067.

[96] Y. Kawahara, S. Otoyama, K. Yamamoto, H. Wakizaka, Y. Shinahara, H. Hoshiro, N. Ishibashi, N. Iwashita, Direct carbonization of high-performance aromatic polymers and the production of activated carbon fibers, J Text. Sci Eng. 5 (2015) 6. https://doi.org/10.4172/2165-8064.1000219.

[97] J.A. Newell, D.K. Rogers, D.D. Edie, C.C. Fain, Direct carbonization of PBO fiber, Carbon. 32 (1994) 651–658. https://doi.org/10.1016/0008-6223(94)90086-8.

[98] Zylon Fibers, (n.d.). https://polymerdatabase.com/Fibers/PBO.html (accessed August 13, 2021).

[99] E.W. Choe, S.N. Kim, Synthesis, spinning, and fiber mechanical properties of poly(p-phenylenebenzobisoxazole), Macromolecules. 14 (1981) 920–924. https://doi.org/10.1021/MA50005A006.

[100] S. Kumar, S. Warner, D.T. Grubb, W.W. Adams, On the small-angle X-ray scattering of rigid-rod polymer fibres, Polymer (Guildf). 35 (1994) 5408–5412. https://doi.org/10.1016/S0032-3861(05)80003-5.

[101] A.L. Andrady, M.A. Neal, Applications and societal benefits of plastics, Philos. Trans. R. Soc. B Biol. Sci. 364 (2009) 1977–1984. https://doi.org/10.1098/rstb.2008.0304.

[102] R. Geyer, J.R. Jambeck, K.L. Law, Production, use, and fate of all plastics ever made, Sci. Adv. 3 (2017) e1700782. https://doi.org/10.1126/sciadv.1700782.

[103] A. Shozo Horikiri, T. Jiro Iseki, I. Masao Minobe, Process for production of carbon fiber, US Patent 4070446, 1978.

[104] J.P. Penning, R. Lagcher, A.J. Pennings, The effect of diameter on the mechanical properties of amorphous carbon fibres from linear low density polyethylene, Polym. Bull. 25 (1991) 405–412. https://doi.org/10.1007/BF00316913.

[105] J.W. Kim, J.S. Lee, Preparation of carbon fibers from linear low density polyethylene, Carbon. 94 (2015) 524–530. https://doi.org/10.1016/j.carbon.2015.06.074.

[106] A.R. Postema, H. De Groot, A.. Pennings, Amorphous carbon fibres from linear low density polyethylene, J. Mater. Sci. 25 (1990) 4216–4222. https://doi.org/https://doi.org/10.1007/BF00581075.

[107] K.-W. Kim, H.-M. Lee, B.S. Kim, S.-H. Hwang, L.-K. Kwac, K.-H. An, B.-J. Kim, Preparation and thermal properties of polyethylene-based carbonized fibers, Carbon Lett. 16 (2015) 62–66. https://doi.org/10.5714/CL.2015.16.1.062.

[108] G.S. Wortberg, A. De Palmenaer, M. Beckers, G. Seide, T. Gries, Polyethylene-based carbon fibers by the use of sulphonation for stabilization, Fibers. 3 (2015) 373–379. https://doi.org/10.3390/fib3030373.

[109] A. De Palmenaer, G. Wortberg, F. Drissen, G. Seide, T. Gries, Production of polyethylene based carbon fibres, Chem. Eng. Trans. 43 (2015) 1699–1704. https://doi.org/10.3303/CET1543284.

[110] D. Zhang, G.S. Bhat, Carbon fibers from polyethylene-based precursors, Mater. Manuf. Process. 9 (1994) 221–235. https://doi.org/10.1080/10426919408934900.

[111] D. Zhang, Carbon fibers from oriented polyethylene precursors, J. Thermoplast. Compos. Mater. 6 (1993) 38–48. https://doi.org/10.1177/089270579300600104.

[112] T. Röding, J. Langer, T.M. Barbosa, M. Bouhrara, T. Gries, A review of polyethylene-based carbon fiber manufacturing, Appl. Res. (2022). https://doi.org/10.1002/APPL.202100013.

[113] D. Zhang, Q. Sun, Structure and properties development during the conversion of polyethylene precursors to carbon fibers, J. Appl. Polym. Sci. 62 (1996) 367–373. https://doi.org/10.1002/(SICI)1097-4628(19961010)62:2<367::AID-APP11>3.0.CO;2-Z.

[114] J.M. Younker, T. Saito, M.A. Hunt, A.K. Naskar, A. Beste, Pyrolysis pathways of sulfonated polyethylene, an alternative carbon fiber precursor, J. Am. Chem. Soc. 135 (2013) 6130–6141. https://doi.org/10.1021/ja3121845.

[115] B.E. Barton, J. Patton, E. Hukkanen, M. Behr, J.C. Lin, S. Beyer, Y. Zhang, L. Brehm, B. Haskins, B. Bell, B. Gerhart, A. Leugers, M. Bernius, The chemical transformation of hydrocarbons to carbon using SO3 sources, Carbon. 94 (2015) 465–471. https://doi.org/10.1016/J.CARBON.2015.07.029.

[116] M.J. Behr, B.G. Landes, B.E. Barton, M.T. Bernius, G.F. Billovits, E.J. Hukkanen, J.T. Patton, W. Wang, C. Wood, D.T. Keane, J.E. Rix, S.J. Weigand, Structure-property model for polyethylene-derived carbon fiber, Carbon. 107 (2016) 525–535. https://doi.org/10.1016/j.carbon.2016.06.032.

[117] M.G. Northolt, L.H. Veldhuizen, H. Jansen, Tensile deformation of carbon fibers and the relationship with the modulus for shear between the basal planes, Carbon. 29 (1991) 1267–1279. https://doi.org/10.1016/0008-6223(91)90046-L.

[118] B.E. Barton, M.J. Behr, J.T. Patton, E.J. Hukkanen, B.G. Landes, W. Wang, N. Horstman, J.E. Rix, D. Keane, S. Weigand, M. Spalding, C. Derstine, High-modulus low-cost carbon fibers from polyethylene enabled by boron catalyzed graphitization, Small. 13 (2017) 1701926. https://doi.org/10.1002/smll.201701926.

[119] J.H. Eun, J.S. Lee, Study on polyethylene-based carbon fibers obtained by sulfonation under hydrostatic pressure, Sci. Rep. 11 (2021) 18028. https://doi.org/10.1038/s41598-021-97529-4.

[120] D. Choi, S.H. Yoo, S. Lee, Safer and more effective route for polyethylene-derived carbon fiber fabrication using electron beam irradiation, Carbon. 146 (2019) 9–16. https://doi.org/10.1016/j.carbon.2019.01.061.

[121] S.-H. Kang, K.-W. Kim, B.-J. Kim, Carbon fibers from high-density polyethylene using a hybrid cross-linking technique, Polymers (Basel). 13 (2021) 2157. https://doi.org/10.3390/polym13132157.

[122] E.J. Hukkanen, B.E. Barton, J.T. Patton, D.R. Schlader, Y. Zhang, X. Qiu, L. Brehm, B. Haskins, W. Wang, N. Horstman, M.A. Spalding, D.A. Hickman, C.W. Derstine, A novel continuous multiphase reactor for chemically processing polymer fibers, Ind. Eng. Chem. Res. 57 (2018) 6123–6130. https://doi.org/10.1021/ACS.IECR.8B00482.

[123] K.-W. Kim, H.-M. Lee, J.-H. An, B.-S. Kim, B.-G. Min, S.-J. Kang, K.-H. An, B.-J. Kim, A. Info, Effects of cross-linking methods for polyethylene-based carbon fibers: review, Carbon Lett. 16 (2015) 147–170. https://doi.org/10.5714/CL.2015.16.3.147.

[124] N. Saglio, P. Berticat, G. Vallet, Study of the pyrolysis of saturated chlorinated polyethylene fibers, J. Appl. Polym. Sci. 16 (1972) 2991–3002. https://doi.org/10.1002/app.1972.070161123.

[125] B. Laycock, X. Wang, R.F. Liu, P.K. Annamalai, J. Cork, C. Derstine, M. Mills, E.W. McFarland, Pyrolysis of brominated polyethylene as an alternative carbon fibre precursor, Polym. Degrad. Stab. 172 (2020) 109057. https://doi.org/10.1016/j.polymdegradstab.2019.109057.

[126] B.E. Barton, E.J. Hukkanen, G.F. Billovits, D. Schlader, M.J. Behr, D. Yancey, M. Rickard, X.H. Qiu, D.M. Mowery, L. Brehm, B. Haskins, W. Wang, M.S. Spalding, C. Derstine, Ammoxidation of polyethylene: A new route to carbon, Carbon. 130 (2018) 288–294. https://doi.org/10.1016/j.carbon.2018.01.031.

[127] E. Frank, E. Muks, A. Ota, T. Herrmann, M. Hunger, M.R. Buchmeiser, Structure evolution in polyethylene-derived carbon fiber using a combined electron beam-stabilization-sulphurization approach, Macromol. Mater. Eng. 306 (2021) 2100280. https://doi.org/10.1002/MAME.202100280.

[128] B.A. Trofimov, T.A. Skotheim, A.G. Mal'kina, L. V. Sokolyanskaya, G.F. Myachina, S.A. Korzhova, E.S. Stoyanov, I.P. Kovalev, Sulfurization of polymers, Russ. Chem. Bull. 2000 495. 49 (2000) 863–869. https://doi.org/10.1007/BF02494710.

[129] S.N. Tripathi, G.S.S.S. Rao, A.B. Mathur, R. Jasra, Polyolefin/graphene nanocomposites: A review, Royal Society of Chemistry, 2017. https://doi.org/10.1039/c6ra28392f.

[130] P. Govindaraj, A. Sokolova, N. Salim, S. Juodkazis, F.K. Fuss, B. Fox, N. Hameed, Distribution states of graphene in polymer nanocomposites: A review, Compos. Part B Eng. 226 (2021) 109353. https://doi.org/10.1016/j.compositesb.2021.109353.

[131] M.C. Sobieraj, C.M. Rimnac, Ultra high molecular weight polyethylene: Mechanics, morphology, and clinical behavior, J. Mech. Behav. Biomed. Mater. 2 (2009) 433–443. https://doi.org/10.1016/j.jmbbm.2008.12.006.

[132] K.R. Brown, C. Love-Baker, T.M. Harrell, X. Li, Effect of tension during sulfonation stabilization for UHMWPE-derived carbon fibers, J. Polym. Res. 30 (2023) 1–14. https://doi.org/10.1007/S10965-023-03829-W.

[133] K.R. Brown, C. Love-Baker, Z. Xue, X. Li, Ultra-high molecular weight polyethylene micro-ribbon fibers gel spun using orange terpenes, Polym. Eng. Sci. 64 (2024) 1743–1755. https://doi.org/10.1002/PEN.26656.

[134] J. -S Tsai, C. -H Lin, The effect of molecular weight on the cross section and properties of polyacrylonitrile precursor and resulting carbon fiber, J. Appl. Polym. Sci. 42 (1991) 3045–3050. https://doi.org/10.1002/APP.1991.070421124.

[135] DSM, Dyneema high-strength, high-modulus polyethylene fiber, (2008) 1–4. www.dyneema.com.

[136] J.W. Kim, J.S. Lee, Preparation of carbon fibers from linear low density polyethylene, Carbon. 94 (2015) 524–530. https://doi.org/10.1016/j.carbon.2015.06.074.

[137] B.M. Shay, Nonswelling texturing spin finish, US Patent 3704225, 1972.

[138] W. Postman, Spin finishes explained, Text. Res. J. 50 (1980) 444–453. https://doi.org/10.1177/004051758005000710.

[139] H.G. Ardiff, R. Klein, J.A. Young, T. Tam, UHMWPE fiber and method to produce, US Patent 9909240, 2018.

[140] J.-X. Li, Coupling agent effects on the interfacial adhesion in a sheath/core type bicomponent fiber, Ohio University, 1989.

[141] S. Holmes, P. Schwartz, Amination of ultra-high strength polyethylene using ammonia plasma, Compos. Sci. Technol. 38 (1990) 1–21. https://doi.org/10.1016/0266-3538(90)90068-G.

[142] T.M. Harrell, X. Li, Automated point tracking measurements using a smartphone to measure strain and displacement, in: Soc. Exp. Mech., Orlando, FL, USA, 2023.

[143] H.P. Klug, L.E. Alexander, Photographic Powder Techniques, in: X-Ray Diffr. Proced. Polycryst. Amorph. Mater., 2nd Editio, Wiley-Interscience, 1974: pp. 175–222.

[144] B.B. He, Data Treatment, in: Two-Dimensional X-Ray Diffr., John Wiley & Sons, Ltd, 2018: pp. 157–210. https://doi.org/10.1002/9781119356080.CH6.

[145] B.E. Warren, X-Ray diffraction in random layer lattices, Phys. Rev. 59 (1941) 693. https://doi.org/10.1103/PhysRev.59.693.

[146] H. Fujimoto, Theoretical X-ray scattering intensity of carbons with turbostratic stacking and AB stacking structures, Carbon. 41 (2003) 1585–1592. https://doi.org/10.1016/S0008-6223(03)00116-7.

[147] A. De Palmenaer, Ermittlung der prozessparameter zur kontinuierlichen herstellung von polyolefin-basierten carbonfasern, RWTH Aachen University, 2017.

[148] J. Mok, D. Choi, S.H. Bhang, Environmentally friendly route for fabricating conductive agent for lithium-ion batteries: Carbon nanoparticles derived from polyethylene, Catalysts. 11 (2021) 424. https://doi.org/10.3390/CATAL11040424/S1.

[149] D. Ramarajan, K. Tamilarasan, Ž. Milanović, D. Milenković, Z. Marković, S. Sudha, E. Kavitha, Vibrational spectroscopic studies (FTIR and FT-Raman) and molecular dynamics analysis of industry inspired 3-amino-4-hydroxybenzene sulfonic acid, J. Mol. Struct. 1205 (2020). https://doi.org/10.1016/j.molstruc.2019.127579.

[150] C. Li, H. Zhu, N. V. Salim, B.L. Fox, N. Hameed, Preparation of microporous carbon materials via in-depth sulfonation and stabilization of polyethylene, Polym. Degrad. Stab. 134 (2016) 272–283. https://doi.org/10.1016/j.polymdegradstab.2016.10.019.

[151] B. Xie, L. Hong, P. Chen, B. Zhu, Effect of sulfonation with concentrated sulfuric acid on the composition and carbonizability of LLDPE fibers, Polym. Bull. 73 (2016) 891–908. https://doi.org/10.1007/s00289-015-1525-y.

[152] F. Vautard, J. Dentzer, M. Nardin, J. Schultz, B. Defoort, Influence of surface defects on the tensile strength of carbon fibers, Appl. Surf. Sci. 322 (2014) 185–193. https://doi.org/10.1016/j.apsusc.2014.10.066.

[153] Z.E. Brubaker, J.J. Langford, R.J. Kapsimalis, J.L. Niedziela, Quantitative analysis of Raman spectral parameters for carbon fibers: practical considerations and connection to mechanical properties, J. Mater. Sci. 56 (2021) 15087–15121. https://doi.org/10.1007/S10853-021-06225-1.

[154] F. Tuinstra, J.L. Koenig, Raman spectrum of graphite, J. Chem. Phys. 53 (1970) 1126–1130. https://doi.org/10.1063/1.1674108.

[155] A.C. Ferrari, J. Robertson, Interpretation of Raman spectra of disordered and amorphous carbon, Phys. Rev. B. 61 (2000) 14095–14106. https://doi.org/10.1103/PhysRevB.61.14095.

[156] A. Sadezky, H. Muckenhuber, H. Grothe, R. Niessner, U. Pöschl, Raman microspectroscopy of soot and related carbonaceous materials: Spectral analysis and structural information, Carbon. 43 (2005) 1731–1742. https://doi.org/10.1016/J.CARBON.2005.02.018.

[157] M. Couzi, J.L. Bruneel, D. Talaga, L. Bokobza, A multi wavelength Raman scattering study of defective graphitic carbon materials: The first order Raman spectra revisited, Carbon. 107 (2016) 388–394. https://doi.org/10.1016/j.carbon.2016.06.017.

[158] M. Pawlyta, J.N. Rouzaud, S. Duber, Raman microspectroscopy characterization of carbon blacks: Spectral analysis and structural information, Carbon. 84 (2015) 479–490. https://doi.org/10.1016/j.carbon.2014.12.030.

[159] A. Cuesta, P. Dhamelincourt, J. Laureyns, A. Martínez-Alonso, J.M.D. Tascón, Raman microprobe studies on carbon materials, Carbon. 32 (1994) 1523–1532. https://doi.org/10.1016/0008-6223(94)90148-1.

[160] P. Puech, A. Dabrowska, N. Ratel-Ramond, G.L. Vignoles, M. Monthioux, New insight on carbonisation and graphitisation mechanisms as obtained from a bottom-up analytical approach of X-ray diffraction patterns, Carbon. 147 (2019) 602–611. https://doi.org/10.1016/j.carbon.2019.03.013.

[161] N. Iwashita, C.R. Park, H. Fujimoto, M. Shiraishi, M. Inagaki, Specification for a standard procedure of X-ray diffraction measurements on carbon materials, Carbon. 42 (2004) 701–714. https://doi.org/10.1016/j.carbon.2004.02.008.

[162] Z.W. Wilchinsky, Recent developments in the measurement of orientation in polymers by X-ray diffraction, Adv. X-Ray Anal. 6 (1962) 231–241. https://doi.org/10.1154/s037603080000210x.

[163] W.N. Reynolds, J.V. Sharp, Crystal shear limit to carbon fibre strength, Carbon. 12 (1974) 103–110. https://doi.org/10.1016/0008-6223(74)90018-9.

[164] W. Ruland, X-ray studies on preferred orientation in carbon fibers, J. Appl. Phys. 38 (1967) 3585–3589. https://doi.org/10.1063/1.1710176.

[165] J. Xu, C. Creighton, M. Johansen, F. Liu, S. Duan, D. Carlstedt, P. Mota-santiago, P. Lynch, L.E. Asp, Effect of tension during stabilization on carbon fiber multifunctionality for structural battery composites, Carbon. 209 (2023) 117982. https://doi.org/10.1016/j.carbon.2023.03.057.

[166] W. Whitney, R.M. Kimmel, Griffith equation and carbon fibre strength, Nat. Phys. Sci. 237 (1972) 93–94. https://doi.org/https://doi.org/10.1038/physci237093a0.

[167] D. Li, C. Lu, L. Wang, S. Du, Y. Yang, A reconsideration of the relationship between structural features and mechanical properties of carbon fibers, Mater. Sci. Eng. A. 685 (2017) 65–70. https://doi.org/10.1016/j.msea.2017.01.006.

[168] K. Honjo, Fracture toughness of PAN-based carbon fibers estimated from strength-mirror size relation, Carbon. 41 (2003) 979–984. https://doi.org/10.1016/S0008-6223(02)00444-X.

[169] J. Abrahamson, The surface energies of graphite, Carbon. 11 (1973) 337–362. https://doi.org/10.1016/0008-6223(73)90075-4.

[170] W.N. Reynolds, Physical Properties of Graphite, 1st ed., Elsevier Publishing Co. Ltd., Amsterdam, 1968.

[171] F. Tanaka, T. Okabe, H. Okuda, I.A. Kinloch, R.J. Young, Factors controlling the strength of carbon fibres in tension, Compos. Part A Appl. Sci. Manuf. 57 (2014) 88–94. https://doi.org/10.1016/j.compositesa.2013.11.007.

[172] Y. Li, M. Zhang, Mechanical properties of activated carbon fibers, in: J.Y. Chen (Ed.), Act. Carbon Fiber Text., Woodhead Publishing, 2017: pp. 167–180. https://doi.org/10.1016/B978-0-08-100660-3.00006-7.

[173] D. Veit, Fibers: History, Production, Properties, Market, 2023. https://doi.org/10.1007/978-3-031-15309-9.

[174] M.F. Hassan, M.A. Sabri, H. Fazal, A. Hafeez, N. Shezad, M. Hussain, Recent trends in activated carbon fibers production from various precursors and applications—A comparative review, J. Anal. Appl. Pyrolysis. 145 (2020) 104715. https://doi.org/10.1016/j.jaap.2019.104715.

[175] G.L.K. Hunter, W.B. Brogden, Terpenes and sesquiterpenes in cold-pressed orange oil, J. Food Sci. 30 (1965) 4. https://doi.org/10.1111/J.1365-2621.1965.TB00252.X.

[176] J.J. Senit, D. Velasco, A. Gomez Manrique, M. Sanchez-Barba, J.M. Toledo, V.E. Santos, F. Garcia-Ochoa, P. Yustos, M. Ladero, Orange peel waste upstream integrated processing to terpenes, phenolics, pectin and monosaccharides: Optimization approaches, Ind. Crops Prod. 134 (2019) 370–381. https://doi.org/10.1016/j.indcrop.2019.03.060.

[177] J.J. Hermans, P.H. Hermans, D. Vermaas, A. Weidinger, Quantitative evaluation of orientation in cellulose fibres from the X-ray fibre diagram, Recl. Des Trav. Chim. Des Pays-Bas. 65 (1946) 427–447. https://doi.org/10.1002/RECL.19460650605.

[178] A.L. Patterson, The scherrer formula for X-ray particle size determination, Phys. Rev. 56 (1939) 978–982. https://doi.org/10.1103/PhysRev.56.978.

[179] W.H. Bragg, W.L. Bragg, R.W. James, H. Lipson, The Crystalline State, 2nd ed., G. Bell, London, 1955.

[180] K.J. Putman, M.R. Rowles, N.A. Marks, C. De Tomas, J.W. Martin, I. Suarez-Martinez, Defining graphenic crystallites in disordered carbon: Moving beyond the platelet model, Carbon. 209 (2023). https://doi.org/10.1016/j.carbon.2023.03.040.

[181] K. Ramos, C.M. Fancher, J.L. Jones, LIPRAS: Line-Profile Analysis Software, (2017). https://github.com/SneakySnail/LIPRAS.

[182] K. Golovin, S.L. Phoenix, Effects of extreme transverse deformation on the strength of UHMWPE single filaments for ballistic applications, J. Mater. Sci. 51 (2016) 8075–8086. https://doi.org/10.1007/s10853-016-0077-3.

[183] X. Shi, Y. Bin, D. Hou, Y. Men, M. Matsuo, Gelation/crystallization mechanisms of UHMWPE solutions and structures of ultradrawn gel films, Polym. J. 46 (2014) 21–35. https://doi.org/10.1038/pj.2013.66.

[184] Y. Fukushima, H. Murase, Y. Ohta, Dyneema: Super fiber produced by the gel spinning of a flexible polymer, in: High-Performance Spec. Fibers, Springer Tokyo, 2016: pp. 109–132. https://doi.org/10.1007/978-4-431-55203-1.

[185] B. Wunderlich, Thermal analysis of polymeric materials, Springer Berlin Heidelberg, 2005. https://doi.org/10.1007/B137476/COVER.

[186] K.S. Simis, A. Bistolfi, A. Bellare, L.A. Pruitt, The combined effects of crosslinking and high crystallinity on the microstructural and mechanical properties of ultra high molecular weight polyethylene, Biomaterials. 27 (2006) 1688–1694. https://doi.org/10.1016/J.BIOMATERIALS.2005.09.033.

[187] Y.K. Kwon, A. Boller, M. Pyda, B. Wunderlich, Melting and heat capacity of gel-spun, ultra-high molar mass polyethylene fibers, Polymer (Guildf). 41 (2000) 6237–6249. https://doi.org/10.1016/S0032-3861(99)00839-3.

[188] A. Boller, B. Wunderlich, Multiple melting peak analysis with gel-spun ultra-high molar mass polyethylene, J. Therm. Anal. 49 (1997) 343–349. https://doi.org/10.1007/bf01987456.

[189] H. Xu, M. An, Y. Lv, L. Zhang, Z. Wang, Structural development of gel-spinning UHMWPE fibers through industrial hot-drawing process analyzed by small/wide-angle X-ray scattering, Polym. Bull. 74 (2017) 721–736. https://doi.org/10.1007/s00289-016-1742-z.

[190] C. Xiao, Y. Zhang, S. An, G. Jia, Investigation on the thermal behaviors and mechanical properties of ultrahigh molecular weight polyethylene (UHMW-PE) fibers, J. Appl. Polym. Sci. 59 (1996) 931–935. https://doi.org/10.1002/(SICI)1097-4628(19960207)59:6<931::AID-APP4>3.0.CO;2-Q.

[191] I. Karacan, Molecular structure and orientation of gel-spun polyethylene fibers, J. Appl. Polym. Sci. 101 (2006) 1317–1333. https://doi.org/10.1002/APP.22952.

[192] L. Berger, H.H. Kausch, C.J.G. Plummer, Structure and deformation mechanisms in UHMWPE-fibres, Polymer (Guildf). 44 (2003) 5877–5884. https://doi.org/10.1016/S0032-3861(03)00536-6.

[193] E. Tarani, I. Arvanitidis, D. Christofilos, D.N. Bikiaris, K. Chrissafis, G. Vourlias, Calculation of the degree of crystallinity of HDPE/GNPs nanocomposites by using various experimental techniques: a comparative study, J. Mater. Sci. 58 (2023) 1621–1639. https://doi.org/10.1007/s10853-022-08125-4.

[194] Y. Fu, W. Chen, M. Pyda, D. Londono, B. Annis, A. Böller, A. Habenschuss, J. Cheng, B. Wunderlich, Structure-property analysis for gel-spun, ultrahigh molecular mass polyethylene fibers, J. Macromol. Sci. - Phys. 35 (1996) 37–87. https://doi.org/10.1080/00222349608220375.

[195] S. Venkatram, J. McCollum, N. Stingelin, B. Brettmann, A close look at polymer degree of crystallinity versus polymer crystalline quality, Polym. Int. 72 (2023) 855–860. https://doi.org/10.1002/PI.6508.

[196] J.T. Yeh, S.S. Chang, Ultradrawing behavior of gel films of ultrahigh molecular weight polyethylene and low molecular weight polyethylene blends at varying drawing conditions, Polym. Eng. Sci. 42 (2002) 1558–1567. https://doi.org/10.1002/PEN.11051.

[197] M. Kakiage, D. Fukagawa, Preparation of ultrahigh-molecular-weight polyethylene fibers by combination of melt-spinning and melt-drawing, Mater. Today Commun. 23 (2020) 100864. https://doi.org/10.1016/J.MTCOMM.2019.100864.

[198] B. Zhu, J. Liu, T. Wang, M. Han, S. Valloppilly, S. Xu, X. Wang, Novel polyethylene fibers of very high thermal conductivity enabled by amorphous restructuring, ACS Omega. 2 (2017) 3931–3944. https://doi.org/10.1021/acsomega.7b00563.

[199] M. Nakae, H. Uehara, T. Kanamoto, A.E. Zachariades, R.S. Porter, Structure development upon melt drawing of ultrahigh molecular weight polyethylene: Effect of prior thermal history, Macromolecules. 33 (2000) 2632–2641. https://doi.org/10.1021/ma991330a.

[200] H. Uehara, M. Nakae, T. Kanamoto, A.E. Zachariades, R.S. Porter, Melt drawability of ultrahigh molecular weight polyethylene, Macromolecules. 32 (1999) 2761–2769. https://doi.org/10.1021/ma981491z.

[201] P. Smith, P.J. Lemstra, Ultra-high strength polyethylene filaments by solution spinning/drawing. 3. Influence of drawing temperature, Polymer (Guildf). 21 (1980) 1341–1343. https://doi.org/10.1016/0032-3861(80)90205-0.

[202] X.P. Hu, Y. Lo Hsieh, Crystallite sizes and lattice distortions of gel-spun ultra-high molecular weight polyethylene fibers, Polymer (Guildf). 30 (1998) 771–774. https://doi.org/10.1295/polymj.30.771.

[203] P.B. McDaniel, J.M. Deitzel, J.W. Gillespie, Structural hierarchy and surface morphology of highly drawn ultra high molecular weight polyethylene fibers studied by atomic force microscopy and wide angle X-ray diffraction, Polymer (Guildf). 69 (2015) 148–158. https://doi.org/10.1016/J.POLYMER.2015.05.010.

[204] V.M. Litvinov, J. Xu, C. Melian, D.E. Demco, M. Möller, J. Simmelink, Morphology, chain dynamics, and domain sizes in highly drawn gel-spun ultrahigh molecular weight polyethylene fibers at the final stages of drawing by SAXS, WAXS, and 1H Solid-State NMR, Macromolecules. 44 (2011) 9254–9266. https://doi.org/10.1021/ma201888f.

[205] C.J. Frye, I.M. Ward, M.G. Dobb, D.J. Johnson, Direct measurements of crystallite size distribution in ultra-high modulus polyethylene fibres, Polymer (Guildf). 20 (1979) 1310–1312. https://doi.org/10.1016/0032-3861(79)90265-9.

[206] L. Balzano, B. Coussens, T. Engels, F. Oosterlinck, M. Vlasblom, H. Van Der Werff, D. Lellinger, Multiscale structure and microscopic deformation mechanisms of gel-spun ultrahigh-molecular-weight polyethylene fibers, Macromolecules. 52 (2019) 5207–5216. https://doi.org/10.1021/acs.macromol.9b00247.

[207] J. Zhang, T. Lei, J.-T. Yeh, C. Jen-Taut Yeh, H. Collaborative, Multiple-stage drawn ultrahigh molecular weight polyethylene/activated carbon fibers prepared with the assistance of supercritical CO2, Polym. Compos. 41 (2020) 4994–5005. https://doi.org/10.1002/PC.25769.

[208] Y. Sun, Q. Wang, X. Li, X. Chen, Y. Ma, Q. Zhang, X. Jin, Y. Jiang, L. Sun, Q. Luo, Investigation on dry spinning process of ultrahigh molecular weight polyethylene/decalin solution, J. Appl. Polym. Sci. 98 (2005) 474–483. https://doi.org/10.1002/APP.22001.

[209] Y. Sun, Y. Duan, X. Chen, Q. Zhang, X. Jin, X. Li, M. Yan, L. Sun, Q. Wang, Research on the molecular entanglement and disentanglement in the dry spinning process of UHMWPE/decalin solution, J. Appl. Polym. Sci. 102 (2006) 864–875. https://doi.org/10.1002/APP.23672.

[210] C.K. Henry, G.R. Palmese, N.J. Alvarez, The evolution of crystalline structures during gel spinning of ultra-high molecular weight polyethylene fibers, Soft Matter. 14 (2018) 8974. https://doi.org/10.1039/c8sm01597j.

[211] Y. Tian, C. Zhu, J. Gong, J. Ma, J. Xu, Transition from shish-kebab to fibrillar crystals during ultra-high hot stretching of ultra-high molecular weight polyethylene fibers: In situ small and wide angle X-ray scattering studies, Eur. Polym. J. 73 (2015) 127–136. https://doi.org/10.1016/j.eurpolymj.2015.10.006.

[212] C.M. Hansen, The Three Dimensional Solubility Parameter and Solvent Diffusion Coefficient., Technical University of Denmark, 1967.

[213] Y. Kusano, S. Teodoru, C.M. Hansen, The physical and chemical properties of plasma treated ultra-high-molecular-weight polyethylene fibers, Surf. Coatings Technol. 205 (2011) 2793–2798. https://doi.org/10.1016/J.SURFCOAT.2010.10.041.

[214] S. Abbott, HSP Basics, Pract. Solubility. (n.d.). https://www.stevenabbott.co.uk/practical-solubility/hsp-basics.php.

[215] R. Gallu, F. Méchin, F. Dalmas, J.F. Gérard, R. Perrin, F. Loup, Investigating compatibility between TPU and bitumen SARA fractions by means of Hansen solubility parameters and interfacial tension measurements, Constr. Build. Mater. 289 (2021). https://doi.org/10.1016/j.conbuildmat.2021.123151.

[216] H. Yamamoto, HSP Application Note #14: How to look at flavor with Hansen Solubility Parameters (HSP), Pirika. (2019). pirika.com/NewHP/PirikaE/Flavor.html.

[217] H. Yamamoto, HSP Application Note #34: Hansen Solubility Parameter (HSP) and Gall STone, Pirika. (2010). pirika.com/NewHP/PirikaE2/Gallstone.html.

[218] E.J. Leão Lana, K.A. da Silva Rocha, I. V. Kozhevnikov, E. V. Gusevskaya, Synthesis of 1,8-cineole and 1,4-cineole by isomerization of α-terpineol catalyzed by heteropoly acid, J. Mol. Catal. A Chem. 259 (2006) 99–102. https://doi.org/10.1016/j.molcata.2006.05.064.

[219] G. Dougnon, M. Ito, Inhalation administration of the bicyclic ethers 1,8- and 1,4-cineole prevent anxiety and depressive-like behaviours in mice, Molecules. 25 (2020) 13. https://doi.org/10.3390/molecules25081884.

[220] M. Soh, G.W. Stachowiak, The application of cineole as a grease solvent, Flavour Fragr. J. 17 (2002) 278–286. https://doi.org/10.1002/FFJ.1103.

[221] G. Antalick, S. Tempère, K. Šuklje, J.W. Blackman, A. Deloire, G. De Revel, L.M. Schmidtke, Investigation and sensory characterization of 1,4-cineole: A potential aromatic marker of Australian Cabernet Sauvignon wine, J. Agric. Food Chem. 63 (2015) 9103–9111. https://doi.org/10.1021/acs.jafc.5b03847.

[222] U.S. Coast Guard Department of Transportation, CHRIS - Hazardous Chemical Data Volume II, U.S. Government Printing Office, Washington, DC, 1984.

[223] M. Yi, Z. Shen, A review on mechanical exfoliation for the scalable production of graphene, J. Mater. Chem. A. 3 (2015) 11700. https://doi.org/10.1039/c5ta00252d.

[224] G. Faour, M. Grimaldi, J. Richou, A. Bois, Real-time pendant drop tensiometer using image processing with interfacial area and interfacial tension control capabilities, J. Colloid Interface Sci. 181 (1996) 385–392. https://doi.org/10.1006/jcis.1996.0395.

[225] M. Cayambe, C. Zambrano, T. Tene, M. Guevara, G. Tubon Usca, H. Brito, R. Molina, D. Coello-Fiallos, L.S. Caputi, C. Vacacela Gomez, Dispersion of graphene in ethanol by sonication, Mater. Today Proc. 37 (2021) 4027–4030. https://doi.org/10.1016/j.matpr.2020.06.441.

[226] X. Zhang, A.C. Coleman, N. Katsonis, W.R. Browne, B.J. Van Wees, B.L. Feringa, Dispersion of graphene in ethanol using a simple solvent exchange method, Chem. Commun. 46 (2010) 7539–7541. https://doi.org/10.1039/C0CC02688C.

[227] S.J. Goldie, M.T. Degiacomi, S. Jiang, S.J. Clark, V. Erastova, K.S. Coleman, Identification of graphene dispersion agents through molecular fingerprints, ACS Nano. 16 (2022) 16109–16117. https://doi.org/10.1021/acsnano.2c04406.

[228] U. Patil, N.M. Caffrey, The role of solvent interfacial structural ordering in maintaining stable graphene dispersions, 2D Mater. 11 (2023) 015017. https://doi.org/10.1088/2053-1583/AD10BA.

[229] A.C. Ferrari, D.M. Basko, Raman spectroscopy as a versatile tool for studying the properties of graphene, Nature Nanotech. 8 (2013) 235–246. https://doi.org/10.1038/nnano.2013.46.

[230] A.C. Ferrari, J. Robertson, Interpretation of Raman spectra of disordered and amorphous carbon, Phys. Rev. B. 60 (2000) 14095. https://doi.org/10.1103/PhysRevB.61.14095.

[231] A. Eckmann, A. Felten, A. Mishchenko, L. Britnell, R. Krupke, K.S. Novoselov, C. Casiraghi, Probing the nature of defects in graphene by Raman spectroscopy, Nano Lett. 12 (2012) 3925–3930. https://doi.org/10.1021/nl300901a.

[232] E. Ceretti, P.S. Ginestra, M. Ghazinejad, A. Fiorentino, M. Madou, Electrospinning and characterization of polymer–graphene powder scaffolds, CIRP Ann. 66 (2017) 233–236. https://doi.org/10.1016/J.CIRP.2017.04.122.

[233] T. Dayyoub, A. V. Maksimkin, S. Kaloshkin, E. Kolesnikov, D. Chukov, T.P. Dyachkova, I. Gutnik, The structure and mechanical properties of the UHMWPE films modified by the mixture of graphene nanoplates with polyaniline, Polymers (Basel). 11 (2019). https://doi.org/10.3390/polym11010023.

[234] E. Tarani, D.G. Papageorgiou, C. Valles, A. Wurm, Z. Terzopoulou, D.N. Bikiaris, C. Schick, K. Chrissafis, G. Vourlias, Insights into crystallization and melting of high density polyethylene/graphene nanocomposites studied by fast scanning calorimetry, Polym. Test. 67 (2018) 349–358. https://doi.org/10.1016/j.polymertesting.2018.03.029.

[235] J.W. Jiang, J. Zhao, K. Zhou, T. Rabczuk, Superior thermal conductivity and extremely high mechanical strength in polyethylene chains from ab initio calculation, J. Appl. Phys. 111 (2012) 124304. https://doi.org/10.1063/1.4729489/147017.

[236] B. Crist, The ultimate strength and stiffness of polymers, Annu. Rev. Mater. Sci. 25 (1995) 295–323. https://doi.org/10.1146/annurev.ms.25.080195.001455.

[237] P. Li, L. Hu, A.J.H. McGaughey, S. Shen, Crystalline polyethylene nanofibers with the theoretical limit of Young's modulus, Adv. Mater. 26 (2014) 1065–1070. https://doi.org/10.1002/ADMA.201304116.

[238] I.M. Ward, P.J. Lemstra, Production and properties of high-modulus and high-strength polyethylene fibres, Handb. Text. Fibre Struct. 1 (2009) 352–393. https://doi.org/10.1533/9781845696504.2.352.

[239] N.Z. Wang, M.Z. Shi, C. Shang, F.B. Meng, L.K. Ma, X.G. Luo, X.H. Chen, Tunable superconductivity by electrochemical intercalation in TaS2, New J. Phys. 20 (2018) 023014. https://doi.org/10.1088/1367-2630/AAA8A7.

[240] M. An, H. Xu, Y. Lv, Q. Gu, F. Tian, Z. Wang, An in situ small-angle X-ray scattering study of the structural effects of temperature and draw ratio of the hot-drawing process on ultra-high molecular weight polyethylene fibers, RSC Adv. 6 (2016) 51125–51134. https://doi.org/10.1039/C6RA09965C.

[241] C.G. Vonk, G. Kortleve, X-ray small-angle scattering of bulk polyethylene, Kolloid-Zeitschrift Zeitschrift Für Polym. 220 (1967) 19–24. https://doi.org/10.1007/BF02086052.

[242] G.R. Liu, A step-by-step method of rule-of-mixture of fiber- and particle-reinforced composite materials, Compos. Struct. 40 (1997) 313–322. https://doi.org/10.1016/S0263-8223(98)00033-6.

[243] M.A. Rafiee, J. Rafiee, Z. Wang, H. Song, Z.Z. Yu, N. Koratkar, Enhanced mechanical properties of nanocomposites at low graphene content, ACS Nano. 3 (2009) 3884–3890. https://doi.org/10.1021/NN9010472/SUPPL_FILE/NN9010472_SI_001.PDF.

[244] M.M. Shokrieh, H. Moshrefzadeh-Sani, On the constant parameters of Halpin-Tsai equation, Polymer (Guildf). 106 (2016) 14–20. https://doi.org/10.1016/J.POLYMER.2016.10.049.

[245] R. Arasteh, M. Omidi, A.H.A. Rousta, H. Kazerooni, A Study on Effect of Waviness on Mechanical Properties of Multi-Walled Carbon Nanotube/Epoxy Composites Using Modified Halpin–Tsai Theory, J. Macromol. Sci. Part B. 50 (2011) 2464–2480. https://doi.org/10.1080/00222348.2011.579868.

[246] M.U. Azam, A. Schiffer, S. Kumar, Mechanical and piezoresistive properties of GNP/UHMWPE composites and their cellular structures manufactured via selective laser sintering, J. Mater. Res. Technol. 28 (2024) 1359–1369. https://doi.org/10.1016/J.JMRT.2023.12.089.

[247] M.J. Martínez-Morlanes, F.J. Pascual, G. Guerin, J.A. Puértolas, Influence of processing conditions on microstructural, mechanical and tribological properties of graphene nanoplatelet reinforced UHMWPE, J. Mech. Behav. Biomed. Mater. 115 (2021) 104248. https://doi.org/10.1016/J.JMBBM.2020.104248.

[248] S. Tsuzuki, A. Fujii, J. í poner, K.E. Riley, P. Hobza, I. Soteras, M. Orozco, F. Javier Luque, Nature and physical origin of CH/π interaction: significant difference from conventional hydrogen bonds, Phys. Chem. Chem. Phys. 10 (2008) 2584–2594. https://doi.org/10.1039/B718656H.

[249] X. Han, T. Chen, Y. Zhao, J. Gao, Y. Sang, H. Xiong, Z. Chen, Relationship between the microstructure and performance of graphene/polyethylene composites investigated by positron annihilation lifetime spectroscopy, Nanomaterials. 11 (2021) 2990. https://doi.org/10.3390/nano11112990.

[250] A.N. Rissanou, A.J. Power, V. Harmandaris, Structural and dynamical properties of polyethylene/gGraphene nanocomposites through molecular dynamics simulations, Polymers (Basel). 7 (2015) 390–417. https://doi.org/10.3390/polym7030390.

[251] P.J. Barham, Strong polymer fibres, Phys. Technol. 17 (1986) 167. https://doi.org/10.1088/0305-4624/17/4/303.

[252] H. Dong, Z. Wang, T.C. O'Connor, A. Azoug, M.O. Robbins, T.D. Nguyen, Micromechanical models for the stiffness and strength of UHMWPE macrofibrils, J. Mech. Phys. Solids. 116 (2018) 70–98. https://doi.org/10.1016/J.JMPS.2018.03.015.

[253] C. Fu, R. Zhang, J. Tian, Q. Yang, P. Xue, X. Chen, Polymer chain conformations in hybrid composites of UHMWPE incorporated by GNP/MWCNT, J. Polym. Res. 30 (2023) 245. https://doi.org/10.1007/s10965-023-03629-2.

[254] C.L. Keller, K.R. Doppalapudi, J.D. Woodroffe, B.G. Harvey, Solvent-free dehydration, cyclization, and hydrogenation of linalool with a dual heterogeneous catalyst system to generate a high-performance sustainable aviation fuel, Commun. Chem. 2022 51. 5 (2022) 1–8. https://doi.org/10.1038/s42004-022-00725-0.

[255] A. Sushchenko, A. Scherschel, C. Love-Baker, R. Cordier, T.M. Harrell, K.R. Brown, X. Li, Evaluating consumer 3D printing nozzles as a low cost alternative for mesophase pitch-derived carbon fiber production, Carbon. 225 (2024) 119088. https://doi.org/10.1016/J.CARBON.2024.119088.

[256] B. Rahman, Flow Modeling of Synthetic Pitch Extrusion through Spinnerets for Continuous Fibers, Clemson University, 2018.

[257] Z. Wang, L. Sangroniz, J. Xu, C. Zhu, A. Müller, Polymer physics behind the gel-spinning of UHMWPE fibers, Macromol. Rapid Commun. (2024) 2400124. https://doi.org/10.1002/MARC.202400124.

[258] S.C. Chowdhury, S. Sockalingam, J.W. Gillespie, Inter-molecular interactions in ultrahigh molecular weight polyethylene single crystals, Comput. Mater. Sci. 172 (2020). https://doi.org/10.1016/j.commatsci.2019.109360.

[259] V. Jiménez, P. Sánchez, A. Romero, Fundamentals of Carbonized and Activated Carbon, in: J.Y. Chen (Ed.), Act. Carbon Fiber Text., Woodhead Publishing, 2017: pp. 1–19.

[260] N.M. Osmond, Activated carbon fibre adsorbent materials, Adsorpt. Sci. Technol. 18 (2000) 529–539. https://doi.org/10.1260/0263617001493594.